Dynamic nonlinear light control and metrology with resonant metasurfaces

Falco Bijloo

Dynamic nonlinear light control and metrology with resonant metasurfaces

Ph.D. Thesis, University of Amsterdam, 17 December 2025
Dynamic nonlinear light control and metrology with resonant metasurfaces
Falco Bijloo

The work described in this thesis was performed at
AMOLF, Science Park 104 & ARCNL, Science Park 106
1098 XG Amsterdam, The Netherlands, Both are institutes of the Foundation
for Dutch Scientific Research Institutes (NWO-I)

Dynamic nonlinear light control and metrology with resonant metasurfaces

ACADEMISCH PROEFSCHRIFT

ter verkrijging van de graad van doctor
aan de Universiteit van Amsterdam
op gezag van de Rector Magnificus
prof. dr. ir. P.P.C.C. Verbeek
ten overstaan van een door het College voor Promoties ingestelde commissie,
in het openbaar te verdedigen in de Agnietenkapel
op woensdag 17 december 2025, te 13.00 uur

door

Falco Bijloo

geboren te Delft

Promotiecommissie

Promotores:	prof. dr. A. F. Koenderink	Universiteit van Amsterdam
	dr. P. M. Kraus	Vrije Universiteit Amsterdam
Overige leden:	prof. dr. R. Grange	ETH Zürich
	prof. dr. S. M. Witte	TU Delft
	dr. J. van de Groep	Universiteit van Amsterdam
	dr. C. J. M. Coulais	Universiteit van Amsterdam
	prof. dr. H. J. Bakker	Universiteit van Amsterdam

Faculteit der Natuurwetenschappen, Wiskunde en Informatica

Contents

Chapter 1

Introduction

The mass production of nanoelectronic devices has entered a new era, enabled by extreme ultraviolet (EUV) lithography. Modern nanolithography technique uses monochromatic 13.5 nm light to print structures with sub-10 nm feature sizes. This technology rests on immense scientific and engineering efforts, for instance in developing the ultra-bright EUV source, the technology to image with EUV light, and the mechatronics required to rapidly and reproducibly expose wafers on industrial scales. These advances are not just scientific milestones, they form the technological foundation of smartphones, autonomous systems, data centers and storage, artificial intelligence hardware, and virtually all modern digital infrastructure. An essential step in manufacturing such intricate nanostructures, is the precise inspection of the tiniest of details, a process known as *metrology*. During lithographic processes, the dimensions of each patterned layer are accurately monitored, as well as the relative alignment and positioning of successive layers and the material properties. Without this tight control, the functionality of the final device cannot be guaranteed, and the production yield would plummet.

At the **Advanced Research Center for Nanolithography (ARCNL)** institute in Amsterdam, metrology concepts for future generation EUV lithography are part of the central research directions. Here, researchers explore and develop advanced methods to probe and monitor nanoscale patterns, sub-nm geometrical variations, material characteristics and more, to constantly push the limits of resolution and throughput of semiconductor metrology. Meanwhile, next door at the research institute **AMOLF**, many research groups focus on *nanophotonics*: the study of how light interacts with matter at the nanoscale. This field explores fundamental principles and applied techniques of light manipulation using nanostructures, to enable tailored structured beam shaping, extreme light confinement, sensitive optical sensing and ultra-fast nonlinear phenomena, among others.

The work presented in this Thesis is inspired by the desire to bridge these two worlds. By applying fundamental nanophotonic insights into how light behaves at extremely small scales, it addresses advanced metrology challenges that require resolution at ever-finer detail. Especially nonlinear phenomena show great promise, due to the benefits of short wavelengths and power-dependent outputs. As such, this Thesis is situated at the interface of two research fields, namely **semiconductor metrology** and **nonlinear optical control in nanophotonic structures**.

1.1 Metrology in the semiconductor industry

The production of microelectronic devices is advancing at an extraordinary pace [1]. The continuous drive for smaller, faster and more efficient electronic devices has led to remarkable progress in semiconductor manufacturing, with feature sizes now routinely reaching well below 10 nanometers [2–4]. This miniaturization drives the current performance of modern technologies, including mobile devices, high-performance computing, data infrastruc-

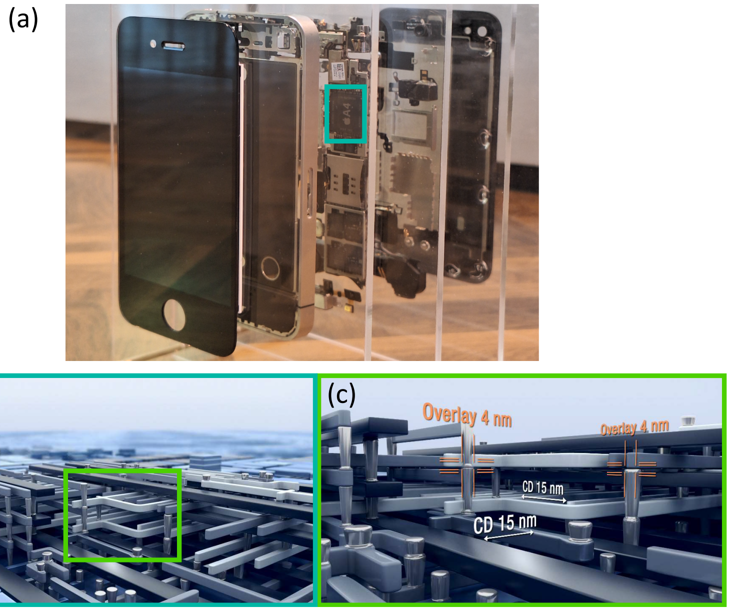

Figure 1.1: Illustration of a semiconductor stack network, commonly found in modern smartphones. a) The inner device of a modern smartphone presents an intricate and complicated world of networks and circuit boards. The chip is located at the blue rectangle. b) Artist's impression of the smallest device features inside a semiconductor integrated circuit. c) Layer-to-layer alignment and correct feature sizes at the tiniest scale are essential to device functionality. *Images (b) and (c) provided by, and property of, ASML.*

ture, and autonomous systems [5–7]. For example, these rapid developments are clearly visible in mobile communication. Just four decades ago, portable phones often weighed around 1 kg, costing thousands of dollars and were limited to basic voice calls. In contrast, current smartphones are compact and lightweight, accessible at a fraction of the cost, and are equipped with functions that far exceed their predecessors. Even the simplest budget phone has multi-core processors running at 1-2 GHz, with gigabytes of random access memory (RAM). In comparison, the Apollo Guidance Computer, on board of the Apollo spacecraft which flew missions to the moon in the time period from 1961 to 1972, operated at 2 MHz and had 3.75 KB of RAM [8]. Until the turn of the millennium, the clock-rate of computing devices steadily accelerated, eventually reaching a few GHz. Since then, further performance improvements have come almost solely from the continued miniaturization of microelectronic systems. This relentless down-scaling of microelectronics is the main reason why even a low-end smartphone today can perform millions of times more operations per second than the Apollo Guidance Computer.

Hand in hand with shrinking dimensions of the microelectronic devices is the emergence of new challenges. Chief among those challenges is the difficulty of accurately visualizing and verifying nanoscale features during nanolithographic fabrication processes [4, 9]. Figure 1.1 illustrates the inner work of semiconductor chips, similar to those used in modern smartphone technology. As device functionality is determined by nanoscale accuracy of geometric features and layer-to-layer alignment, precise inspection and control are essential to ensure product yield and manufacturing efficiency. This precise inspection is what the semiconductor industry refers to as **metrology**.

1.1.1 Fundamentals of modern semiconductor metrology

In our everyday experience, we often understand things by looking at them. We observe the world to make sense of it. As such, perhaps the most intuitive approach to quality control is to perform imaging, creating a spatial representation of the properties (geometry, shape, material distribution) of an object using light, electrons, or a sharp mechanical scanning probe. The goal of imaging is often to obtain the most faithful representation while making a minimal set of prior assumptions on the properties of the object at hand. However, in semiconductor metrology, direct visualization is not always necessary. The goal is not to render the full microelectronic architecture of a chip, but rather to extract very precisely the value of a select set of critical parameters, while making maximum use of prior knowledge of the approximate geometry of the architecture in hand. These parameters present quantities that, though few in number, are rich in meaning for device performance. The semiconductor manufacturer relies on metrology parameters to assess whether an integrated circuit system will operate correctly and reliably [1, 9].

Key metrology parameters [4, 10–14] include the edge placement error

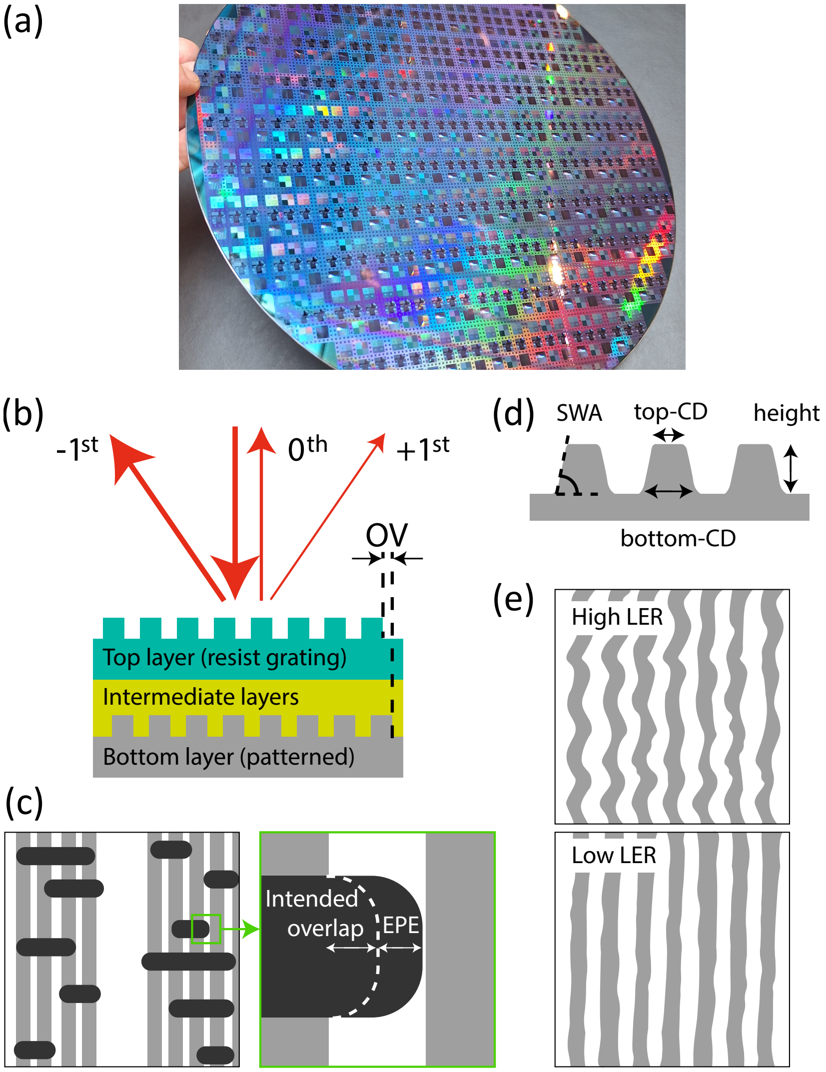

Figure 1.2: Schematics of key metrology parameters. a) Picture of 300 mm silicon wafer, fully patterned with integrated circuits. b) Diffraction-based overlay measures the relative overlay of two layers by comparing diffracted light intensities. c) Edge placement errors measures the displacement of edges of features from their intended target position. d) A cross-cut provides information about CD (and top- and bottom-CD), sidewall angle, and height. e) A top view of printed lines enables the measurement of the variation of the line edges from their average center position, allowing extraction of the line edge roughness.

(EPE), which measures the displacement of the edge of a feature from its intended target position; the overlay error (OV), describing the (mis)alignment between successive lithographic layers; and the critical dimension (CD), referring to the minimum feature size (or gap) in a specific layer and material. Advanced metrology also differentiates between top- and bottom-CD, indicating that the upper and lower parts of structures may exhibit different lateral widths. Additional parameters of interest are the sidewall angle (SWA), which describes the angle between the side of the fabricated structure and the surface of the wafer substrate; the film thickness or structure height; surface and line-edge roughness (LER), which quantifies the variation of a line's edge from its ideal smooth shape; and the material properties, such as chemical composition or crystal orientation and structure. The most important metrology parameters are summarized in Fig. 1.2.

Improvements in optical lithography have played an essential role in the continuous down-scaling of semiconductor device features. Currently, EUV-lithography machines use light with just 13.5 nm wavelength for exposure, while the numerical aperture (NA) of the imaging optics has increased to 0.55 [15]. Together with smart illumination algorithms, and tailored photochemistry via resists, this has resulted in the extreme small nodes of 3-5 nm that are already making their way out of industrial EUV machines on the most high-end chips [15, 16]. The accuracy in the small printed features is extremely important. A tiny mismatch in OV or CD can result in faulty devices, wasting valuable resources and energy. For critical layers, the maximum allowed OV error variation across a 300 mm wafer is commonly, relatively easily, maintained below 4-5 nm, with current OV errors in high-end manufacturing on the order of 1-2 nm [17], with a precision in OV metrology of 0.1-0.2 nm [16]. In addition to low OV errors, the industry requires a CD uniformity to remain below 10% of the smallest CD across the entire wafer [9, 18]. Achieving these tolerances requires not only advanced manufacturing techniques, but also metrology sensors for quality control that operate with sub-nm precision [19].

Three primary techniques are used to perform this high-precision metrology [1, 9]. The first is scanning electron microscopy (SEM), which relies on direct visualization of features through electron scattering. This technique is often applied to random places on the integrated circuit itself to inspect almost all metrology parameters, but most importantly and routinely used for CD and EPE. Second, optical scatterometry uses the scattered light from cleverly designed metrology targets that are placed spatially separated from the functional integrated circuits, to measure spectra and angular distribution [9, 20, 21]. The scattered light is often compared to library-based models, to analyze and determine many intricate parameters such as OV and CD. An established industrial application of optical scatterometry is ASML's YieldStar metrology system [22]. In this technique, visible light and essentially a high-NA microscope objective are used for illumination and collection. However, instead of analyzing (diffraction-limited) real-space images, analysis is based on pupil plane data, equivalently termed Fourier-space images, or diffraction patterns. The third technique involves atomic force microscopy (AFM), in which a tiny sharp tip mechanically scans the surface to extract topographical information. AFM is most commonly used to determine surface roughness and could also be used for OV and EPE, but more in research and development (R&D) and validational settings. The industry also makes a distinction between metrology focused on information in the wafer plane (e.g., lateral alignment of layers, and the linewidth of features as measured in a plane parallel to the wafer) and cross-sectional information. For instance in the context of SEM one differentiates Critical Dimension SEM (CD-SEM) and Cross-Sectional SEM (X-SEM) [14], where the latter is an invasive (or rather, destructive) technique in which samples are physically cleaved along a feature of interest to expose a cross-section. This cross-section allows to study the complete profile of an etched line such as height, edge rounding, top- and bottom CD and SWA. Another technique that is routinely used in calibration and R& D settings is transmission electron microscopy (TEM). Although TEM offers the highest resolution of any technique, it is not used in production lines due to its very low throughput of (sub-)single wafers per hour.

1.1.2 Current limitations and constraints

All metrology techniques are subject to stringent sets of requirements to handle the big challenge of robust sub-nm measurement precision at high productivity ($>$ 200 wafers per hour). The inspection tools need to deliver high throughput (*i.e.* be fast), make accurate and precise measurements and estimations, and if tell-tale scattering targets in between devices are used, these must take up little wafer surface area. Furthermore, while inspection during R&D

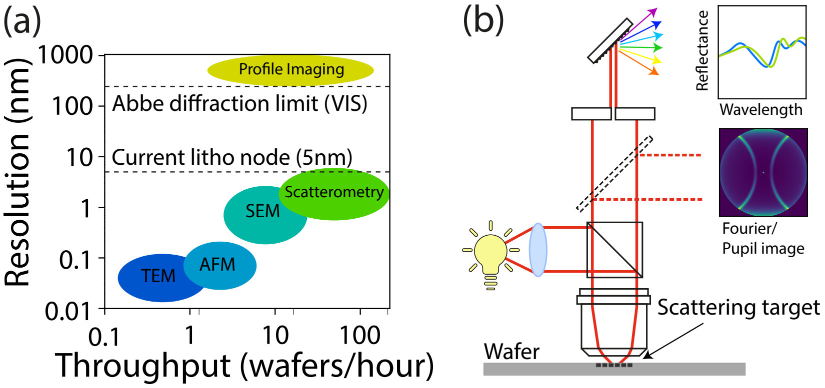

Figure 1.3: a) Resolution and throughput comparison of different metrology techniques [4]. b) Optical scatterometry microscope setup to measure both reflected spectrum and angle dependent scattering in Fourier space. *Figure adapted from Setija and Koenderink.*

or process development and calibration can be destructive, in-line production monitoring tools are required to be non-invasive.

Each technique excels in a certain requirement, while being limited in the other. The main trade-off is throughput versus resolution. The resolution-throughput performance of the most common techniques is summarized in Fig. 1.3a) [4]. Techniques relying on SEM, to determine CD for example, offer extremely high resolution and accuracy [23, 24]. Sub-nm CD variations are easily detectable and the accuracy in determining LER and SWA is unmatched. However, as SEM relies on point-by-point scanning of a focused electron beam, the technique allows only a modest throughput of a few to tens of wafers per hour [1]. In contrast, optical scatterometry techniques (setup sketched in Fig. 1.3b) enable full-wafer scanning, resulting in significantly higher throughputs, which often exceeds more than 125 wafers per hour [1]. However, the high speed comes at the cost of a large struggle to reach nanometer or sub-nanometer resolutions, as optical techniques are inherently limited by the large (typically 0.5 to 1.5 μm) wavelength.

At this point we must remark that the scientific and industrial use of the term *resolution* is quite different. In the scientific context of optical imaging the 'Abbe diffraction limit' is a central tenet for the resolution of an optical instrument, describing the minimum separation required between two objects so that they can be separately observed. It is well-known from the field of super-resolution microscopy that with prior knowledge, optical measurements can pinpoint spatial information more precisely than the Abbe limit [25]. For instance, with the prior knowledge that an object is a single point in a homogeneous environment, localization techniques like photo-activated localization microscopy (PALM) [26] and stochastic optical reconstruction microscopy (STORM) [27] can pinpoint the location of single molecules with nanometer accuracy. Similarly, metrology is not primarily concerned with general-purpose imaging, but with the extraction of dimensional parameters while making maximum use of prior information. Within that context, the relevant terminology for measurement performance are *sensitivity*, *accuracy* and *precision*. Sensitivity refers to the smallest change in a physical quantity (for example displacement, temperature or refractive index) an optical system can detect. Accuracy is defined as the closeness of a measurement to the true value (relating to the lack of systematic error), whereas precision describes the degree of consistency among repeated measurements (relating to spread in measurements). Resolution is closely related to sensitivity, but differs in that it describes a system's ability to distinguish between two closely spaced objects, features, or values. In essence, it reflects how finely the system can separate detail, whether spatial, temporal, spectral, or angular. We adopt the terminology commonly used in industry literature, which applies the term *resolution* rather liberally, and use it in a broader, more flexible sense. This means that we use resolution to refer to the smallest detectable physical feature, *or* difference, a system can reliably resolve.

In the case of determining OV-errors, resolutions are required of a single digit nanometer, which is at the limit of the capabilities of modern diffraction based OV (DBO) techniques [28] and displacement metrology [29]. DBO is a technique that requires patterning identical diffraction gratings across subsequent layers (potentially including intermediate layers) and relies on interference effects that induce intensity differences between opposite diffracted orders due to nonzero OV [9] (Fig. 1.2b). At future smaller nodes, visible-light DBO is not sufficient to keep up with the smallest resolutions. Furthermore, most current optical metrology targets require large surface areas. They are essentially optical diffraction gratings of pitch commensurate with the wavelength, and to obtain a diffraction pattern one must illuminate at least a few grating lines. Finally, the measured optical contrast upon an OV or CD *difference* is intrinsically very low. While this is counteracted by having exhaustive optical models and extensively validated benchmarking libraries, this low scatterometry contrast is a fundamental limit for both precision and accuracy of the measurement.

The semiconductor industry is worth hundreds of billions of dollars, creating strong incentives to improve manufacturing efficiency. Lithographic yield, and thereby resource utilization, crucially depends on the ability to perform metrology with 1) high throughput, 2) high resolution, and 3) at a reduced footprint. In essence, improving accuracy and resolution decreases the number of faulty devices, while allowing even smaller device features, and throughput increases the number of chips inspected per time. A reduced footprint increases the valuable wafer real estate that is allowed to print chips. The economic impact of improved yield through faster and more accurate metrology is immense: with a global annual revenue of \$600 billion in lithography, even a 1% improvement in yield translates to a value of \$6 billion in added value [30]. At ASML, the global leader in nanolithography machines, inspection and metrology tools represent furthermore a significant fraction of the revenue of chip-making equipment systems [31]. Clearly, there is a very large motivation to search for techniques that operate at the high throughput of optical scatterometry with larger contrast, while allowing resolutions below a single nanometer, with large accuracy and reduced footprint.

1.2 Resonant metasurfaces

This Thesis is positioned on the interface of two fields, namely, optical scatterometry-based metrology and the rich world of nonlinear optical control in nanophotonics. At the heart of this union lies one of the most powerful platforms in modern nanophotonics: **resonant metasurfaces**. In the past two decades, metasurfaces have formed into a core paradigm for controlling, manipulating, and studying light [32–35]. These metasurfaces are carefully engineered surfaces that are composed of arrays of subwavelength

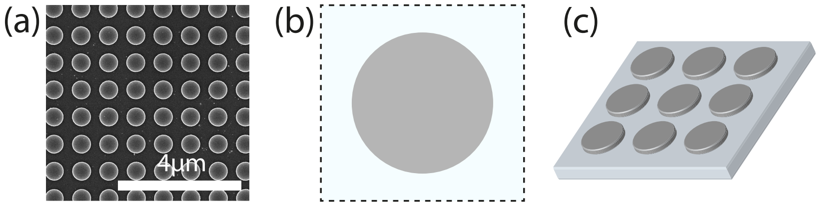

Figure 1.4: Resonant all-dielectric metasurfaces a) SEM image of a silicon nanodisk on a quartz substrate offers a relative simple platform to study spectrally separate Mie resonances. b) Schematic of a single unit-cell/meta-atom of a disk metasurface. c) Schematic of 3x3 meta-atoms disk metasurface.

nanostructures (often referred to as meta-atoms or unit-cells), placed in generally aperiodic arrangements, designed to manipulate light with a degree of control not achievable with conventional optics. As such, metasurfaces are a very rich generalization of the classical diffraction grating. Figure 1.4a) shows an example SEM image of a 2D grid of silicon disks on a quartz substrate, Fig. 1.4b) visualizes a schematic of the individual meta-atom and Fig. 1.4c) shows a schematic of 3x3 meta-atoms.

Optical metasurfaces found their introduction a couple of decades ago [36, 37], along with the emergence of the field of metamaterials [38–41]. Metamaterials describe, and use engineered structured materials to exhibit, properties not directly found in the natural material itself. In the first electromagnetic metamaterials, the strong electric field and scattering properties of metals led to many interesting discoveries, for example, the realization of a negative index of refraction [42, 43], or the realization that Maxwell's equations on paper allow the exotic solution of a perfect electromagnetic invisibility cloak [39, 44]. Harnessing the intense electric fields on the surface of metallic nanoparticles, arranged in two-dimensional planes, led to the first generation of plasmonic metasurfaces [37, 45–47]. During this time, the subwavelength propagation and localization of light largely surpassed classical limits imposed by diffraction [48, 49]. However, plasmonic metamaterials have been strongly held back by the intrinsic optical losses of metals.

1.2.1 Mie resonances in dielectric nanoparticles

Since circa 10 years, dielectric materials started to play a more prominent role, as high-refractive-index nanoparticles support a rich variety of Mie resonances with minimal losses [50–52]. All-dielectric resonant metaphotonics employs a range of electric and magnetic Mie resonances for the manipulation of light [53], that occur when the wavelength inside the particles (or meta-atoms) becomes comparable to its spatial dimension, $2r \simeq \lambda n$, where r is the nanoparticle radius, λ the wavelength of the light, and n the nanoparticle refractive index. Figure 1.5 presents an overview of the fundamental Mie

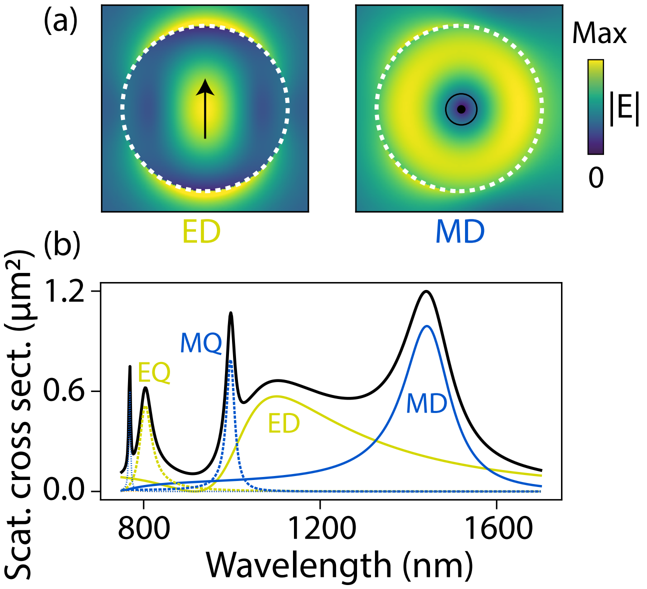

Figure 1.5: Calculation of the fundamental Mie resonances in a dielectric nanosphere. a) COMSOL simulation of the absolute electric near-field for a nanosphere with radius $r = 200$ and refractive index $n = 3.45$ in air. The left panel shows the electric dipole (ED) mode, oriented along the vertically polarized driving field that is propagating horizontally. The right panel shows the magnetic dipole (MD) mode, characterized by a circular electric field pattern, oriented orthogonal to the driving field. b) Analytical calculation of the scattering cross section for a similar nanosphere. The black solid curve shows the total magnitude, whereas the blue (lime) curves denote the magnetic (electric) contributions. The dotted curves indicate higher order contributions (electric quadrupole, EQ and magnetic quadrupole MQ).

resonances in a dielectric sphere. An electric Mie resonance corresponds to the excitation of a discrete electromagnetic mode within the dielectric particle, in which the bound electrons collectively oscillate under the driving optical field. This oscillatory motion produces an internal field distribution analogous to that of a standing wave. The normalized electric field distribution is visualized in the left panel of Fig. 1.5a). The lowest order electric Mie resonance is often referred to as the electric dipole (ED), and points in the direction of the driving field. Interestingly, in the silicon nanosphere, the first order ED is spectrally not the lowest order mode. The first order mode resonating at the longest wavelength is the magnetic dipole (MD), that arises when the driving optical field induces a circulating displacement current. The MD points in the orthogonal direction from the driving field. The field distribution of the MD is visualized in the right panel of Fig. 1.5a). Already in a classic paper from 1908 [50], Gustav Mie analytically described the scattering of light from tiny particles. These analytical expressions are today known as Mie theory, and allow for calculating scattering and extinction cross sections of nanoparticles. Calculations for the scattering cross section of a dielectric nanosphere ($n = 3.45$ and $r = 200$ nm) are shown in Fig. 1.5c), together with the individual contributions of the separate Mie modes.

The resonant wavelength of the Mie modes in a dielectric sphere, are dependent on the radius and refractive index of the material (and surrounding medium) only. Figure 1.6 shows a calculation of the scattering cross section of the MD for increasing sphere radius. This property makes them ideally suited for the design and control of resonant modes. When nanoparticles are placed into a metasurface, they frequently lose their ideal spherical geometry, as practical implementations typically use blocks, disks, or asymmetric shapes. In such cases, strictly speaking, one can no longer refer to pure ED or MD modes. Nevertheless, the terminology persists in the field, with modes exhibiting predominantly ED-like characteristics still referred to as ED modes, and MD-like as MD modes.

1.2.2 Fano resonant metasurfaces

Early all-dielectric metasurfaces relied on isolated Mie resonances [54, 55]. The field soon progressed to explore modal interference of spectrally overlapping optical resonances, which lead to so-called Huygens metasurfaces. The Huygens principle is the idea that every point on a propagating wavefront can be treated as a subsequent source of spherical waves. The interference of these secondary waves defines the new wavefront. In classical optics, the Huygens principle can, for example, be used to describe diffraction or refraction. In nanophotonics, the concept is extended as subwavelength scatterers can be engineered in such a way that their electric and magnetic

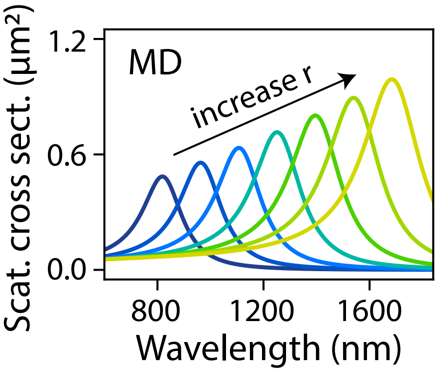

Figure 1.6: Analytical calculation for the MD contribution to the scattering cross section of a dielectric nanosphere of variable radius and refractive index $n = 3.45$ in air. Increasing the radius results in a redshift of MD resonance wavelength.

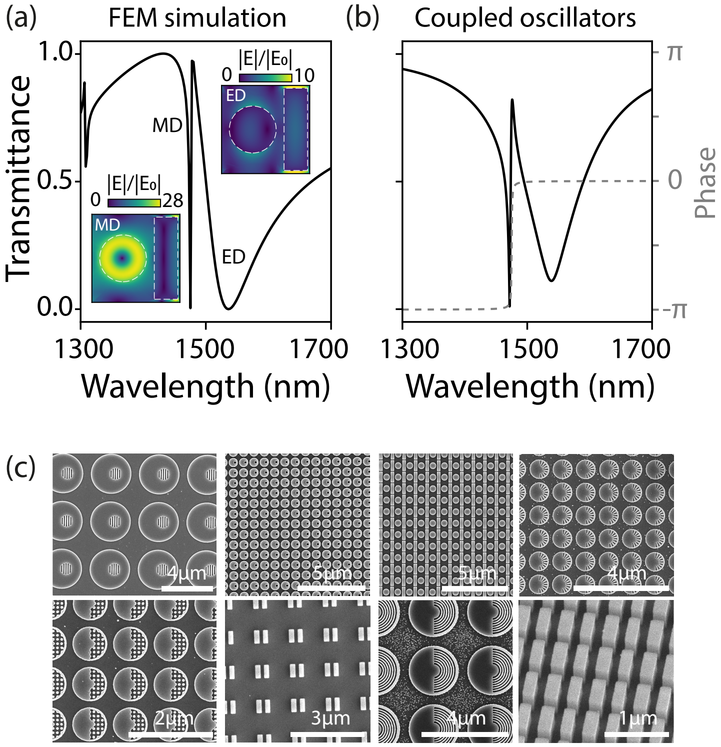

Figure 1.7: Fano resonant metasurface calculations and examples. a) Transmittance spectrum obtained via COMSOL simulation in which the broad ED around 1535 nm and the narrow Fano resonance, due to the coupling of the MD, around 1475 nm are visible. The insets show the electric near-field enhancement at the resonant wavelengths of the MD mode (left bottom) and ED mode (top right). b) Transmittance spectrum in solid black line, obtained via a coupled oscillator calculation with oscillator 1 at resonant wavelength $\lambda_1 = 1535$ and with $Q_1 = 15$, and oscillator 2 at $\lambda_2 = 1475$ and with $Q_2 = 1300$, coupling constant $\kappa = (180\,\frac{2\pi\,c\,Q_2}{\lambda_2})^2$, with c the speed of light, and leakage $f = 1.6$. The dashed gray line represents the phase of the second oscillator, which rapidly changes from $-\pi$ to 0 through the Fano resonance. c) SEM images of Fano-resonant silicon metasurfaces that are fabricated in the AMOLF Nanolab, demonstrating the versatility and creative design freedom enabled by this rich photonic platform.

dipole responses radiate with a certain tailored amplitude and phase. By treating the individual Mie modes at the nanoparticle positions as point-like secondary Huygens sources, a wide range of possibilities emerge to shape the phase, amplitude and polarization of the scattered wavefront at will. This modal interference has lead to phenomena such as uni-directional Kerker scattering [56], non-radiating anapole modes [57] and examples of very strong Fano resonances [58–60] or quasi-bound states in the continuum (quasi-BIC) resonances [61, 62]. A Fano resonance occurs when a dark mode interferes with a bright mode. The dark mode is a very high (or infinite) quality factor Q mode, such as a dipole pointing into the excitation direction (and therefore is not accessible), or a diffracted order in the plane of the array (which is referred to as the Rayleigh anomaly [63]). The bright mode can be a low Q mode, such as an in-plane dipole, that is associated with the same nanoparticle, or it can be spatially separated from it and located in a secondary nanoparticle. Figure 1.7a) shows a transmittance spectrum, calculated via finite element method (FEM) simulations (COMSOL Multiphysics 5.2), for a silicon disk-bar metasurface on glass [58]. The typical Fano lineshape occurs due to the interference of the out-of-plane MD at the disk near 1475 nm (electric near-field visualized in the left bottom inset) and the in-plane ED near 1535 nm (visualized in top right inset). A quasi-BIC arises when a true bound state in the continuum is perturbed. This is typically achieved by introducing a tunable asymmetry parameter embedded in the geometry, and thereby opening a controlled radiation channel that allows the dark mode to scatter into the far field [62, 64–67].

Both Fano resonances and quasi-BIC can be described by a coupled oscillator motif. This coupled oscillator framework captures the interference between a broad or bright mode (or continuum) and a narrow or dark mode (or bound state) [68, 69]. A calculation of a transmittance spectrum for two coupled oscillators, with oscillator 1 at resonant wavelength $\lambda_1 = 1535$ and $Q_1 = 15$, and oscillator 2 at $\lambda_2 = 1475$ and $Q_2 = 1300$ is presented in Fig. 1.7b). The full coupled oscillator model is described in Appendix B of Chapter 3. A similar typical Fano lineshape is retrieved as the FEM simulation. The phase of the narrow oscillator (gray dashed line, axis on the right) rapidly undergoes a π phase-shift through the Fano resonance, which makes for the extremely sharp asymmetric lineshape. Fano resonances are not limited to metasurfaces with spatially separated modes or symmetric particles. As an example, Fig. 1.4c) presents a plethora of SEM images of all-dielectric Fano resonant metasurfaces that were fabricated in the AMOLF Nanolab.

All-dielectric (Fano) resonant metasurfaces have unlocked an extraordinary range of applications, including beam steering or wavefront shaping [70–72], holography [73], analog signal processing [74], amplitude and phase modulation [75, 76]. Additionally, metasurfaces have shown to be powerful in manipulation of light emission [77], polarization state conversion [78], and are especially significant for (refractive index) sensing [79–85], even at very small footprint [86, 87]. Non-resonant dielectric metasurfaces have also been proposed for interlaced or displacement metrology [29, 88], overlay metrology [11, 89], library-based super-resolution [90], and super-oscillatory displacement metrology [91].

Another particularly important metasurface realization that uses Fano resonances is found in the form of the **nonlinear metasurface**, where enhanced local fields and the metasurface design paradigms of Huygens principle and resonant meta-atom engineering enable efficient harmonic generation and ultra-fast optical control [92–94]. Normally, harmonic generation from solids requires bulky nonlinear optical crystals. The weak optical nonlinearity of solids means that long paths are needed for efficient nonlinear conversion (e.g., third-harmonic generation, sum- and difference-frequency generation), which in turn introduce phase matching constraints that can only be satisfied in specific optical crystals [95]. A main advantage of nonlinear metasurfaces is that, because of their ultra-thin geometry, they no longer require traditional phase-matching constraints [96]. Fano resonant all-dielectric nonlinear metasurfaces use the very strong local field enhancement that can be achieved in the meta-atoms, to generate acceptable harmonic conversion efficiencies, within the volume of the nanoparticles. These conversion efficiencies are orders of magnitude larger than those of unpatterned films at a comparatively low excitation intensity [97–101]. The facile engineering of (interfering) resonances in these dielectric structures gave rise to a broad array of interesting applications for nonlinear metasurfaces, such as nonlinear beam steering [102], holography [103], resonant chiral effects [104], entangled photons [105, 106], vector beams [107], imaging [108], and dynamic image tuning [109, 110].

1.2.3 Fourier microscopy

Many of the aforementioned nonlinear metasurfaces applications posses interesting beam-shaping capabilities, such as steering light in specific direction. Alongside this, optical scatterometry metrology techniques rely on measuring the angular distribution of light. To observe directionality of emitted light from resonant metasurfaces, or in optical scatterometry context, a technique is required that can capture both the magnified real-space image as the angular distribution of the scattered light. This technique is used extensively in the work presented in this Thesis, and is called **Fourier microscopy**. Real-space microscopy (sketched in Fig. 1.8a) uses a conventional microscopy setup in which an infinity-corrected microscope objective, together with a tube lens, projects a magnified image of the sample onto the camera sensor. Each microscope objective is characterized by a specific NA and, when combined with a tube lens of a corresponding focal length, provides a defined magnification. The NA is related to the collection angle of the scattered light according to

$$\mathrm{NA} = n \, \sin(\theta) \tag{1.1}$$

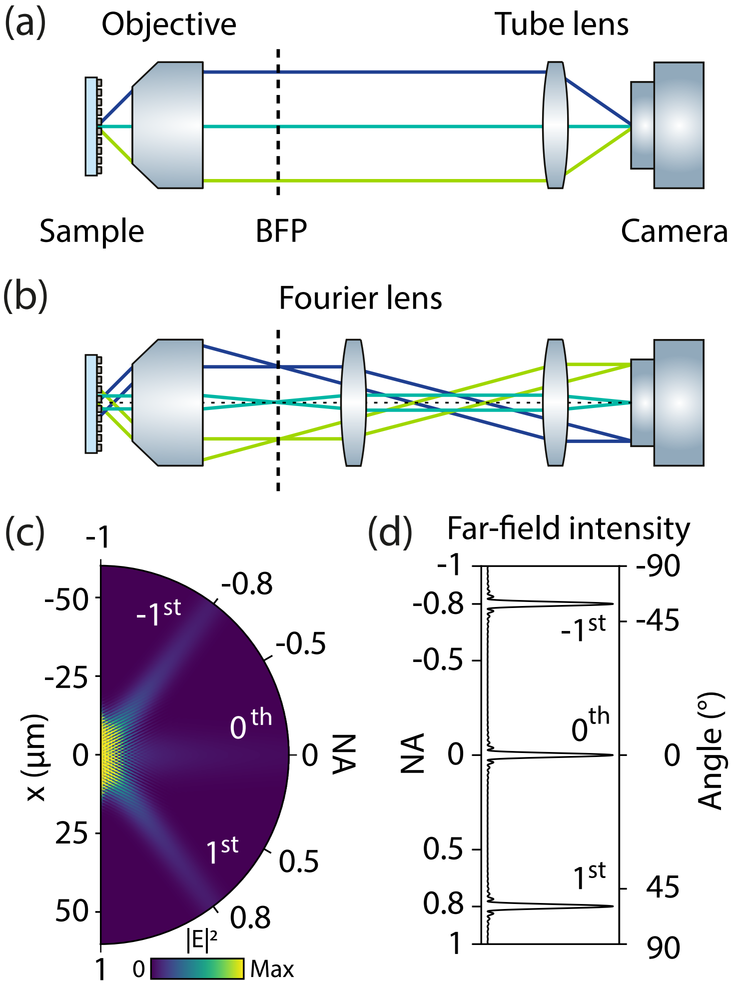

Figure 1.8: Fourier microscopy schematics. a) Conventional real-space microscopy projects a magnified image via an objective-tube lens combination on a camera sensor. The different colored lines represent various emission angles, which converge to the same position on the camera if they originate from the same point in the sample. b) Inserting a so-called Fourier lens, focused at the BFP of the objective, projects the various emission angles from different regions of the sample, onto the same position on the camera. c) Example calculation for the light intensity of a line of point emitters, illustrating diffraction from a grid. The interference guides the light in discrete diffraction orders, which are captured by the objective, and projected onto the camera. d) The camera records the far-field intensity, where NA (or emitted angle) corresponds to position on the camera sensor.

with n the refractive index of the medium between the objective and sample, and θ the angle from the optical axis. Equation 1.1 directly dictates the maximum angle of the collected light cone. Objectives with a high NA therefore capture a broader angular distribution and are preferred in Fourier microscopy, as they provide a greater amount of directional information. Inserting a secondary lens with its focal plane coinciding with the back-focal plane (BFP) of the objective, images the Fourier space onto the camera sensor. As sketched in Fig. 1.8b), each propagation *angle* (indicated by different colors) maps to a specific *position* on the camera, enabling direct extraction of angular information. Figure 1.8c) shows an example calculation of the electric near-field intensity for a line of point scatterers (such as Mie dipoles, pointing out of the plane) emitting spherical waves, with a Gaussian excitation mask. The coherent light is diffracted into specific propagation angles determined by the periodicity of the structure, given by

$$\theta_m = \arcsin\left(\frac{-m\lambda}{p}\right) \tag{1.2}$$

for diffracted order m, at wavelength λ and grating pitch p. For $p = 1000$ nm and $\lambda = 800$ nm, the light of the first order $m = 1$ is diffracted at an angle $\theta_1 \simeq 53°$, corresponding to an NA of 0.8. The camera in a Fourier-microscopy setup translates the spatial axis of the camera linearly to NA, visualized in Fig. 1.8d). Because of the inserted Fourier lens, the diffracted light from the line grating forms discrete far-field diffraction orders, which are imaged by the camera sensor.

1.2.4 Nonlinear metasurfaces

Nonlinear metasurfaces enhance light-matter interactions via resonant nanostructures, enabling harmonic generation through both bulk nonlinearities in the nanoparticle material (mostly for dielectrics) and strong surface nonlinearities driven by localized fields (mostly for plasmonics). In dielectrics, these nonlinear optical phenomena arise from the response of the bulk material's polarization to the local electric field, when the local field is sufficiently strong. At high field intensities **E**, the polarization **P** no longer scales linearly with the electric field, and is described with a nonlinear expansion

$$\mathbf{P} = \mathbf{P}^{\mathrm{L}} + \mathbf{P}^{\mathrm{NL}} \tag{1.3}$$

with the linear polarization $\mathbf{P}^{\mathrm{L}} = \epsilon_0\, \chi^{(1)}\, \mathbf{E}$, where ϵ_0 is the vacuum permittivity and $\chi^{(1)}$ the material linear susceptibility. The nonlinear polarization [95] is given by

$$\mathbf{P}^{\mathrm{NL}} = \epsilon_0\Big(\chi^{(2)}\mathbf{E}^2 + \chi^{(3)}\mathbf{E}^3 + \chi^{(4)}\mathbf{E}^4 + \cdots\Big) \tag{1.4}$$

with $\chi^{(n)}$ the nth-order nonlinear susceptibility. The nonlinear polarization $\mathbf{P}^{\mathrm{NL}}$ drives a nonlinear current $\mathbf{j}^{\mathrm{NL}} = \frac{\partial \mathbf{P}}{\partial t}$, which in turn generates nonlinear emission at harmonic frequencies $n\omega$ of the form $\mathbf{E}_n(n\omega)$. As $\chi^{(n)}$ are relatively small compared to $\chi^{(1)}$, linear optical effects dominate in most cases with low electric field strengths [95, 111]. The nonlinear polarization becomes significant, only when the local electric field $\mathbf{E}$ is sufficiently large, owing to the higher-order power dependence on the field amplitude. Dielectric (Fano) resonant metasurfaces can relatively easily support large field amplitudes inside the nanoparticles, as is clear from the inset of Fig. 1.7a), making them highly suitable for nonlinear metasurface applications.

The second-order nonlinear susceptibility $\chi^{(2)}$ is responsible for nonlinear optical effects such as optical rectification and second-harmonic generation (SHG) [112]. Dielectric materials with non-centrosymmetric crystal structures possess a nonzero second-order susceptibility [95, 112]. Notable examples of such $\chi^{(2)}$ materials, used for nonlinear metasurfaces, include (Al)GaAs [107, 113] and $LiNbO_3$ [114–117]. The third-order nonlinear susceptibility $\chi^{(3)}$ is responsible for nonlinear optical effects such as the Kerr-effect and third-harmonic generation (THG) [95]. Interestingly, a common thread across many works on dielectric nonlinear metasurfaces is the widespread use of a single $\boldsymbol{\chi}^{(3)}$ semiconductor material from which to build the meta-atoms. This back-bone of modern high-performing all-dielectric metasurfaces offers a compelling combination of properties. This material has a relatively high refractive index, negligible absorption in the infrared, excellent compatibility with existing semiconductor fabrication processes, and it constitutes the bulk of virtually all modern-day chips. **Silicon** has established itself as the material of choice for many resonant (nonlinear) metasurfaces [93, 96, 97, 118, 119]. The widespread use of silicon in both the semiconductor industry and nonlinear metasurfaces presents a notable opportunity: can we leverage the fundamental advances in nonlinear metasurfaces in the nanophotonics domain for the benefit of semiconductor metrology?

1.2.5 Metrology with nonlinear metasurfaces

Due to the low absorption of silicon in the (infra)red, current metrology platforms typically operate with visible or infrared wavelengths in a linear setting (IR/VIS in $\rightarrow$ IR/VIS out) [9]. As discussed in Section 1.1.2, optical scatterometry offers the highest throughput, but is inherently bound by the diffraction limit. Shorter wavelengths (SHG or THG) that are produced by nonlinear metasurfaces could provide a promising route to surpass existing resolution limits. We envision two distinct scenarios in which metasurfaces are of interest, which hinge on two distinct physical principles. The first advantage is that the generation of shorter wavelengths trivially improves spatial resolution, through the dependence of the Abbe diffraction limit on wavelength. The second physical principle is that the nonlinear polarization, which is the source of harmonic generation, of order n scales to the algebraic power n of the local field enhancement at the pump frequency (Eq. 1.4). This

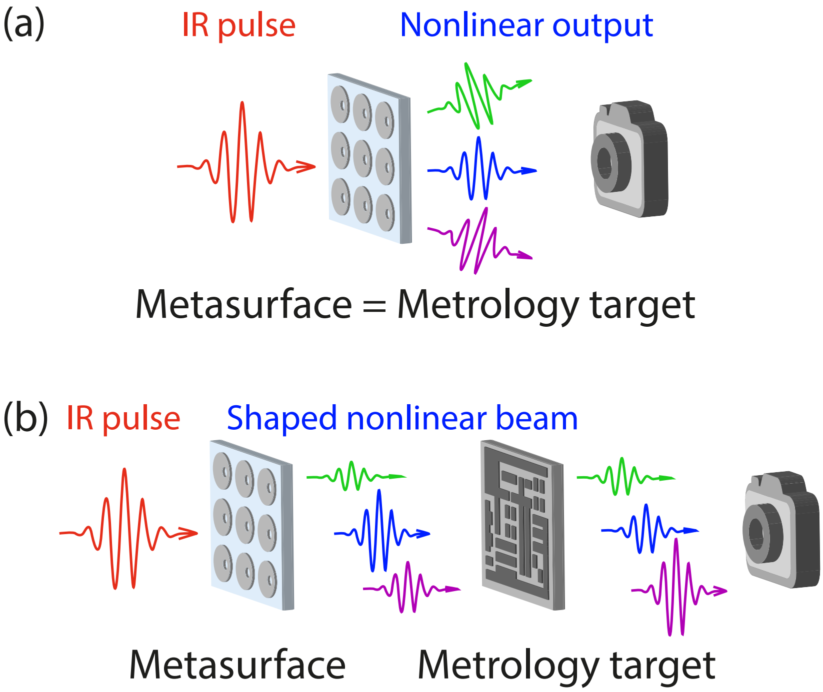

Figure 1.9: Two scenarios for the use of nonlinear metasurfaces in metrology. a) The nonlinear metasurface is the metrology target itself, excited by high-intensity ultrafast pulses to generate a harmonic output that directly relates to certain metrology parameters. b) The nonlinear metasurface produces a shaped harmonic beam that is designed for smart short-wavelength illumination of the metrology target, which is in this example in transmission, but also works in reflection.

potentially makes harmonic generation and emission exquisitely sensitive to the geometry of a generating metasurface, as it provides a highly nonlinear translation of the resonant near-field into a measurable far-field signal.

These two advantages directly present us two different opportunities for nonlinear metasurfaces in metrology, visualized in Fig. 1.9. The first scenario (Fig. 1.9a) uses the metrology target as the nonlinear light emitter (metasurface) itself. A high intensity ultra-fast light pulse excites the metrology target, and the harmonic output is captured. This scenario provides increased metrology sensitivity, as it relies on the algebraic power of the field to the induced nonlinear polarization, and thereby nonlinear current and emission [95]. Because nonlinear light generation is a coherent phenomenon, the nonlinear emission/diffraction can be extremely sensitive to small geometric variations in the nanostructured detail, through design of nanophotonic mode properties at both the fundamental and the up-converted frequency. A far-field measurement of the nonlinear light directly relates to an estimation of a metrology parameter, for which the measurement scheme was designed. This idea, for instance, underpins our patent application [120] wherein third-harmonic light from an asymmetric bar metasurface is proposed for a CD measurement. This scenario is closely related to harmonic generation microscopy which is an established technique [121], that can even go beyond the nonlinear diffraction limit [122]. However, our focus lies not on imaging, but on enhancing metrology parameter extraction.

The second scenario (Fig. 1.9b) envisions smart illumination of the metrology target with shorter-wavelength light to benefit from the concomitantly improved Abbe resolution limit. Crucially in this scenario the 'blue' (harmonic) light is not generated in the wafer at hand, but is generated prior to performing the scatterometry. This blue light could obviously be achieved simply by replacing the infrared laser that is commonly used with sources operating at shorter wavelengths. Indeed, for exactly this reason, alongside industry-standard infrared lasers, the industry also employs ArF lasers emitting at 193 nm and KrF lasers at 248 nm for metrology. However, if one wants to imprint certain interesting tailored spatial profiles for smart or optimal illumination for metrology, this might lead to the problem that blue and UV beams are more difficult to shape due to increased absorption and performance limitations of conventional optics at shorter wavelengths. For instance, it is well known that scatterometry and microscopy can be improved by using structured light with non-trivial intensity distribution (*e.g.*, donut beams), phase profiles (*e.g.*, orbital angular momentum beams) and polarization structure (*e.g.*, vector beams), as reviewed by [123]. In a separate development, the community of random optical media has developed the concept of wavefront shaping, in which the concept of optimally informative structured illumination for metrology has been proposed [124]. Nonlinear metasurfaces allow the emission of cleverly engineered harmonic beam profiles for smart interrogation of a metrology target (visualized in Fig. 1.9b). In this setup, an IR pulse could excite a specifically designed metasurface to produce a shaped harmonic beam, that illuminates a metrology target for highly sensitive and informative parameter estimation, benefiting from both the enhanced resolution provided by short-wavelength light and the concept of optimal illumination.

1.2.6 Dynamic light control: beyond the fixed function

In the course of exploring the intersection between metrology and nonlinear metasurfaces, we identified the use of metasurfaces as controllable nonlinear light sources as a particularly compelling direction. The relevance is not limited to metrology, but extends to any application that benefits from shaped ultraviolet light. Nonlinear metasurfaces offer the remarkable quality to shape and design a variety of harmonic beams [125–128], even controlling directionality of the nonlinear emission [102]. However, a main drawback

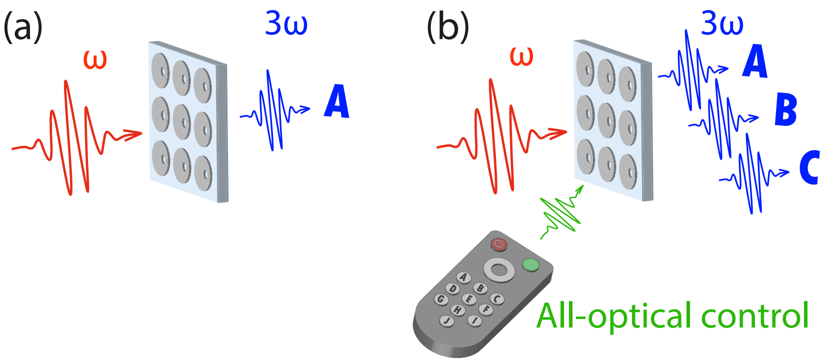

Figure 1.10: Dynamically tunable harmonic output. a) A static metasurface generates a harmonic beam profile corresponding to its intended design, by excitation with an ultra-fast light pulse. b) By applying a second light pulse, the harmonic output (spatial beam profile or directionality) can be dynamically controlled, enabling a wide variety of smart illumination techniques with just a single nonlinear metasurface, at ultra-high speeds.

of metasurfaces is that their function is fixed at fabrication. Significant effort has gone to researching approaches to change or modulate metasurface function dynamically, often referred to as active of tunable metasurfaces [129–132]. Dynamic functionality in active metasurfaces is often achieved by mechanical alteration or actuation [133, 134], temperature changes [135], electric gating [136, 137], phase-change materials [138, 139], modulation of the dielectric environment [140], and tuning of the optical nonlinearity [141]. While some of these techniques can provide high contrast, most of them tend to be slow and perform poorly at the required wavelengths, particularly in the blue and ultraviolet ranges. An alternative, ultra-fast approach, involves refractive index switching by photo-excitation of carriers, commonly referred to as all-optical modulation, tuning or switching [142–147]. All-optical tunability of metasurface functionality often requires a second femtosecond pulse to modulate metasurface properties, leading to switching behavior at timescales of the duration of the laser pulses. Figure 1.10 illustrates the concept of all-optical modulation of nonlinear emission from a metasurface. The static metasurface produces a certain fixed harmonic output (Fig. 1.10a), whereas a secondary control pulse (represented by the remote control in Fig. 1.10b) dynamically tunes the harmonic output profile. In this vision, an interesting harmonic beam profile can be dynamically shaped with ultra-fast speeds, with applications to interrogation of metrology targets, or any other dynamic blue light source applications.

1.3 Motivation and outline of this thesis

Throughout this Thesis, Fano resonant metasurfaces serve as a unifying platform for a range of investigations that span the boundaries of linear and nonlinear nanophotonics. These resonances, with their sharp lineshapes and intense local field enhancements, form the foundation from which we set out to explore how to advance optical metrology and dynamical nonlinear light control. This naturally triggers deep curiosity and ignites a series of questions. In what ways can the intense local fields be harnessed for metrology? What insights lie hidden in the nonlinear optical response of such metasurfaces, where harmonic generation is not only shaped by geometry, but also by their intricate interplay of ultra-fast dynamics and modal coupling? To what extent does the temporal nature of the driving field influence this response, and how can we use that dependency to control nonlinear output? How might we transform metasurfaces from passive scattering targets to act as active nonlinear sources? How could we, ultimately, with the speed of light, dynamically imprint tailored spatial profiles or steer nonlinear emission, turning light itself into a dynamic tool for next-generation metrology and beyond? These questions form the motivating thread through this Thesis, and will be answered in the following set of chapters:

- In **Chapter 2**, we focus on critical dimension metrology using quasi-BIC resonances. These resonances produce sharp Fano lineshapes that have the advantageous property of being extremely sensitive to minute geometrical changes of the meta-atom architecture. We show a unique approach to determine deep subwavelength feature sizes, on the order of industry standard CD. The approach relies on linear transmission measurements of metrology targets that consists of dielectric disks, with an asymmetrically induced void (or hole), thereby creating the quasi-BIC resonance. The void is structurally filled with nanoscale features under interrogation, and variations in the feature width translate to resonant wavelength shifts. In this Chapter, we present both experimental and simulated results for different *structure-in-void* metasurface designs, and attribute the spectral change of the resonance to the sensitivity to an effective refractive index in the void of the meta-atom. This approach could revolutionize CD metrology as it works at the high throughput of optical scatterometry with strongly increased optical contrast, while performing at the high resolution of SEM, and it could be directly applicable in the current production lines.
- In **Chapter 3**, we study third-harmonic generation from a similar disk-hole quasi-BIC metasurface, exploring the path to nonlinear optical metrology. Here, we analyze how the bright and dark modal interference and pulse properties influence the nonlinear output, and show that nonlinear metasurface design cannot be seen separately from

its external driver. Our experiments show imbalances in third-harmonic diffraction efficiencies and non-Gaussian third-harmonic spectral features that exhibit strong variations near the fundamental Fano resonance. We explain the salient physics of these observations via a coupled-oscillator model that captures the interplay between the driving field and the nonlinear response of the modes. The model provides a predictive framework to exploit the modal interplay for optimizing tunable third-harmonic diffraction efficiency. The results presented in this Chapter establish pulse-engineered metasurfaces as a powerful platform for nonlinear wavefront shaping and frequency conversion applications, while simultaneously pointing out opportunities and pitfalls for nonlinear optical metrology, where engineered metrology targets can translate pulse properties into highly geometry-sensitive, tunable signals.

- In **Chapter 4**, we explore all-optical modulation of nonlinear output via a secondary femtosecond pulse, to lay the foundation for dynamic control of nonlinear generated light. We study third-harmonic generation from silicon Fano-resonant metasurfaces and modulate the metasurface resonance by free carrier excitation induced by absorption of a 800 nm pump pulse, leading to up to 93% suppression of third-harmonic generation. Modulation and recovery occur on (sub)picosecond timescales. According to a Drude model to describe the refractive index upon carrier excitation, the pump-induced refractive index change blueshifts the metasurface resonance away from the generation pulse, causing a strong modulation of third-harmonic conversion efficiency. The principle holds great promise for spatio-temporal programmability of nonlinear light generation and paves the way for spatially engineered dynamical UV wavefronts for ultra-small semiconductor metrology.
- In **Chapter 5**, we show the realization of ultra-fast nonlinear beam shaping, using spatially structured pump light to control the TH emission profile and directionality. We use a digital mirror device inside a pump-probe setup that allows spatial pump patterns of a visible light pulse to spatio-temporally coincide with an infrared probe pulse onto an all-dielectric Fano resonant metasurface. The infrared pulse is tuned near the Fano resonance to generate strong third harmonics, and the pump pulse locally deactivates harmonic generation. The scattering of spatially periodic pump patterns convolve with the TH diffraction pattern, which generates satellite orders that evidence coherent emission and directional control. This work opens the door to ultra-fast precise control over harmonic beam profiles and directionality at generation stage.

Chapter 2

Structure-in-Void Quasi-BIC Metasurface for Deeply Subwavelength Nanostructure Metrology

Fano lineshapes associated to quasi bound-state-in-the-continuum resonances, that are supported by dielectric metasurfaces, have the advantageous properties of being extremely sensitive to minute geometrical changes in the meta-atoms. We show a unique approach to determine deep subwavelength feature sizes, comparable to semiconductor critical dimension metrology, by structurally infilling a void of a dielectric disk-hole metasurface design. Our simulated results show a sensitivity of 40.5 nm resonant wavelength shift for a 1 nm feature width (i.e. critical dimension) change, at an optical linewidth of 1.8 nm. We present both experimental and simulated results of different void infillings and attribute the spectral change of the resonance to the sensitivity to an effective index in the void of the meta-atom, which arises from the filled volume fraction and the material boundaries orientation relative to the local polarization. Treating our metasurface as an effective index sensor, the sensitivity is 262 nm$\cdot$RIU^{-1} and the figure of merit is 146 RIU^{-1}, which underlies the pronounced resonant wavelength shift driven by similarly large changes in the effective index caused by extremely tiny critical dimension variations. This approach could impact critical dimension measurements in semiconductor metrology, as it works at the high throughput of optical measurements while performing at the high resolution of scanning electron microscopy.

2.1 Introduction

Fano resonances in optical dielectric metasurfaces have uniquely advantageous properties for manipulating optical near- and far-field responses. Fano resonance lineshapes generally arise from the interference between a broad continuum of states (such as a broad scattering resonance or background radiation) and a narrow discrete resonance (such as a high-Q Mie mode) [59, 68, 148]. The quality factor Q and overall line shape can be exquisitely controlled by, for instance, combining broad dielectric Mie resonances to shape the continuum [71], with exquisite tailoring of the radiative damping of the narrow resonance by using, e.g., multipole resonances [58, 149], guided mode resonances [150, 151], or controlled symmetry breaking [62, 152, 153]. As Fano resonances carry a strong near-field, a nontrivial phase response, and often also wave vector selectivity, they allow for the shaping and manipulation of wavefronts [154, 155], efficient harmonic generation [97, 156], very sensitive refractive index sensors [157–160], and other applications [161, 162]. An efficient strategy for generating strong resonances has proven to be the engineering of quasi-bound states in the continuum (quasi-BIC) metasurfaces [67, 163–165]. The main principle of a BIC is the vanishing coupling between a discrete resonant mode and all radiation channels, called the continuum, which is generally the background radiation. The most common approach starts with a symmetry-protected BIC metasurface, using a periodic design that supports a Bloch mode prohibited from radiating due to symmetry constraints. Building on such a dark mode - which lacks radiation damping and thus has a nominally infinite Q-resonances can be unveiled by introducing a slight asymmetry in the unit cell or superlattice. This asymmetry opens a radiation channel, allowing the mode to radiate [166]. As the original BIC becomes leaky, it is referred to as a quasi-BIC [62]. It is well established that by tuning the geometric asymmetry, one can tailor the quality factor and resonant wavelength at will [165]. By choosing a specific geometric asymmetry one could, for example, use a quasi-BIC metasurface as a sensitive gas-sensor, by tracking the resonant wavelength as a function of surrounding refractive index [167]. These examples show the strong responsivity of quasi-BIC metasurface resonances to tiny perturbations in the nanostructure or surrounding medium.

2.1.1 Semiconductor metrology

Nanolithography techniques can achieve resolutions down to tens of nanometers in scientific settings, (electron beam lithography), while the semiconductor industry is pushing the limits below 5 nm, with sub-nm accuracy using extreme ultraviolet technology [1–4]. Metrology, the science of measuring and determining specific geometrical or dimensional parameters, plays an essential role in the semiconductor industry [4]. Commercial lithography demands metrology techniques that match the accuracy of the lithography process itself. Chip fabrication involves numerous sequential steps, each requiring precise dimensioning and alignment [1, 9, 11]. Manufacturing efficiency in terms of yield, and thereby resource utilization crucially depends on the ability to perform exquisite quality control at every stage. In the semiconductor industry, this quality control is achieved through metrology. The economic impact of improved yield through faster and more accurate metrology is immense: with a global annual revenue of \$600 billion in lithography, even a 1% improvement in yield represents a value of \$6 billion [30]. A wide range of structural parameters are of interest for metrology, including individual layer thicknesses, relative alignment of different layers (so-called interlayer overlay), feature sidewall angles, line-edge roughness, and more [9]. Among these, one of the most fundamental parameters is the critical dimension (CD), which represents the width of the smallest feature size of a nanostructure. CD measurements at the highest spatial resolution can be achieved with scanning electron microscopy (SEM). To employ it, wafers need to be taken out of a production line: While CD-SEM provides excellent accuracy, it suffers from low throughput, potential beam-induced damage, and SEM-specific error sources such as drift and inaccurate beam placement due to charging effects [4, 9, 168]. There is hence a large role for optical methods. Optical methods are noninvasive and nondestructive, and the fact that they are capable of delivering very high throughput ($\sim$0.1 s [9]) means that they are routinely applied in the manufacturing loop, screening every wafer either after resist development or etching. However, optical methods are fundamentally constrained by the diffraction limit. The challenge is to extract values for geometrical parameters with (sub)-single digit nanometer accuracy while using visible wavelengths.

2.1.2 Optical scatterometry targets

Optical metrology is typically performed not on actual devices but on dedicated targets that are specifically designed for efficient, fast, and accurate measurements. The target design includes important similar features of the actual functional device, without fully replicating it, to extract the most useful information. These metrology targets are patterned in the same litho-step as the functional integrated circuits and are placed in the scribe lanes of a wafer, spatially separated from and located between the devices. By choosing the right design, position and orientation, the important metrology information of the targets can be reliably extrapolated to the device features [9]. Some targets are designed to extract multiple metrology parameters, while others are tailored for a single task. Depending on the application, a single wafer can include dozens to hundreds of metrology targets for measuring alignment- and overlay errors, CD (variations) and surface roughness, among others. The most common optical approach for determining CD relies on spectral measurements of specially designed periodic nanostructure scatterometry targets, using a library-based approach to reconstruct grating parameters. These techniques require prior knowledge of the grating's periodicity and approximate structural parameters. Indeed, the crucial distinction between general imaging and reconstruction problems is that metrology seeks to accurately determine the value of a single parameter given as complete knowledge as possible of the sample geometry. It is this crucial distinction that enables beating the diffraction limit by several orders of magnitude. For instance, diffraction based metrology (based on measuring grating diffraction efficiency) is widely used in metrology to determine overlay errors (i.e. relative interlayer alignment with ASML Yieldstar [22]) with single digit nanometer accuracy. Diffraction based scatterometry is also effective—even with very low optical contrast—for CD measurements for features above tens of nanometers, but accurately measuring CD at the single-digit nanometer scale with high throughput remains an open challenge. To address the growing demands of modern semiconductor metrology, new solutions are required that reach both the high throughput capabilities of scatterometry and the sub-nm resolution provided by SEM. These requirements ask for the development of optical metrology techniques that give strong transmission or reflection contrast to reach fast and accurate readout, while maintaining a minimal wafer footprint that is suitable for the integration in advanced metrology workflows. This Chapter is motivated by the notion that metasurface designs can present competitive optical scattering targets for metrology. For measurements on 'telltale' scattering targets to be relevant, their design must meet a set of demands: 1) the targets must include feature sizes that are comparable to those in the device, 2) they should occupy minimal footprint to preserve valuable wafer real estate, and 3) they should allow for rapid measurements to support high-throughput processes. Meeting these criteria directly impacts the yield by reducing the number of faulty devices, increasing the available area for functional integrated circuits, and enabling measurements within a shorter time frame.

2.1.3 CD metrology with resonant metasurfaces

In this Chapter, we present a method for optically determining the CD of dielectric nanostructure patterns with deeply sub-diffractive periodicity and single-digit nanometer widths, achieving sub-nanometer sensitivity based on the concept of quasi-BIC metasurfaces. The method is based on studying the spectral response of the metasurfaces composed of dielectric meta-atoms featuring an asymmetrically placed semi-circular void, which induces a quasi-BIC, while the void itself is embedded with the structures under test (satisfying requirement (1) above). We report both simulations and experiments, reaching a simulated sensitivity of 40.5 nm at 7 nm feature size resonant wavelength shift per 1 nm increase in CD. This theory is supported by experiments on prototype samples (experiments at 1.5 μm wavelength, at larger

CD values). We attribute the observed shifts in the Fano resonance to the exceptional refractive index sensitivity of quasi-BIC metasurfaces. Structural changes of the subwavelength nanostructures, such as variations in width, modify the effective refractive index of the meta-atom structure-in-void, leading to a pronounced resonance shift. We substantiate this understanding by analyzing Fano resonance shifts for structure-in-void metasurfaces with meta-atoms that consist of different shapes, where the subwavelength patterns are aligned either along or perpendicular to the local polarization. By mapping the data onto the effective index using a polarization-dependent effective index model, we demonstrate that all sensitivity curves converge onto a single master curve. Our findings introduce a unique approach for detecting ultra-small feature variations in deeply subwavelength gratings embedded within dielectric metasurfaces. Although the mechanism that we identify is akin to reported sensing of refractive index changes in gases and liquids by BIC metasurfaces, the performance metrics are different: the standard approach to BIC index sensing is to work at very high quality factors Q, in turn requiring semi-infinite spatial extent. Instead, metrology targets must occupy only a small spatial footprint (requirement (2) listed above). Therefore we developed a method that works at low quality factor Q, and equivalently poor angular resolution. Despite low Q, in our approach small variations in CD produce pronounced shifts in the reflection or transmission spectrum. The approach is fully compatible with existing diffraction-based metrology workflows at very high speeds (requirement (3) above) and offers immediate applicability in advanced semiconductor manufacturing. While conventional methods rely on scatterometry on non-resonant sub-diffractive gratings to reconstruct grating parameters, our approach harnesses the strong electric field confinement of quasi-BIC metasurface resonances. In essence, current metrology targets used in scatterometry can be seamlessly integrated into a structure-in-void metasurface platform to enhance optical contrast from just a few percent to several tens of percent. This improvement enables higher yield through faster measurements, and more accurate estimation of critical dimensions down to the single-digit nanometer scale.

2.2 Structure-in-void metasurface

Figure 2.1 shows the main concept of our metrology proposition, which is based on a metasurface comprising high-index disks with an asymmetrically placed structure-in-void illuminated by white light to measure a transmission spectrum. It is well known that such a disk system with a symmetrically placed hole can support a symmetry-protected BIC mode, which becomes optically accessible in the far field, and turns into a quasi-BIC, upon introducing an asymmetry by off-center placement of the hole [67, 110, 166, 169]. Similar disk-hole structures have been proposed for dynamic nonlinear im-

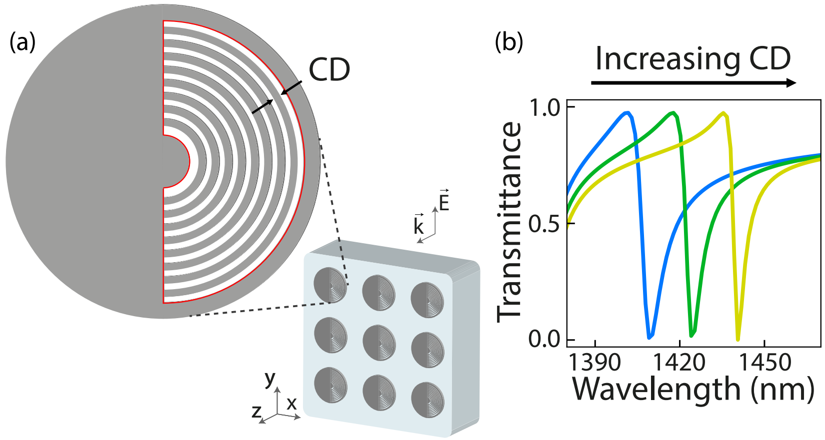

Figure 2.1: a) Schematic illustrating the core concept. We illuminate a quasi-BIC metasurface –composed of thin silicon disks (height h = 75 nm, radius r_d = 400 nm, pitch p = 995 nm) with an asymmetrically placed structure-in-void– on a quartz substrate using white light to measure the transmission spectrum. The void area is illustrated by a red solid border. The spectral response is highly sensitive to tiny geometrical variations in the structure-in-void's grating width, or CD, which modulates the effective index. b) Simulated transmittance spectra for CD = 13.3 nm (blue), 16.6 nm (green) and 19.9 nm (yellow), indicating a clear redshift of the Fano resonance as per increasing CD.

age tuning [110] – where the dark mode is attributed to a magnetic dipole resonance with out-of-plane magnetic moment – and cube-hole structures for a polarization-independent sensor [170]. Strong resonances can occur in a variety of similar structures with asymmetrically placed air holes, involving magnetic dipole resonances, electric quadrupole resonances, and toroidal dipole responses [164]. Experimentally, for such structures, quality factors up to $\sim 5{\cdot}10^3$ can be obtained at $\lambda \sim 1500$ nm, tuneable by the placement and size of the hole. In our work, the goal is not to maximize Q by minimizing size and optimizing placement of the hole, as metrology targets requires functionality at the small footprint of only a few unit-cells, which inherently reduces the quality factor. We rather use the hole area as the metrology target region where we embed a deeply subwavelength grating with a known periodicity, similar to current sub-diffractive metrology gratings, to measure the unknown CD. Therefore, we focus on designs in which the hole is semi-circular and extends over nearly half of one side of the disk, showing that the prototype already functions well at relatively low Q. The nanostructures under test are placed in the void, forming what we refer to as the structure-in-void metrology sensor. Throughout this chapter, any references to placing, filling, or embedding structures refer strictly to the design stage of the metasurface geometry. All features of the design are fabricated in a single lithography step. These terms do not imply any physical post-processing steps for infilling such as post-fabrication mechanical insertion, a second lithography and lift-off step, or material infiltration.

In the field of quasi-BIC metasurfaces one usually defines an asymmetry parameter α according to meta-atom geometry, for instance defining $\alpha = 1 - (r_d - d)/r_d$, where d is the distance of the hole from the center of the disk of radius r_d. Since in our case, we are not interested in the placement or size of the hole per se, but in measuring the structure-in-void parameters, we instead define $\alpha = 1 - FF$, where FF is the nanostructure fill factor, determined by the fraction of volume of the embedded nanostructure in the meta-atom's void relative to an empty void $FF = V_{Si}/V_{void}$. The fill factor FF ranges from 0 (empty void) to 1 (completely filled void, symmetric disk, resulting in $\alpha = 0$). In the example case of Figure 2.1a), the void is filled with eight azimuthally oriented lines (concentric grating) of circa CD $\simeq$ 16.6 nm, at a period of 33.1 nm ($\alpha = 0.5$). Figure 2.1b) shows three calculated transmittance spectra for CD = 13.3 nm, 16.6 nm and 19.9 nm, (FF=0.4, 0.5 and 0.6) where a clear red shift of the Fano resonance is visible for increasing CD.

2.3 Infrared transmittance simulations

Figure 2.2a) presents finite element simulations (COMSOL Multiphysics 5.2) for the normal-incidence transmittance through a structured void metasurface with $N = 8$ lines, where we increase the thickness of the concentric rings to obtain fill factors from $FF = 0$ to 1. We solve for the system assuming poly-crystalline silicon meta-atoms in air on glass ($n_{air} = 1, n_{glass} = 1.44, n_{Si} = 3.45$), placed in an infinite square array of pitch $p = 955$ nm. A detailed description of the simulation is presented in the Methods section 2.7. The meta-atoms are illuminated from the glass side with polarization along the vertical axis (y-axis in Fig. 2.1a), perpendicular to the horizontally placed asymmetry), inducing an asymmetric electric near-field on either side of the meta-atom. This asymmetry drives a circulating electric current that is associated to an out-of-plane magnetic Mie dipole, which is visualized by a ring in the normalized electric field (inset of Fig.2.2c). The transmittance is calculated as the energy flow from input port (in the glass) to output port (air). At $FF = 1$ (symmetric disk, completely filled void) the metasurface supports a vanishing symmetry protected BIC, however by introducing an asymmetry (reducing the FF to 0.9), a sharp resonance occurs near 1500 nm wavelength of $Q = 3 \cdot 10^3$. Such high Q-values are typical for quasi-BIC resonances with very low asymmetry values [163]). The quasi-BIC resonance red shifts and significantly broadens upon increasing the asymmetry (decreasing FF), reaching a wavelength of 1380 nm and a $Q = 200$ at zero fill factor. This behavior is archetypical for symmetry-protected quasi-BIC metasurfaces. A second spectral feature is found around 1370 nm, which does not show a vanishing linewidth as the asymmetry is removed. This feature is associated

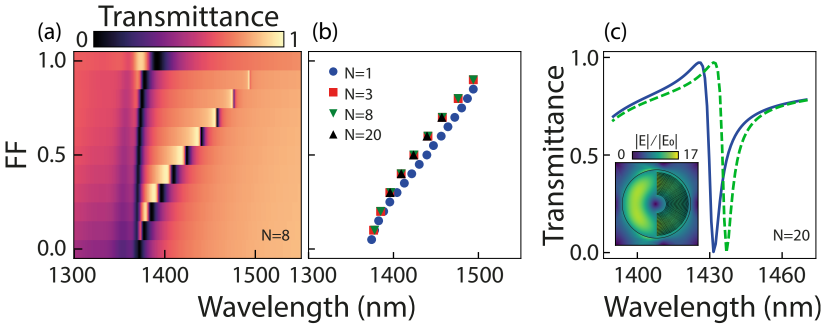

Figure 2.2: Simulated spectral response of a structure-in-void metasurface, composed of meta-atoms of disks with an embedded concentric grating in the asymmetrically placed void (illustrated in Fig. 2.1a), as a function of fill factor. The variable N denotes the number of concentric rings in the grating. a) Transmittance spectra for N=8, for fill factor FF on the y-axis ranging from 0 (fully asymmetric/empty void) to 1 (no asymmetry/completely filled void), corresponding to CD ranging from 0 nm to 33.1 nm. A blue-shift and broadening of the asymmetric Fano line shape is clearly visible for decreasing FF. A somewhat broader resonance is relatively wavelength independent and present around 1370 nm. b) Fano-dip tracking for $N = 20, 8, 3$ and 1, plotted as a function of FF (on the y-axis), in which it is clear that similar behavior is found for all N. This result enables us to scale up the nanostructure CD for experimental purposes, demonstrating proof-of-principle measurements that operate similarly for very small CDs in industrial applications. c) Transmittance spectra for $N = 20$, for two fill factors $FF = 0.55$ (blue solid) and 0.56 (green dashed) corresponding to CDs of 7.29 nm and 7.42 nm respectively, which shows a 5.4 nm wavelength shift of the Fano resonance for a 0.13 nm increase in CD. At this wavelength the optical linewidth is 1.8 nm, with $Q = 805$. The inset shows the simulated electric near-field $|E|$, normalized to the incoming electric field $|E_0|$, for a single meta-atom with $N = 20$ ($FF = 0.56$) at the Fano dip of 1437nm.

with a Rayleigh anomaly (RA), where the meta-atom bright mode mediates grating diffraction into glass.

We focus on the quasi-BIC and examine the transmittance for structure-in-void metasurfaces for meta-atoms with varying coarseness of the azimuthal line pattern $N = 1$, 3, 8 and 20 concentric grating lines. Note that for each value of N, the periodicity of the nanostructure is well-defined, as it is given by the void radius divided by the number of concentric grating lines. This results in a unique mapping of FF to CD. The embedded nanostructure CD ranges from 0 nm at $FF = 0$ to 265 nm ($N = 1$), 88.3 nm ($N = 3$), 33.1 nm ($N = 8$), and 13.3 nm ($N = 20$) at FF = 1. To underline the generalization of the resonance shift behavior as a sensing mechanism to CD variations, we track the Fano dip as a function of FF in Fig. 2.2b). Similar behavior for $N = 3, 8$ and 20 is found, while the $N = 1$ case shows a small deviation from the common behavior, though being qualitatively similar. On basis of this simulation result, we hypothesize that the Fano-resonance is primarily sensitive to the fill factor of the nanostructure in the void, which in the spirit of homogenization theory is equivalent to measuring effective index of the void volume. For prototype experiments in this work we test the concept for modest numbers of lines, compatible with the CD values that can be achieved in standard academic electron beam lithography processes. On basis of the numerical simulations we argue that the concept extrapolates to large N, *i.e.*, to the very small CD that can not be achieved in an academic cleanroom, and that may be achieved only in industrial settings. This scaling allows us to experimentally validate the concept while demonstrating proof-of-principle measurements that function similarly for very small CDs in industrial applications. As industry has a need for "at-resolution" metrology, *i.e.*, metrology on structures with the same dimensions as device structures, this is an essential capability. Figure 2.2c) presents simulated transmittance results for a metasurface with $N = 20$ azimuthal lines for $FF = 0.55$ and $FF = 0.56$, which is on par with industrial resolution limits. The small change in fill factor corresponds to a change in CD of 0.13 nm, from 7.29 to 7.42 nm. This minute geometrical change causes a resonance shift of circa 5.4 nm in wavelength. Given the quality factor $Q = 805$ at this fill factor, already a full optical linewidth shift of 1.8 nm is reached upon 0.05 nm CD variation, which is smaller than the lattice spacing in crystalline silicon. This strong fill factor dependence evidences an extremely high sensitivity for the readout of geometrical variations, even for much lower quality factors due to finite-size arrays with a footprint of <10 μm, that would be practically considered in metrology applications. Appendix C reports on 10×10 (20×20) unit-cells simulations, which reveal $Q \simeq 25$ ($Q \simeq 89$) at a modest $FF = 0.55$, which still corresponds to an optical linewidth shift at single (sub) nm-sized CD variations.

2.4 Experimental realization

We fabricated metasurfaces in 75 nm thick polycrystalline silicon, evaporated on fused quartz, via a standard electron beam lithography procedure. This height was chosen to approach ultrathin layers that are used in industry, while maintaining enough material to excite the out-of-plane MD associated to the quasi-BIC resonance. A detailed description of the nanofabrication procedure is found in the Methods section 2.7. The metasurfaces consist of meta-atoms placed in square arrays (995 nm pitch) with disks of radius $r_d = 400$ nm and a semi-circular hole that covers almost half one side of the disk, stretching from $r_1 = 100$ nm to $r_2 = 365$ nm. We created a variety of embedded nanostructure patterns including azimuthal line gratings, radial spokes and dot patterns, where we vary the fill factor and the number of elements N within the constraints of the e-beam lithography resist (step size 5 nm and minimum gap size/CD 20 nm).

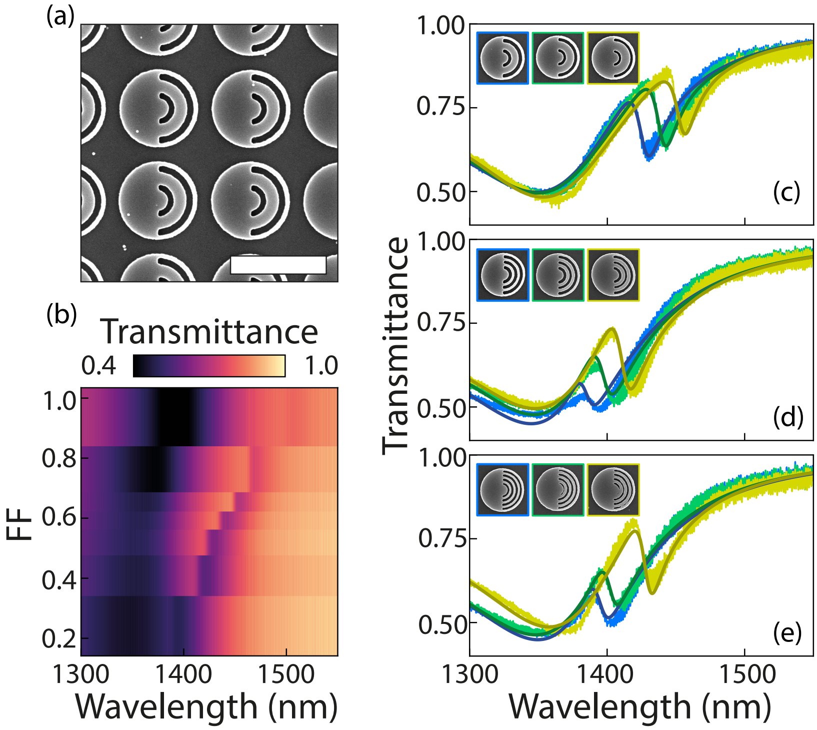

Figure 2.3: Experimental realization of a structure-in-void metasurface with $N = 1$, 2 and 3 azimuthal lines. a) SEM image for $N = 1$, $FF = 0.51$ (scale bar 1 μm). Metasurface parameters are height $h = 75$ nm, $r_{disk} = 400$ nm, with a void that covers almost half of disk reaching from $r_1 = 100$ nm to $r_2 = 365$ nm, with a single azimuthal line embedded in the void that is centered at $r = 230$ nm and has a width of CD = 130 nm. b) Transmittance spectra for $N = 1$ azimuthal line nanostructured void metasurfaces with FF on the y-axis ranging from 0.24 to 0.94. c) Spectra for $FF = 0.51$ (blue),0.61 (green) and 0.63 (yellow), showing a clear shift in resonant wavelength, accompanied by insets of SEM images of their individual meta-atoms, bordered by corresponding colors. The solid line shows a Fano lineshape fit. d) Spectra for $N = 2$ azimuthal lines structure-in-void metasurfaces with $FF = 0.31$ (blue), 0.40 (green) and 0.48 (yellow), showing a similar trend, with the inset showing SEM images of individual meta-atoms. e) Spectra for $N = 3$ azimuthal lines, $FF = 0.40$ (blue), 0.52 (green) and 0.60 (yellow).

2.4.1 Infrared transmittance experiment

Figure 2.3a) shows a scanning electron micrograph (SEM) image for a metasurface where meta-atoms have $N = 1$ azimuthal line in the void. The azimuthal line is centered at a radius $r = 230$ nm from the metasurface origin, and ranges in width from 64 nm ($FF = 0.24$) to 249 nm (almost filling the entire hole, $FF = 0.94$). Figure 2.3b) presents transmittance spectra (x-axis) as a function of FF (y-axis). Transmission measurements are performed in a home-built microscope setup that loosely focuses white light onto the metasurface from the glass side (f = 30mm, NA$\sim$ 0.05), while collecting many angles on the air side with an objective (NA 0.9, 100x, Nikon, CFI Plan Apo BD) and projecting the image onto a multi-mode fiber (core size 100 μm) that feeds into a Fourier transform optical spectrum analyzer (Thorlabs, OSA202C). Throughout this work, the FF is determined from SEM images by image analysis, using a thresholding procedure described in Appendix A. Incident white light is polarized along the vertical axis (y-axis in Fig. 2.1), allowing excitation of the quasi-BIC mode. Similar Fano line shapes between 1380 and 1500 nm as in the simulation are found. A broad spectral feature at around 1360 nm is found at all asymmetries that is associated with the Rayleigh anomaly, while to the red of the Rayleigh anomaly the quasi-BIC is observed. As in the simulation the quasi-BIC broadens and blue shifts with increasing asymmetry (decreasing FF). Features appear much broader than in the simulation, as in the experiment we loosely focus on the sample, causing an averaging over a cone of excitation angles, while additionally introducing finite footprint that fundamentally constraints quality factor (see Appendix C for 20×20 unit-cell simulations, that reveal a simulated $Q \simeq 89$, which is close to the measured Q). Furthermore, since our academic e-beam lithography tools inherently introduce CD variations within a metasurface, all resonances are smeared out across the range of resonances that occur due to the variations in the fabricated CDs [171]. Spectral fringes of ca. 1.3 nm are observable in the experiment, which are likely caused by a Fabry-Perot effect from the quartz substrate. The fringes are not present in the simulation, which assumes an infinite quartz substrate thickness.

Three transmittance spectra for estimated $FF = 0.51$, 0.61 and 0.63 are plotted in Fig. 2.3c), accompanied by insets of SEM images of their corresponding individual meta-atoms. A shift of 27.5 nm in resonance wavelength is found for a FF change of 0.12, which corresponds to 229 nm/FF change over the region around FF = 0.55, or $\Delta\lambda/\Delta d = 229\ \text{[nm]}/265\ \text{[nm]} = 0.86$ nm resonant wavelength shift for 1 nm change in CD of the single azimuthal line (while $Q = 112$, so the optical line width of the resonance is 13 nm). Assuming identical sensitivity to fill factor for higher N one can estimate the sensitivity for the $N = 20$ case, where $\Delta d = 13.1$ nm, meaning $\Delta\lambda/\Delta d = 17.4$ nm resonant wavelength shift for a 1 nm change in thickness. This number is a factor two lower than the COMSOL prediction, which may be caused by rough estimation of experimental FF. Figure 2.3d) presents transmittance spectra for a metasurface with $N = 2$ instead of just $N = 1$ azimuthal lines embedded in the void, accompanied by insets of SEM images of corresponding unit cells. The estimated fill factors are $FF = 0.31$, 0.40, 0.48. Similar transmittance spectra are plotted in Fig. 2.3e), where the amount of azimuthal lines in the meta-atom void is $N = 3$, and the estimated $FF = 0.40$, 0.52 and 0.60. The measured sensitivity of this $N = 3$ metasurface is $\Delta\lambda/\Delta d = 3.6$ nm resonant wavelength shift per 1 nm CD increase, which means a shift of one optical linewidth of 10.3 nm is reached with a CD increase of 2.87 nm. Depending on the signal-to-noise ratio of a measurement protocol, even with this relatively simple design, sub-nm CD variations are within reach.

2.5 Effective refractive index

To investigate our hypothesis that FF, or more precisely, effective index, is the dominant contributing factor that determines the shift in the resonant response, we fabricated a plethora of different structure-in-void metasurface designs. Figure 2.4 presents both simulated and experimental results of the structural design study. Figure 2.4a) shows a finite element simulation of the electric near field ($|E| = \sqrt{E_x^2 + E_y^2 + E_z^2}$) normalized to the incoming electric field $|E_0|$ at $P = 1\text{W}$ ($|E_0| = \sqrt{\frac{2P}{c\epsilon_0 p^2}}$, with p the pitch) for a wavelength at the minimum of the Fano resonance in transmission for a reference structure, namely a disk-void metasurface where the void volume is filled with a homogeneous medium of refractive index n. This reference case is used to compare the effective index generated by structural infilling with line, spoke and dot patterns. The transmittance spectra (x-axis) for FF 0 to 1 (y-axis) are presented in 2.4b), where FF is directly converted to effective refractive index by $n = n_{air} + FF(n_{Si} - n_{air})$, ranging from $n = 1$ to $n = 3.45$ respectively.

2.5.1 Structural designs

In the structural design study presented in Fig. 2.4 we highlight five different designs: (c,h) Azimuthal $N = 1$ (concentric grating), (d,i) Azimuthal $N = 3$, (d,j) Radial $N = 2$ (spokes), (f,k) Radial $N = 8$ and (g,l) Pillars $N = 14$ (dots). These designs were chosen to probe the difference between small and large N, and also to understand the influence of the orientation of the features relative to the electric field of the dark mode. The Fano-resonance is attributed to the coupling to an out-of-plane magnetic dipole moment, which has an azimuthally oriented in-plane electric field circling the meta-atom center. Consequently, the near field is oriented along the material boundaries for azimuthal geometric features, whereas in the radial case, the polarization is orthogonal to the boundaries. The pillar case provides a mixture of parallel

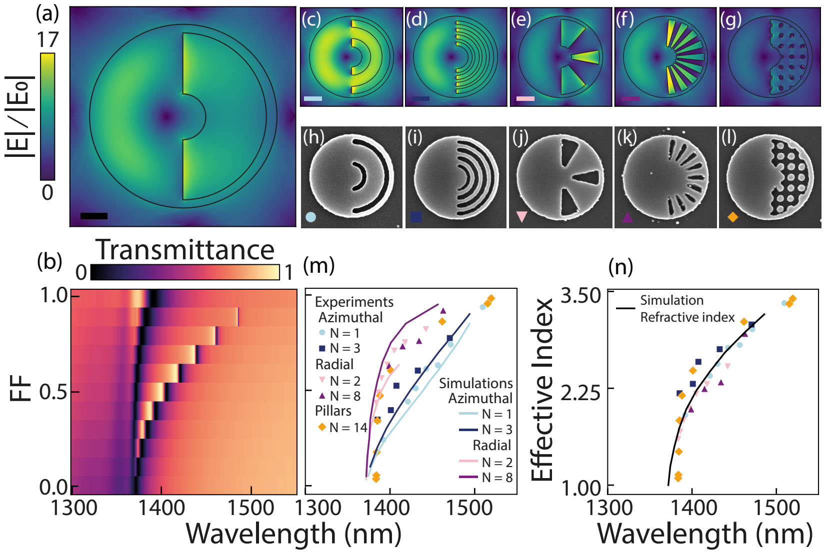

Figure 2.4: Structural design study of deeply subwavelength structure-in-void metasurfaces with near-field simulations, SEM images, and experimental Fano dip analysis. a) Simulated electric near-field distribution for a single unit cell in a periodic lattice, with a void that is filled with refractive index $n = 1.98$, normalized to the incoming electric field $|E_0|$, and b) the calculated transmittance spectra for $n = n_{air}$ ($FF = 0$) to $n = n_{Si}$ ($FF = 1$). c-g) Simulated normalized near-field distributions, at the Fano resonance minimum wavelength, for metasurfaces that feature designs of nanostructures embedded in the void: 1 azimuthal line (c), 3 azimuthal lines (d), 2 radial spokes (e), 8 radial spokes (f) and pillars (g), with color scale silimar to (a). h-l) SEM images of unit-cells, with the same designs as the simulated unit-cells. m) Fano dip track of the metasurface transmission as a function of FF. Experimentally extracted Fano dip wavelengths are plotted as solid markers, with colors matching the marker in the left-bottom corner in the corresponding SEM images. Simulated Fano dip tracks are plotted as solid lines, with colors corresponding to the line in the near-field simulation images. n) Fano dip track as a function of calculated effective index, revealing that most data align along a single curve, with the Fano dip track of the refractive index void filled metasurface of (a), plotted as the solid black curve. This indicates that the metasurfaces function as effective index sensors, detecting collective structural changes in CD that are sensed through effective index variations.

and perpendicular polarizations. One might expect different sensitivities in these three cases owing to the large difference in field boundary conditions, *i.e.*, owing to whether the perturbation is associated with a jump or with continuity in the electric field. In effective medium theory this difference expresses in different mixing formulas depending on the field orientation [172–174]. Figures 2.4 c-g) show simulated electric near-fields at the Fano minimum frequency, normalized to the incoming electric field $|E_0|$, for the 5 highlighted designs. The fill factors are $FF = 0.4$, 0.4, 0.43, 0.55, 0.4. The distinction in boundary condition is immediately evident: electric field jumps in the radial metasurfaces in e) and f) are clear, whereas the electric field is continuous for the azimuthal line patterns in c) and d). Moreover, the azimuthal (radial) designs allow a stronger enhancement of the field inside the silicon (gaps), and the pillars show an overall less enhancement. Figures 2.4 h-l) show SEM images of individual fabricated meta-atoms for all design cases, at fill factors $FF = 0.63$, 0.4, 0.56, 0.73, 0.47.

2.5.2 Experimental effective refractive index sensing

Spectral transmission measurements were performed on all metasurface designs and at many fill factors (all spectra are reported in Appendix B), from which we extract the wavelength of the Fano resonance minimum (Fig. 2.4m). Experimental results are plotted as solid markers alongside simulated results as solid lines (plot colors match the color coding in the left bottom corner of the SEM images and electric near field plots). All structural designs show a large sensitivity to geometrical change. At the same time one observes that different design families have very different responsivity curves: notable, the azimuthal designs have a similar responsivity across the entire FF-range, while the radial designs show high responsivity for large FF (above $FF \sim 0.55$, steepest part of the curves), and poorer sensitivity at small FF. The pillar structures response lies between these extremes. This result evidences that not simply the geometrical fill factor dominates the resonance shift. We attribute this difference to the fact that the simple mixing rule $n = n_{\text{air}} + FF(n_{\text{Si}} - n_{\text{air}})$ for the effective index n as function of fill factor FF is not accurate, and needs to be refined in dependence of the family of patterns. Indeed the same FF can correspond to quite different effective index values depending on the orientation of structural boundaries relative to the electric field, as is well known from the study of effective medium mixing rules for high-index contrast media (silicon and air) such as stratified stacks, nanopillar arrays and nanopore arrays with boundaries mostly following or perpendicular to the electric field. Such mixing rules have been studied extensively in the context of two-dimensional photonic crystals [172, 174, 175] and effective medium theory of stratified media [176, 177]. For such systems one can single out TE-polarized propagation (E-field along material boundaries) and TM-polarized propagation (H-field along boundaries, meaning the E-field is not continuous), and reported mixing rules are:

$$n_{\text{eff}}^{E} = [\varepsilon_a + FF(\varepsilon_b - \varepsilon_a)]^{1/2} \tag{2.1}$$

$$n_{\text{eff}}^{H} = \varepsilon_a \left[\frac{\varepsilon_a + (\frac{1+2FF}{3})(\varepsilon_b - \varepsilon_a)}{\varepsilon_a + (\frac{1-FF}{3})(\varepsilon_b - \varepsilon_a)}\right]^{1/2} \tag{2.2}$$

where ε_a (ε_b) is the permittivity of the two media, in our case air (1) and silicon (12.25), respectively. In the structure-in-void metasurfaces, polarization is given by the direction of the circulating electric field associated with the magnetic Mie dipole. The anisotropic structuring causes form birefringence, so that the effective index depends on the field alignment relative to the structure boundaries. Whether the electric field is oriented parallel or perpendicular to the material boundaries depends on the specific meta-atom design. We apply the effective medium mixing rules accordingly, selecting Eq. 2.1 to describe the effective index that is generated by azimuthal structures (where the electric field is mostly parallel to the boundaries) and Eq. 2.2 for radial structures (where the field is predominantly perpendicular). This allows to replot the Fano resonant wavelength shift as a function of the effective index, presented in Fig. 2.4 n). In the case of pillars we chose the effective index to be described as an average refractive index according to the FF as

$$n_{\text{eff}} = \varepsilon_a^{1/2} + FF(\varepsilon_b^{1/2} - \varepsilon_a^{1/2}) \tag{2.3}$$

which takes values in between n_{eff}^{E} and n_{eff}^{H}. For reference, we have also calculated the wavelength shift for the case of filling the void volume with a homogeneous medium of index n, according to the same average index equation 2.3. We observe that as function of effective index all tuning curves are much closer, essentially overlapping to within the error bars in our experiments. From this analysis we can draw two distinct conclusions.

First, the mechanism of sensing is essentially that the Fano resonance is ultra-sensitive to the effective refractive index of the structure-in-void n_{eff}, which arises from the deeply subwavelength nanostructure embedded in the void. To make our sensing scheme comparable to metasurface refractive index sensors that are used in i.e. biosensing [160, 178, 179] we examine the common parameter for sensitivity, which is wavelength shift per refractive index unit (RIU) change. For the structures at hand the sensitivity $S = \Delta\lambda/\text{RIU}$ evaluates as 262 nm / RIU for the simulated case of $N = 20$ azimuthal lines 2.2. With an optical resonance line width of 1.8 nm, this translates into a figure of merit (FOM, comparing the spectral shift per RIU given by S to the optical line width) of FOM$= 146$, which is comparable to reported optical sensors based on metasurfaces [159, 178, 180], but not outperforming recent works [167]. The fact that our prototype operates at relatively low Q (thus FOM), yet resolves filling factor variations below 0.1 (equivalent to a 1.3 nm CD change for a 7 nm nominal CD with $N = 20$ grating lines at a 13.5 nm pitch) demonstrates the strength of our design as a metrology platform. It effectively integrates previously unused resonances with established optical metrology techniques based on scatterometry of subwavelength gratings. While comparisons to metasurface refractive index sensors may provide useful context within the broader landscape of recent studies, our aim is not to compete on sensitivity benchmarks, but to introduce a new design strategy tailored to the demands of advanced wafer metrology.

Second, the local polarization dependence of the mixing rules provides some room to optimize sensitivity, or to gain information about the anisotropy and orientation of the embedded nanostructure. Aside from possible opportunities to sense shape anisotropies in lithography (comparing CD in different dimensions), the orientation dependence also provides a route to optimize sensitivity to CD, depending on the FF regime of interest. For instance, for $FF > 0.6$, sensitivities are twice higher for radially oriented structures, while at the same time the optical linewidth becomes very narrow.

Finally, we note that the experimental data and simulated data do not perfectly collapse on the tuning curve for homogeneous void volume filling. We attribute this deviation to the fact that we assumed mixing rules that were derived for bulk electromagnetic composite media. In contrast, the nanostructures in the void at hand are themselves deeply subwavelength in diameter and height (circa $\lambda/7$ in the xy-plane, and $\lambda/20$ in thickness), and in reality the modes in our structured void metasurface have boundaries both parallel and perpendicular to the electric field in all cases. We note that although the model provides a mechanistic understanding, it is not a substitute for full wave simulations. This furthermore holds for practical metrology applications, where the effective index approach could serve an insightful heuristic model, but cannot replace data fitting to rigorous spectral libraries.

2.6 Conclusion and outlook

In summary, we presented simulations and experiments demonstrating structure-in-void quasi-BIC metasurfaces as promising sensors for critical dimensions in extremely deeply subwavelength patterns, such as encountered in semiconductor lithography. The use of the void in quasi-BIC metasurfaces as a container for metrology to embed deep subwavelength structured systems has, to our knowledge, not been proposed before. Previous works have proposed quasi-BIC metasurfaces as highly sensitive refractive index sensors [84, 158, 160, 167, 181], with envisioned applications in IR spectroscopy and biosensing, and have extensively studied the influence of the position and size of meta-atom hole on the BIC response [164]. In semiconductor metrology, facile optical measurement on at-resolution structures to determine feature sizes with subnanometer resolution is in high demand, and a seemingly straightforward mechanism based on homogenization has, in fact, many benefits. It promises sensitivity to minute CD differences in patterns with deeply subwavelength-width lines and as a mechanism it is agnostic to the actual CD or pitch chosen. Indeed, the size requirements are on the meta-atom disks and the need to have a somewhat extended array, but not on the nominal periodicity of the actual structure that is subject to inspection. For sensing CD errors that are due to under/over exposure or underetching for instance, one can easily construct convenient readout scenarios on this basis: one can directly compare targets with different feature size (changing the line density, i.e., N) and identify if nominally identical fill factors FF indeed give identical response (or determine which exposures/etch conditions indeed give nominally identical fill factors FF). Additionally, one could envision the currently used library-based approach, which relies on very low contrast differences in spectral measurements, incorporating structure-in-void metasurfaces to take advantage of the strong resonance enhancements. Also, the sensing is to some degree robust: small changes in line orientation, line symmetry, variations in line width along the line length (i.e. CD variations, instead of just CD), or precise placements of the lines in the void will not strongly effect the response. As such it fits precisely the requirements of metrology: determining a single parameter (CD in this case) with maximum precision through prior knowledge (one needs to know the period or the number N, and rough line orientation and FF), and with maximum robustness against variations in other parameters. This should be contrasted to scenarios in which the task is to obtain a reconstruction with minimal prior knowledge of an unknown object placed in the void, as in an imaging or optical reconstruction task. For such tasks the structure-in-void metasurface approach is quite unsuited: The only sensitivity of the structured void metasurfaces that goes beyond effective index sensing is via the orientation dependence in the effective index mixing rule.

The designs presented here were chosen to combine a practical quality factor Q, for presenting a substantial area/volume available for sensing (ca. 35% of the meta-atom), and without any significant optimization efforts already present a simulated sensitivity of 40.5 nm resonant wavelength shift for 1 nm CD change, at 7 nm feature size (chosen as the current litho-node), with an optical linewidth of 1.8 nm. Experimentally we reached a sensitivity of 3.6 nm wavelength shift per 1 nm CD width change as our feature sizes were around 45 nm, resulting in one optical linewidth shift for a CD width change of 2.87 nm. We see many opportunities for further optimization. There are many meta-atom designs in the quasi-BIC toolbox where the asymmetry that opens the quasi-BIC coincides with high field confinement in a tight gap [167], which can thus embed a deeply subwavelength nanopattern. An interesting question is what design rules optimize sensitivity to particular patterns of interest. In this work we presented simple transmission as a read out mechanism. Instead one could also envision measuring nonlinear light generation, performing polarimetry on scattered light, interferometric readout [85], exploring off-normal incidence BICs, or reading out diffraction patterns. In this sense, special targets could be designed to measure alignment errors or astigmatism, or to determine other metrology parameters such as line- or surface roughness and side wall angle. To develop deployable metrology targets and raise the technology-readiness-level of our concept, some key fabrication-line challenges need to be addressed in an industrial setting. These challenges include statistical robustness against wafer-to-wafer variations, resonance drift due to chuck heating, photoresist residue and the influence of the stratified nature of the wafer to spectral behavior. Finally, we notice that in this work we used high-index metasurfaces. An open question is if these methods can also be translated to low-index contrast scenarios. In semiconductor metrology there is a crucial advantage to performing metrology on resists after development yet before etching, as opposed to after etching (when a wafer that does not meet the quality standard can no longer be used). The disk-void metasurface design could serve as a sensor, with resist nanopatterns embedded in the void through a two-step lithography process. While the tradeoffs between index contrast, spatial extent of the metasurface, and index sensitivity are not fully explored yet, a promising fact is that the basic mechanism of quasi-BIC formation also operates in low index gratings.

2.7 Methods

2.7.1 Metasurface Fabrication

A standard e-beam lithography recipe was used to fabricate the nanostructures. First, fused quartz substrates (12×12 mm, 500 μm thick, Siegert Wafer GmbH) were cleaned via sonication in water for 10 minutes, followed by immersion in a base piranha solution at 75 °C for 15 minutes. The substrates were then dipped in water and rinsed with isopropanol (IPA). We use the same recipe as in Appendix A, however, with two distinct differences. A 75 nm-thick polycrystalline silicon layer was deposited using e-beam evaporation (Polyteknik Flextura M508 E) by heating silicon pellets with an emission current of 90 mA to achieve a deposition rate of 0.1 nm/s. The samples were subsequently subjected to oxygen plasma treatment for 2 minutes to grow a thin passivation layer, which protected the silicon during development and enhanced adhesion to the resist layer. A ca. 40 nm-thick layer of hydrogen silesquioxane (HSQ) resist (Dow Corning, XR-1541 E-Beam Resist) was spin-coated at 4000 rpm (ramp rate: 1000 rpm/s) for 45 seconds and baked at 180 °C for 2 minutes. To mitigate charging effects during patterning, a thin conductive layer of 10 nm aluminium is evaporated by thermal evaporation (Polyteknik Flextura M508 E). This layer of aluminium does not influence patterning properties and is etched away by the resist-developer. Electron beam patterning was performed using Raith's Voyager system at 50 kV, with an average dose of 1500 μC/cm^2. The development process began with a 70-second immersion in TMAH at 60 °C, then two subsequent water rinses and one IPA immersion for 15 seconds each. Finally, the HSQ mask was transferred into the silicon via reactive ion etching (Oxford Instruments Plasma Technologies, Plasmalab 80 Plus) using a $CHF_3/SF_6/O_2$ gas mixture (15/10/3 sccm), a forward power of 150 W, and a chamber pressure of 7 mTorr, achieving an etch rate of ca. 45 nm/min. Excess resist was not removed, as it neither altered the optical properties nor significantly affected the experimental quality. Metasurface fields of a certain design are ca. 250×250 μm, with 100 μm distance to its neighboring field.

2.7.2 Experimental Transmission Measurements

Metasurface transmission measurements were carried out in a home-build transmission microscope. White light from a halogen source (Avantes, Avalight-HAL, 3602600 nm) passes through a linear polarizer (Thorlabs) and is loosely focused through the backside of the sample on the metasurface using a 30 mm working distance C-coated lens (Thorlabs). This setup approximates normal incidence excitation, minimizing the broadening of the quasi-BIC resonance caused by multi-angle illumination. Transmitted light with an NA of 0.9 is collected using a 100× microscope objective (Nikon, CFI Plan Apo BD) and subsequently focused with an f = 50 mm C-coated lens onto a 100 μm core multimode fiber. The sample is illuminated from the back side, as the collection objective has no coverslip aberration correction. Finally, the fiber feeds the collected light into an optical spectrum analyzer (Thorlabs, OSA202C). Reference measurements to generate transmittance spectra are taken adjecent to the metasurface fields.

2.7.3 Near-Field and Transmission Simulations

We use the RF module in COMSOL Multiphysics 5.2 to numerically solve Maxwell's equations for a system comprising polycrystalline silicon meta-atoms in air situated on a glass substrate ($n_{\text{air}} = 1,\ n_{\text{glass}} = 1.44,\ n_{\text{Si}} = 3.45$). The meta-atoms are arranged in a square lattice with a pitch of $p = 955$ nm, modeled using periodic boundary conditions to imitate an infinite extended array in the xy-plane. Void structures are parameterized using a fill factor, which scales the radius of azimuthal features or angular regions in the case of radial designs. This enables a parameter sweep over the fill factor combined with a frequency sweep, sampling 200 frequency points. Perfectly matched layers (PML) are implemented above and below the meta-atom plane along the z-axis, positioned at least twice the wavelength away from the structure, to effectively absorb outgoing scattered light. The system includes an input port and an output port defined at the interfaces of the glass and air regions with the PMLs, respectively. Transmission spectra are calculated by evaluating the transmitted energy flow from input port (in the glass) to output port (in air). The meta-atoms are illuminated from the glass side with an incident field polarized in the vertical direction. This polarization aligns perpendicular to the asymmetry of the meta-atoms, which is oriented horizontally.

Appendices

A Fill Factor estimation and image analysis procedure

The FF is estimated by using a thresholding procedure. In essence, this comes down to a script that reads a TIFF file that contains a SEM image of a structured void metasurface. Figure 2.5 shows a sequence of images, starting with a raw SEM image, and leading to the isolation of a single meta-atom, from which we determine fill factor. First, the contours in the metasurface SEM images are found by using an adaptive thresholding called cv2.adaptiveThreshold by OpenCV (version 4.9.0, Python version 3.9.13). This method uses small groups of neighboring pixels to find an optimal threshold value for each neighbor. Second, a circle is fitted to the image to find a disk radius and center. This is used as a mask of value 1 and multiplied with the original image, to extract only one meta-atom.

Next, for an isolated meta-atom we determine the fill factor by binarizing. Grey value pixels from the SEM image are binarized into a black and white (0 or 1) image by thresholding. The threshold value needs to be adjusted depending on the image, as many boundaries light up in SEM images. This means that the threshold value is determined per category of structured infillings. We found it judicious to decrease the threshold by 6 points per upwards step in the patterned fill factor for each structure stripe, accounting for the fact that features darken in SEM when boundaries are further apart.The tabulated base threshold values were chosen as follows for the lowest fill factors (An indicating Azimuthal with N=n, and R/Pil indicating Radial and Pillar structures):

A1	A2	A3	R2	R8	Pil
100	100	100	100	80	100

The result of such a procedure are shown in Fig. 2.6.

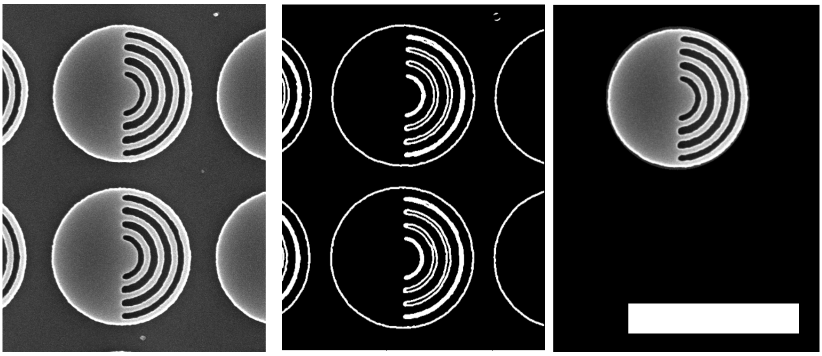

Figure 2.5: Illustration of procedure to isolate a single meta-atom for image analysis of its fill factor. Left: raw SEM image. Middle: boundaries identified by OpenCV. Right. Single meta-atom isolated by fitting a meta-atom outer boundary in the middle image, and masking. The scale bar in the right image denotes 1 μm.

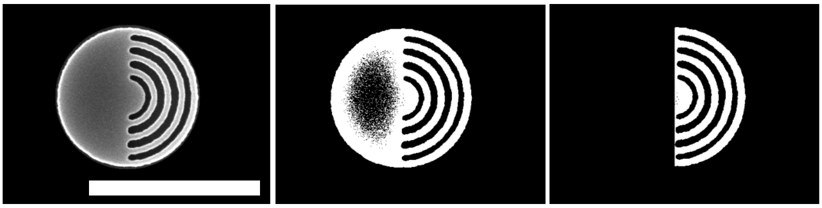

Figure 2.6: Illustration of procedure to determine fill factor. Left: single meta-atom isolated by image analysis (replicated from Fig. S1), scale bar denotes 1 μm. Middle: thresholded image. Right: Clip out for just the structured void part. The FF is determined by counting the fraction of white pixels in the semicircle.

Figure 2.7: Thresholded image for an FF=0 and FF=1 structure. These images are used to determine the area of the void, which is required to normalize to when determining the FF of structured voids.

Part of the large surface area on the unstructured left side is considered below the threshold value, even though it is ‘filled, an illustration of the statement that areas darken in SEM images as they are further away from boundaries. A typical example of this is shown in the middle image in Fig. 2.6. As we are interested only in the structured void part, we cut out only the right half of the circle. Next we count the number of white pixels, which we identify as silicon. To convert that into a FF, we need to ratio to the ‘fillable area, meaning we need to determine the area of the ’unfilled’ void. To do so, we examine SEM images for the FF=0 and FF=1 case with the same procedure. This provides the normalization to obtain a FF between 0 and 1, where FF=0 means the same amount of white pixels as the left image of Fig. 2.7, and FF=1 means the same amount of white pixels as the right image of Fig. 2.7.

The thresholding procedure introduces errors. In particular, the extracted FF values depend somewhat on the chosen threshold value. We note that decreasing thresholding values leads to systematic upward (approximately linear) shifts of extracted FF values. Therefore, the qualitative behavior of wavelength shift versus FF value changes does not change with thresholding, although the thresholding procedure may introduce a small systematic error in FF.

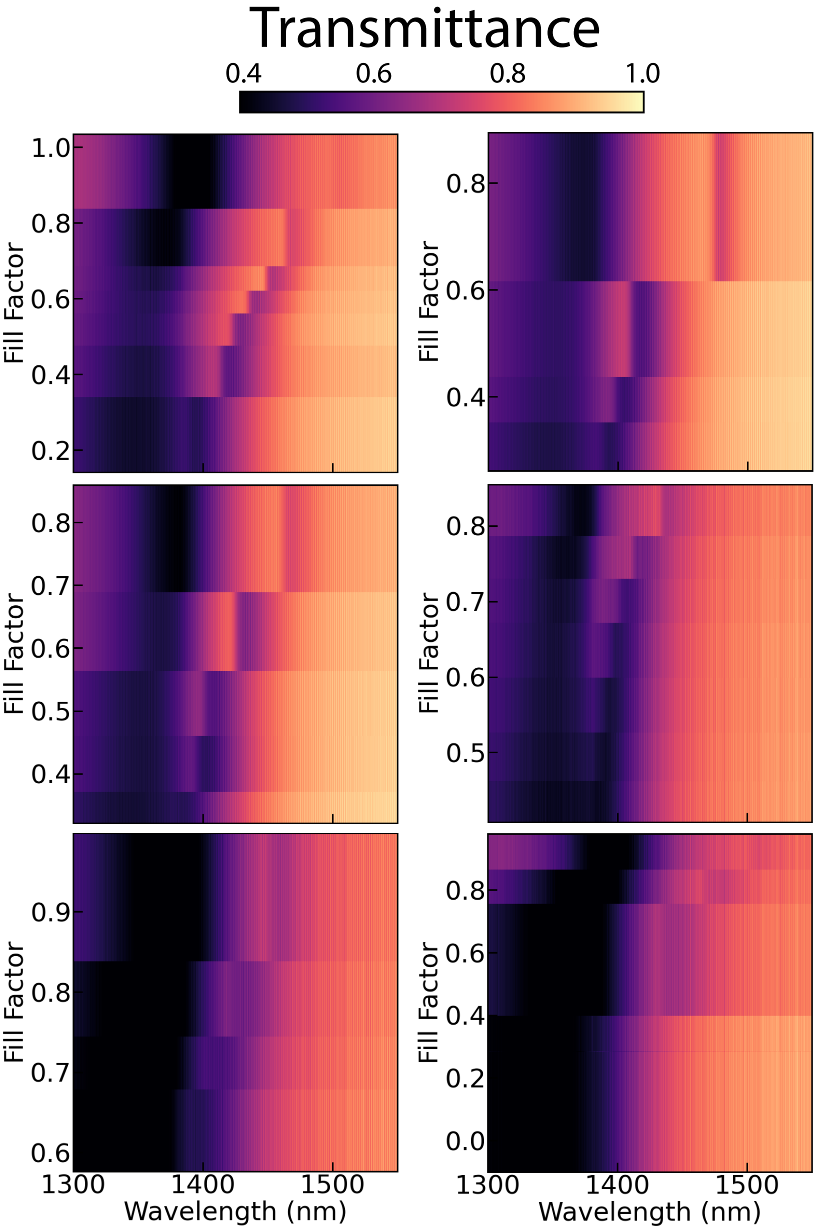

Figure 2.8: Experimental transmittance spectra for all fabricated structured-in-void metasurfaces. Wavelength is plotted on the x-axes in nm, fill factor FF on the y-axes and transmittance is represented by color, which is denoted by the colorbar on the top. Top left: Azimuthal N=1, top right: azimuthal N=2, middle left: azimuthal N=3, middle right: radial N=2, bottom left: radial N=8, bottom right: Pillars.

B All transmittance spectra

Figure 2.8 presents all experimental transmittance spectra (x-axes) as function of fill factor (y-axes) for all fabricated structure-in-void metasurface designs. Top left: Azimuthal N=1, top right: azimuthal N=2, middle left: azimuthal N=3, middle right: radial N=2, bottom left: radial N=8, bottom right: Pillars.

C Finite sized array simulations

The authors thank August Röell for providing finite-sized array simulations.

To assess whether a low quality factor Q arising from finite-sized metasurface arrays still (1) permits informative CD measurements, and (2) is primarily limited by measurement process or by the device footprint, we performed finite element simulations using JCMSuite. The simulations were performed using both the scattering solver and the open system eigenmode solver. The simulated systems all consist of a glass substrate and an air superstrate, both 900 nm thick, with the metasurface being 60 nm thick. Each meta-atom has a radius of 398 nm, and the meta-atoms are arranged in a square lattice with a lattice vector length of 953 nm. The mesh of the periodic simulations has a maximum side length of 175 nm in the substrate and superstrate,

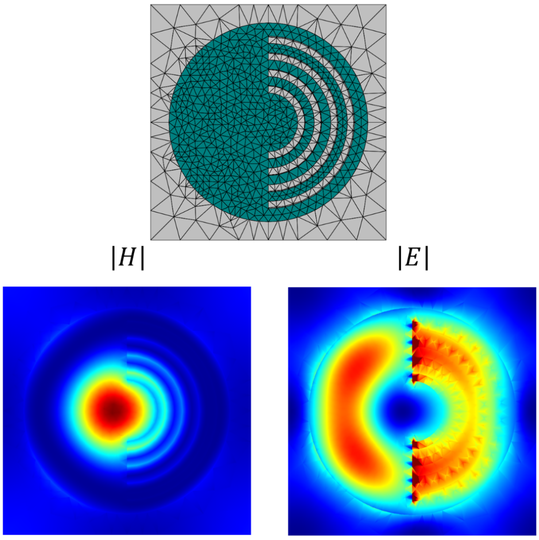

Figure 2.9: Top: Mesh of the periodic simulations. Bottom: Absolute value of the H- and E-fields of the eigenmode of a single unit cell of the metasurface in rainbow colormap blue (min) to red (max), with periodic boundary conditions in the X,-X,Y,-Y directions and transparent PML boundary conditions in the Z,-Z directions. The magnetic dipole mode is clearly visible. The eigenmode has a frequency of 1331.1 - 1.9002i THz. All calculations were performed using JCM, with finite element degree equal to 2, resulting in around 3×105 elements, 10 GB memory use, and a solving time of about 1 min on a typical PC.

and 44 nm in the metasurface. The mesh of the 20 × 20 finite array simulations has a maximum side length of 233 nm in the substrate and superstrate, and 59 nm in the metasurface. The simulation software uses open PML boundary conditions which are automatically generated. First, periodic structures were simulated to benchmark against our COMSOL simulations. We observed similar resonance behavior in both methods for the case of an N=3 azimuthal concentric grating with FF = 0.55. The magnetic dipole mode is clearly identified and visualized in Fig. 2.9, where the magnetic field |H| shows a strong spot which is pointing out of the plane (H Hz in this case) and the electric field |E| shows the typical ring.

Finite sized array simulations for 20 × 20 unit-cells at FF = 0.55, reveal through eigenmode analysis a similar magnetic dipole mode, which is visualized in Fig. 2.10. The magnetic dipole mode is clearly visible as strong spots in the magnetic field H and circles in the electric field E, which are similar to the periodic analysis. In the plane of the metasurface, at its edge, we add a buffer of one unit cell thick around the metasurface, and the computation is made more efficient by adding a perfect electric conductor symmetry plane (functioning as a mirror) in the -Y direction, duplicating the sample horizontally. We found an eigenfrequency of 1328.4 - 7.6378i THz, corresponding to a resonant wavelength of 1418 nm, with an expected linewidth of 16 nm and a quality factor $Q \sim 87$. Via Fig. 2.2b) we extrapolate this footprint-limited quality factor for an N=20 concentric grating metasurface, which shows that in a practical CD metrology application, still ∼0.5nm CD change results in a single optical linewidth shift.

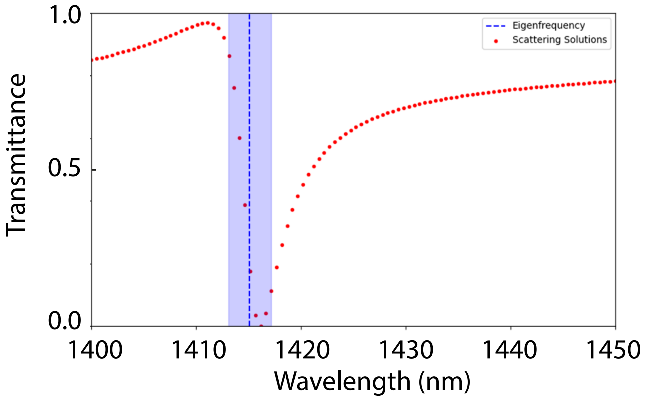

Figure 2.10: Transmission spectrum of the periodic metasurface around the Fano resonance. Every dot corresponds to the result of a scattering simulation. The vertical dashed line indicated the resonant wavelength as predicted by the eigensolver, and the shaded area around the resonant wavelength indicated the linewidth as predicted by the imaginary part of the eigenfrequency. We see a clear Fano lineshape, and a good correspondence between the scattering results and the predictions of the eigenmode approach. All calculations were performed using JCM, with finite element degree equal to 2. The eigenmode solution is identical to that of Fig. 2.9, and each of the 100 scattering simulations requires around 3 × 105 elements, 5 GB memory use, and a solving time of about 22 sec on a typical PC.

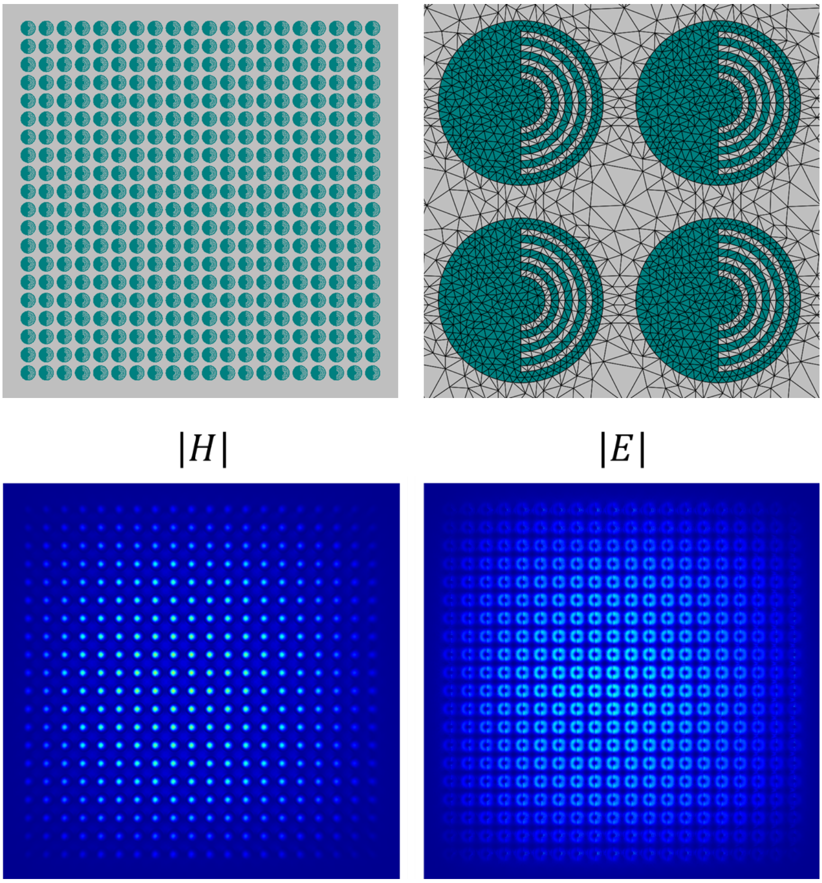

Figure 2.11: Top: The left image shows the 20 × 20 finite size array of the metasurface, while the right image shows the mesh used for the simulation, zoomed in on four meta-atoms. Bottom: The absolute value of the H- and E-fields of the eigenmode of a 20x20 finite sized array of the metasurface in rainbow colormap blue (min) to red (max), with transparent PML boundary conditions in every direction except the -Y direction, which defines a perfect electric conductor symmetry plane. The eigenmode has a frequency of 1328.4 7.6378i THz. All calculations were performed using JCM, with finite element degree equal to 1, resulting in around 6x106 elements, 110 GB memory use, and a solving time of about 1 hour on a typical PC.

Chapter 3

The Influence of Driving Pulse Properties on Third-Harmonic Diffraction from Quasi-BIC Metasurfaces

Quasi-bound states in the continuum in dielectric metasurfaces support sharp Fano resonances that emerge from the interference between bright and dark modes. We exploit this modal interplay to demonstrate tunable third-harmonic emission, controlled through the driving pulses wavelength and intensity. Our experiments show imbalances in third-harmonic diffraction patterns and non-Gaussian third-harmonic spectral features, that exhibit strong variations near the Fano resonance. We explain the observations via a coupled-oscillator model, that captures the interplay between the driving field and the nonlinear response of the modes, explaining our observations and providing a predictive framework for optimizing third-harmonic diffraction efficiency. These results establish pulse-engineered metasurfaces as a powerful platform for nonlinear wavefront shaping and frequency conversion applications, while simultaneously serving as a warning that pulse properties play a vital role in metasurface function design.

3.1 Introduction

Over the past decade, nonlinear optical metasurfaces have emerged as an effective means to study fundamental light-matter interactions [111] and are pursued for a range of applications [96], such as efficient generation of structured beams of harmonic light [110, 125, 128], tunable functionality [182, 183] and analog signal processing with nonlinear films [184]. The ability to design nanoscale meta-atoms with tailored resonance wavelengths, quality factors, and polarization properties, has stimulated significant progress in optimizing nonlinear functionality. Resonant effects, in particular, are known to enhance conversion efficiencies by amplifying local near-fields [97]. Among these, quasi-bound states in the continuum (quasi-BIC) resonances have demonstrated exceptional performance for nonlinear frequency conversion, employing Fano lineshapes that significantly boost third-harmonic and high harmonic generation (THG and HHG) by many orders of magnitude[99, 165, 185]. These quasi-BIC resonances can occur when a dark mode (bound state) is coupled to a bright mode (acting as a continuum contribution) to give a Fano resonance in linear response [186]. Nonlinear metasurfaces not only boost conversion efficiencies in solid state systems by 3 to 5 orders of magnitude compared to that in unpatterned films, but also one can imprint nontrivial wavefronts, encoded in the arrangement and shape of the meta-atoms. This can find applications in areas such as nonlinear holograms [103], beam-shaping [125] to obtain beams with orbital angular momentum and nontrivial vector properties, beam steering [102, 182, 187, 188], imaging [108], and dynamic image tuning [110], demonstrating their versatility in both fundamental science and technological applications.

Most of the work in this domain has focused on enhancing nonlinear conversion efficiencies and shaping the desired beam properties [189] by leveraging meta-atom design, while usually not considering in detail the role of the input pulse shape. It is well understood that conversion efficiencies are highest when input pulse bandwidths match the quality factors of quasi-BIC resonances, while not much research has been attributed to understand how to shape nonlinear output as function of other driving pulse properties. For high driving powers, it is reported by multiple groups that metasurfaces for nonlinear conversion suffer from saturation effects [165, 188, 190]. Such saturation effects can occur due to self action (e.g., refractive index tuning and absorption induced by the frequency converted light), and lead to a limiting of conversion as well as a power-dependence of the generated third-harmonic (TH) and high-harmonic (HH) spectra. While it has been reported that such nonlinear effects could be useful for *manipulating* the harmonic generation process [190], in the majority of studies the critical role that driving pulse parameters play in shaping nonlinear optical emission is either overlooked or seen as a limiting factor, and certainly not seen as a resource.

In this Chapter we report on an experimental study of nonlinear emission from Fano resonant metasurfaces as a function of driving pulse properties, and we show that nonlinear diffraction patterns and spectra crucially depend on multi-mode interference. For a given, fixed, metasurface this means that very different TH conversion spectra and diffraction patterns can be obtained simply by choosing different input pulses. Our experiments are supported by a time-domain coupled oscillator model to provide insight into the key ingredients required to understand the vital influence of pulse properties on the behavior of diffractive nonlinear metasurfaces. Our findings highlight a pathway to more precise control over nonlinear emission by adjusting the characteristics of the excitation pulse, rather than modifying the metasurface structure itself. This approach not only holds promise for fundamental research, such as exploring spectral-temporal studies of nonlinear diffraction, but also expands the potential for practical applications in tunable photonic devices, enabling nontrivial control over nonlinear emission profiles [191, 192].

3.2 Fano resonant nonlinear metasurface

Figure 3.1 shows the main concept of our experiment. We excite a Fano resonant nonlinear metasurface with infrared pulses and study the generated TH diffraction patterns and spectra depending on how the excitation pulse matches the Fano-resonance. To this end, we vary the metasurface geometry to control the Fano line width and resonant wavelength, we vary the laser tuning (1320 to 1480 nm range) to control the detuning between excitation and metasurface resonance, and we perform measurements as a function of pulse power.

3.2.1 Fabrication and characterization

The dielectric metasurface (scanning electron micrograph shown in Fig. 3.2a) is fabricated in polycrystalline silicon (thickness 75 nm) evaporated on fused quartz, patterned with electron beam lithograpy and subsequent reactive ion etching. Appendix A reports in detail on the nanofabrication procedure. The sample consists of a square grid (880 nm pitch) of nominally identical unit cells that consist of a silicon disk of radius r_d= 295 nm with an off-centered hole with radius r_h= 125 nm. When the hole is placed at the meta-atom center, the system supports a symmetry-protected BIC mode, which is unaddressable under normal incidence. This resonance is opened to coupling to far-field radiation by introducing asymmetry through off-center placement of the hole [67, 110, 169]. The dimensionless asymmetry parameter α is defined as $\alpha = d/r_d$, where d is the distance of the hole from the center of the disk. The quasi-BIC mode manifests as a strong Fano resonance in transmission, resulting from the coupling between a bright in-plane electric dipole (ED)

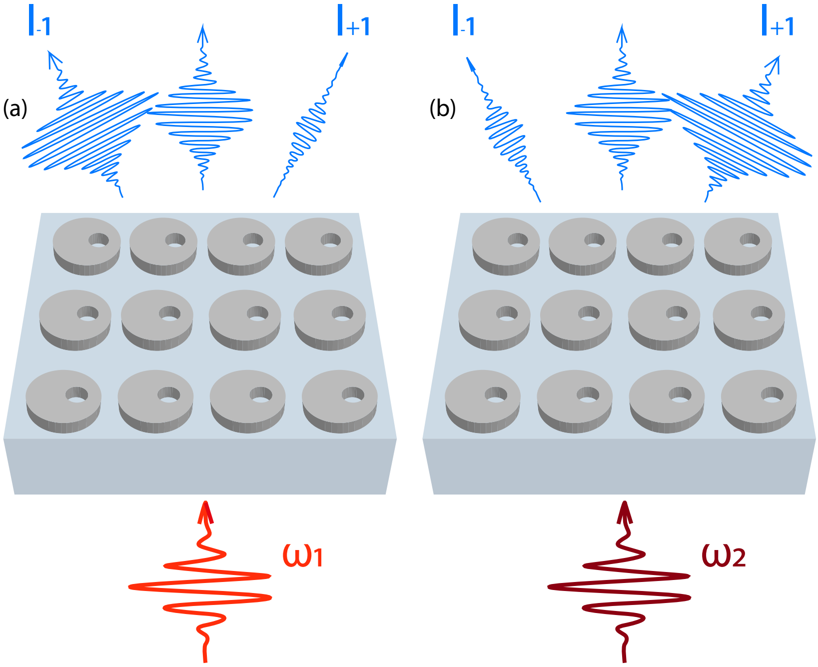

Figure 3.1: Schematic of our approach to study the nonlinear response as a function of driving pulse power and frequency. An infrared driving pulse excites a Fano resonance supported by a quasi-BIC dielectric metasurface. Depending on the pulse properties, such as power and frequency, a strong contrast emerges between opposing TH diffraction orders. This effect is illustrated in a) and b), where different driving frequencies result in varying diffraction order intensities.

and a dark out-of-plane magnetic dipole (MD) [164]. Figure 3.2b) presents a measured transmission spectrum for a metasurface with $\alpha = 0.3$ (green curve). The typical Fano lineshape at circa 1415 nm wavelength has a quality factor of ca. $Q = 289$, as extracted from fitting a coupled oscillator model (dark green dashed curve. See Appendix B for a detailed description of the coupled oscillator model). Figures 3.2c) and d) show simulations (c) and experimental results (d) of the spectral response as a function of α, which increases from bottom to top on the vertical axis. The simulation evidences a strong redshift with increasing asymmetry, as well as a strong dependence of the quality factor of the quasi-BIC, which decreases with increasing asymmetry as expected. Experimental transmission spectra as function of asymmetry agree closely to the simulation, aside from a minor overall shift in the wavelength axis, which we ascribe to a refractive index mismatch between the simulated silicon ($n = 3.45$) and the evaporated poly-Si, and minor differences in geometry dimensions, such as hole radius.

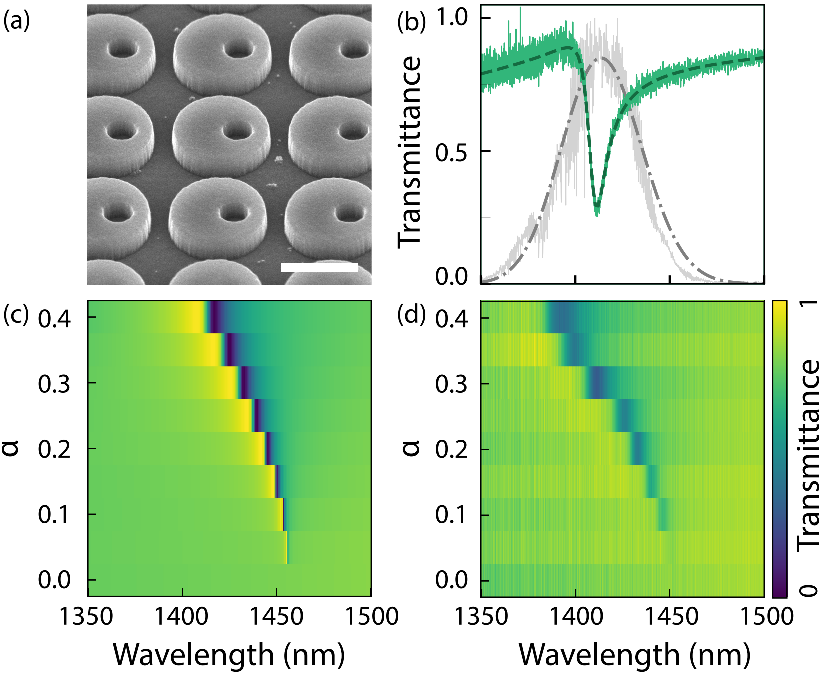

Figure 3.2: Metasurface properties: (a) Scanning electron micrograph of the silicon disk metasurface featuring an asymmetrically placed hole (scale bar 500 nm), pitch $p = 880$ nm, disk radius $r_d = 295$ nm, hole radius $r_h = 50$, Si height $d = 75$ nm.) The center of the hole is positioned at a distance $l = \alpha r_d$ from the center of the disk, where the asymmetry parameter α ranges from 0 (center) to 1 (edge), with this metasurface having $\alpha = 0.3$ (b) Linear transmittance of the metasurface (green solid line) with a coupled oscillator fit (dark green dashed), revealing a Fano lineshape of quality factor Q = 289. For reference, a 130 fs chirped pulse (chirp rate $\beta = -5 \cdot 10^{-6}$rad/fs^2), centered at 1414 nm, used for third-harmonic generation (experimental gray solid, modeled Gaussian pulse with similar parameters in dark gray dash-dot) is also shown. (c) COMSOL simulation of transmittance for a metasurface with similar properties, varying asymmetry parameters $\alpha = 0$ to $\alpha = 0.4$. The Fano resonance blueshifts and broadens, as the electric near-field concentrates in the hole for larger α, thus the field experiences a lower refractive index and stronger coupling from the bound state to the continuum. (d) Experimental transmittance of the fabricated metasurfaces with α ranging from 0 to 0.4, demonstrating strong agreement with simulations.

3.3 Experimental results

The metasurfaces are studied in a femtosecond Fourier microscope (schematic setup in Fig. 3.3a), more detailed setup in Appendix C). A train of 100 fs pulses at 1 MHz repetition rate and 1030 nm wavelength from a LightConversion Pharos laser is fed (input power 8 W) into a LightConversion Orpheus-F hybrid optical parameteric amplifier which as idler generates 130 fs pulses in the wavelength region of interest for our experiments (1300-1500 nm), of which a typical pulse spectrum is shown in Fig. 3.2b) (shaded gray). A combination of a half wave plate and a linear polarizer (Thorlabs AQWP10M-1600, LPVIS050-MP2) at the output of the laser controls the driving power, after which the pulse train is loosely focused onto the metasurface using a $f = 30$ mm lens, creating a spot with radius 11 μm on the sample. In the transmitted direction we employ a $100\times$ microscope objective (Nikon AC API plan, numerical aperture (NA) of 0.9) to collect transmitted infrared light as well as nonlinear emission. A dichroic mirror (Edmund Optics 69-900) reflects the third-harmonic light while transmitting the infrared beam for analysis on an optical spectrum analyzer (OSA), for determining pulse central wavelength. To fully suppress the infrared beam in the third-harmonic detection path we additionally use two short-pass filters (Thorlabs TF1). The third-harmonic emission is either fed into a grating spectrometer (Andor Shamrock 163i, 163 mm focal length, with a 300 lines/mm grating (SR1-GRT-0300-0500) and a 25 μm fixed-width vertical slit to which we mounted a monochrome CMOS camera (Ximea MC124MG-SY-UB) to resolve the third-harmonic spectrum or alternatively is directed onto a camera (Teledyne Prime BSI Express) to produce real- and Fourier-space images (selected by a flippable mirror, projecting the object plane or back focal plane on the camera chip). When pumped at full power (6 mW at 1 MHz repetition rate), bright TH is clearly visible, and a photograph of the TH on a piece of paper near the back focal plane (BFP) of the objective (Fig. 3.3a), right, taken with a phone camera), underlines both the strong THG conversion efficiency and the fact that the THG light is distributed over a set of diffraction orders. Here it should be noted that the metasurface does not support diffraction orders for the infrared excitation light. It it the induced polarization current at 3ω that can radiate into a set of diffraction orders owing to the fact that the metasurface periodicity exceeds the third-harmonic wavelength. The typical conversion efficiency enhancements, compared to the conversion efficiency of unpatterned silicon film on the same sample, are $\eta_{\text{enh}} = 10^3$ (measured at pump power 0.73 mW = 0.19 mJ/cm^2 $\simeq 1.37\text{GW/cm}^2$). Absolute conversion efficiencies (fundamental to harmonic power) are typically $\eta \sim 10^{-6} - 10^{-5}$.

Third-harmonic spectra for different tunings of the pump pulse and at constant pump power are presented in Fig. 3.3b) (pulse power = 0.5 mW, corresponding to pump fluence 0.15 mJ/cm^2) with different plot colors representing pulse central wavelengths as indicated in the caption, for a metasur-

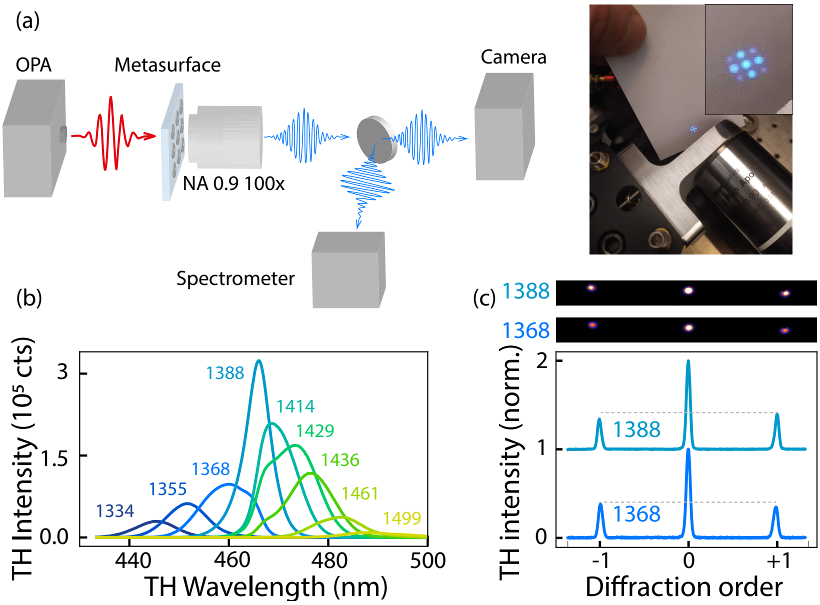

Figure 3.3: Third-harmonic generation experiment for studying TH spectra and TH diffraction contrast: (a) Sketch of the experimental setup to study TH spectra and diffraction contrast. An optical parametric amplifier (OPA) generates ca. 130 fs pulses centered between 1300 and 1500 nm, which are loosely focused (f = 30 mm) to excite the metasurface from the backside. A collection objective (NA 0.9, 100×) captures the TH light, projecting its back focal plane (BFP) via a $4f$-telescope onto a camera. Alternatively, a flip mirror directs the TH beam into a spectrometer. The right image, captured by a phone camera just behind the BFP, shows a typical blue TH diffraction pattern. b) TH spectra as a function of pulse tuning, with each color representing an excitation pulse centered at the wavelength indicated above the spectrum, for metasurface with $\alpha = 0.3$. The average power is maintained at circa 0.7 mW, corresponding to pump fluence 0.15 mJ/cm^2. c) Summed counts of the -1, 0, and +1 TH diffraction orders for pulses centered at 1368 nm (bottom dark blue) and 1388 nm (top light blue), showing pulse tuning can inverse diffraction order intensities. Pulse input power is 3 mW (0.79 mJ/cm^2).

face with asymmetry parameter $\alpha = 0.3$. Two key observations emerge. First, THG conversion is maximum when the pulse is tuned to spectrally match the Fano resonance. Secondly, the THG conversion spectra are not Gaussian, like the excitation pulse, but show marked shoulders. This is also observed by previous work reported in literature [110, 190]. The spectrum is narrowest and most like a single peak when the excitation matches the Fano resonance. For detuning in either direction, the converted pulses are broader, appearing to show a component that is pinned to the Fano resonance, and a component that tunes with the incident pulse. Figure 3.3c) shows cross cuts of 2D camera images, taken in Fourier imaging mode. The central peak represents the wavelength-integrated intensity of the zeroth diffraction order for the THG light, while the side peaks correspond to the ± 1st diffraction orders. These diffracted orders are diffracted along the direction of the structural asymmetry in the Fano-resonant meta-atoms (also for metasurface with $\alpha = 0.3$), which is orthogonal to the polarization direction of the driving field (input power of 3 mW, which corresponds to ca. 0.79 mJ/cm^2). The diffraction data has the following characteristics. First, the diffracted intensity is significant, with the intensity in the diffracted orders up to 50% of the intensity in the zeroth order. Second, the intensity of the $+1$st and -1st diffraction orders is different, indicated by the gray horizontal dashed line. This is a direct consequence of the structural asymmetry, and we have verified that the diffraction orders along the perpendicular axis do not show such an asymmetry. Finally, the bottom dark blue and top light blue line represent crosscuts at different central wavelengths of the pump pulse (1368 nm, resp. 1388 nm, relating the colors to the TH spectra in panel b), clearly demonstrating that the asymmetry in the TH diffraction that arises from the structural asymmetry, in fact depends on the pulse tuning. For this particular nanostructure the TH contrast $\Delta_I = \frac{I_{+1}-I_{-1}}{I_{+1}+I_{-1}}$ in the asymmetry ranges from zero (no significant different) to circa ± 0.3, depending on the pulse tuning and power.

3.4 Power dependent third-harmonic emission

A main conclusion drawn from the observations presented in Fig. 3.3, is that nonlinear TH generation depends in efficiency, spectral content, and diffracted output pattern, on the tuning of the input pulse relative to the metasurface Fano resonance. Less obvious is if these phenomena show a trivial third-power dependence on pump fluence, or whether there furthermore is a non-trivial power dependence to THG spectra and diffraction patterns. Figure 3.4 presents a power dependent study of TH spectra and TH diffraction contrast. In Fig. 3.4a) we show TH spectra generated for two selected input pulse wavelengths 1388 nm (blue curve, at Fano resonance) and 1436 nm (green, redshifted from Fano resonance), and at different input powers (lighter (darker) colors corresponding to lower (higher) input powers, ranging from 0.36 to 2 mW average power (corresponding to 0.09 mJ/cm^2 to 0.53 mJ/cm^2). To focus on the spectral shapes the spectra are normalised. Integrated intensity values are presented in panel (b). The spectra are clearly power dependent. For the reddest pump wavelength the shoulder at the Fano resonance observed in the tuning data (Fig. 3.3b) is clearly present. Notably its relative height compared to the main peak decreases with increasing input power (bright to dark green spectra in Fig. 3.4a). For the bluer pump wavelength, it is obvious that the spectrum broadens. We interpret both sets as indicative of one and the same physical scenario: the emission consists of a superposition of two contributions. Of these, one is pinned to the

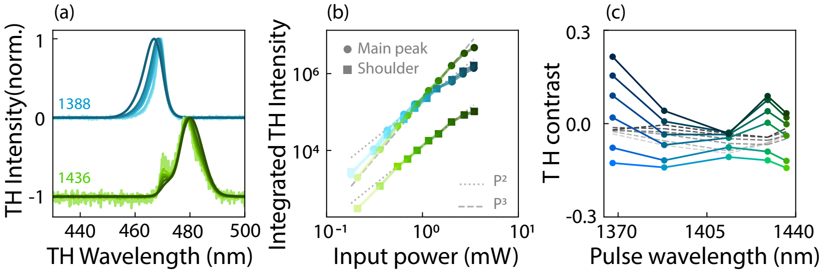

Figure 3.4: Power dependent study of TH spectra and TH diffraction contrast: (a) Normalized TH spectra for pulses centered at 1388 nm (blue) and 1436 nm (green), with increasing pump power indicated by lighter to darker shades (0.36 mW, 0.55 mW, 0.70 mW, 0.88 mW, 1.16 mW, 1.47 mW, 2.01 mW). (b) Log-log plot of TH power as a function of input pulse power, displaying the integrated TH intensity for the two Gaussians for each pulseone corresponding to the main peak and the other to the shoulderwith solid circles representing the main peak and the squares the shoulder, and increasing power as lighter to darker shades. A third-order (second-order) power law is shown as a gray dashed (dotted) line. (c) TH diffraction contrast Δ_I plotted as dots connected with solid lines, as function of pump pulse tuning and power, with light to dark colors representing increasing pump power (average pump power 0.7 mW to 5.2 mW in linear steps). The gray dashed line represents the TH diffraction contrast of the vertical orders, which fluctuates around 0, with a small deviation at lower input power that can be attributed to noise.

Fano resonant frequency, which quickly saturates with increasing power, and it arises from the quasi-BIC contribution. The other contribution likely arises from the broad dipole mode of the meta-atom. Since the broad dipole mode hardly shows a frequency structure in its linear response, the third-harmonic spectrum that arises from its nonlinear response is essentially the third-harmonic spectrum of the pump pulse as it would appear in a non-resonant medium. We hypothesize that this contribution does not saturate as quickly with incident pump power as the quasi-BIC contribution. On basis of this hypothesis we fit the spectra to sums of two Gaussians, extracting the power dependent growth of the integrated intensity of these two contributions. Example fits of the two fitted Gaussians are shown in Appendix D. The integrated TH intensity of the fitted Gaussians is plotted in Fig. 3.4b), in blue (green) for the 1388 (1436) nm pulses, where the circular markers represent the main peak and the squares the shoulder at the Fano frequency. Interestingly, the off-resonance 1436 nm pulse demonstrates a clear third-order power law for the main peak (green circles) across most of the pump fluence range, while the shoulder (green squares) grows according to a second-order power law, above 0.3 mW. From around 2 mW onwards the dependencies deviate from both the third- and second-order power laws, both showing a saturation behavior. Both on-resonant 1388 nm pulse Gaussian intensities show a 3rd order law for the lower input powers, and saturation sets in at input powers of 1 mW, or even somewhat below. Saturation of spectrally integrated conversion efficiencies has been commonly reported in the literature of nonlinear metasurfaces, and has been commonly attributed to self-action effects, such as free carrier induced detuning of the metasurface resonance [110, 190]. In Fig 3.3c) we plot TH diffraction contrast Δ_I as a function of pulse tuning, for six different input powers (0.7 to 5.2 mW, in steps of 0.9 mW, corresponding to lighter to darker colors). The TH contrast is also plotted in gray for the vertical orders, hovering around 0 at all tunings and input powers, showing that diffraction asymmetry only occurs along the geometrical axis along which the meta-atom symmetry is broken (slight deviations for lowest input powers can be attributed to the larger noise level). The diffraction contrast is generally minimal when the pump pulse is tuned to the Fano resonance, and reaches significant values upon detuning the pump from the Fano resonance. Moreover, the diffraction asymmetry generally depends on the pump power. In fact, at given pump tuning, the diffraction asymmetry even *inverts* upon increasing the pump power.

Given that the Fano-resonant response at the fundamental frequency is by construction the result of two modes interfering, it is intuitively to be expected that also the third-harmonic response can show multi-mode interference effects. In this view, tuning the pulse fundamental frequency will affect not just the overall TH generation efficiency, but also the interference balance between contributions of the two modes to the nonlinear diffraction pattern. Indeed, tuning causes different complex superpositions of the two involved modes at the fundamental frequency to be excited, and so even in a perturbative picture (3ω curves are just the third power of induced polarizations at frequency ω) this should change nonlinear diffraction properties. Less obvious is how this could result in a pump-power dependence of the diffraction patterns and spectra that is different from a simple overall third power scaling. We note that a better understanding of this physics is of high relevance for nonlinear metasurfaces. There have been many reports on record high spectrally integrated conversion efficiencies (highest values for pump pulses linewidth-matched to quasi-BICs), and successful demonstrations of, e.g., nonlinear holograms. The notion of a nonlinear hologram is associated to the notion that nonlinear diffraction patterns are *stable* against pumping conditions. Our work points at a marked spectral reshaping of nonlinear diffraction patterns in dependence of pump pulse tuning and pulse power. This could at the same time be limiting for applications (lack of control over nonlinear output), or be enabling as a means to nontrivially control nonlinear response.

3.5 Coupled oscillator model

We developed a semi-analytical model for TH responses in an effort to identify the minimum ingredients required to generate observations such as ours. The starting point is a coupled oscillator model for the frequency response of the system at the fundamental frequency.

3.5.1 Linear coupled oscillator dynamics

We set up a two-oscillator model with input-output ports, such that a low Q mode is directly driven by a Gaussian input pulse, while the high Q mode that generates the Fano resonance in transmission is only indirectly driven through coupling of the two oscillators. The low Q mode we identify as the 'bright' ED resonance, while the high Q mode represents the 'dark' MD mode. A detailed description of the nonlinear coupled oscillator model, including all relevant equations, is provided in Appendix B. While the model is easily solved in the spectral domain and can be accurately fitted to the experiments by adjusting the parameters (Q-factors, resonance frequencies, coupling strengths), for nonlinear calculations we proceed with the time-resolved modal excitation coefficients $a_1(t)$ for the ED and $a_2(t)$ for the MD mode of the form $a_{1,2}(t) = \tilde{a}_{1,2}(\omega)F(\omega)e^{i\omega t}$, where $\tilde{a}_{1,2}$ are the modal frequency-domain response functions and $F(\omega)$ represents the infrared laser pulse spectrum. The top section of Fig. 3.5a) presents a representative time trace of an off-resonant (1334 nm) driving pulse, along with the corresponding temporal ringdown of a_1 and a_2. At this wavelength, it is evident that the bright mode a_1 is directly excited by the input pulse, whereas the dark mode a_2 is only

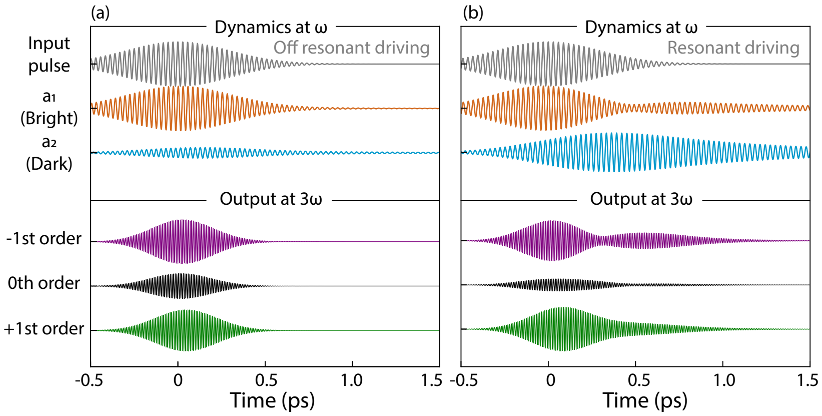

Figure 3.5: Coupled oscillator model dynamics: (a) In the top panel, the time evolution of the input pulse at off-resonant driving (1334 nm central wavelength) in gray and the ring-down of the two oscillators a_1 (orange) representing the bright ED and a_2 (blue) representing the dark MD. In the bottom panel, the time evolution of the conversion efficiency η at the third harmonic for the -1^{st} (purple) 0^{th} (black) and $+1^{st}$ (green) diffraction orders. (b) The temporal evolution for resonant driving with an input pulse centered at 1388 nm, the dynamics of a_1 and a_2 and at the bottom the conversion efficiency of the third-harmonic diffraction orders, indicated by the same colors as in (a).

weakly excited through coupling with a_1. Since the pulse bandwidths in our experiments are wider than the Fano resonance, both the bright and dark modes are excited. The dark mode, characterized by a high Q-factor, exhibits a long ringdown time, though its limited spectral overlap with the pump pulse reduces the excitation amplitude. Conversely, the broad ED resonance produces a ringdown signature only slightly longer than the incident pulse duration. The top section of Fig. 3.5b) shows time traces for a resonant pump (1414 nm) and the corresponding temporal ringdown of a_1 and a_2. In this case, for a few optical cycles, nearly all of the energy initially in a_1 transfers to a_2 leading to a strong excitation of a_2, which subsequently exhibits a large excitation amplitude and prolonged ringdown.

3.5.2 Nonlinear dynamics

To set up a simple description for the TH intensity in each nonlinear diffraction order we evaluate a perturbative model, in which we assume that THG generation in the time domain is produced by a current distribution that is proportional to the third power of the local and instantaneous current distribution that is induced at the fundamental. In the modal Ansatz that is the coupled oscillator model, the temporal and spatial dependences are by construction separated, meaning that the currents at the fundamental frequency are written as a product $\mathbf{j}_{1,2}(t,r) = a_{1,2}(t)\mathfrak{J}_{1,2,}(\mathbf{r})$, where the $\mathfrak{J}_{1,2}(\mathbf{r})$ are essentially the eigenmode spatial profiles. To obtain THG we expand the superposition $(\mathbf{j}_1(t,r) + (\mathbf{j}_2(t,r))^3$, as usual keeping only the terms that lead to third-harmonic contributions (i.e. a_2^3, $a_2^2 a_1$, $a_2 a_1^2$ and a_1^3, but not contributions with a subset of the factors complex conjugated, which correspond to four wave mixing). According to this logic the intensity spectrum of any of the diffraction orders $m = -1, 0, 1$, expressed as TH conversion efficiency η, is of the form

$$\eta_m(\tilde{\omega}) \propto \left| \int \left[A_m a_2(t)^3 + B_m a_2(t)^2 a_1(t) + C_m a_2(t) a_1(t)^2 + D_m a_1(t)^3 \right] e^{-i\tilde{\omega}t} dt \right|^2 \tag{3.1}$$

where the $\int \cdot e^{-i\tilde{\omega}t} dt$ arises to transform back to the spectral domain and where the coefficients $A_m, \ldots D_m$ derive from the spatial distribution of currents Fourier transformed over the unit cell to obtain far field diffraction efficiencies.

While a precise determination of the coefficients $A_m, \ldots D_m$ requires full-wave simulations, we argue that simple arguments inherent to the quasi-BIC nature of our structure already allow to draw important conclusions. First, we expect the term proportional to a_2^3 to dominate for Fano-resonant metasurfaces: conversion efficiencies are boosted typically 10 to 100 times by the Fano resonance as compared to having just the broad electric dipole mode (a_1 contribution) [97, 193]. This ratio depends on how well the incident pulse is linewidth matched to the Fano resonance at hand, with the highest values reported for picosecond pulses, while the lower value of 10 is pertinent to our experiment. This enhancement factor suggests a ratio $|a_2|/|a_1|$ of order 10, and therefore take D_m small. Furthermore, we argue that the mixing terms containing both a_2 and a_1 can not be ignored: if strictly only the dark high Q resonance would contribute to nonlinear diffraction, the relative intensity of diffraction orders would remain independent of the spectral content of the driving pulse. Instead, our key observation is that diffraction asymmetries depend on pulse tuning, implying that interference occurs of the different nonlinear contributions in Eq. 3.1.

3.5.3 Nonlinear diffraction

Next we examine spatial symmetries inherited from the original infrared modes by the nonlinear current distributions, and thereby the diffraction intensity of opposing diffraction orders. The bright mode (a_1 term) corresponds to an in-plane electric dipole (ED), which in linear optics in the far field gives rise to an even symmetry for the radiated field. Instead the dark mode corresponds to an out-of-plane magnetic dipole term, which in the far field gives rise to an odd-symmetry electric field. These symmetries carry over to the nonlinear terms, where terms that contain odd powers of a_2 result in odd-symmetry diffracted far fields, while terms with even powers of a_2 result in even-symmetry contributions. Thus each term in Eq. 3.1 taken individually would correspond to equal diffraction amplitudes at positive and negative diffraction angles, but taking the terms together will show either constructive or destructive interference in opposing diffraction orders. Based on these principles, the TH conversion efficiency in the +1 and -1 diffraction orders, $\eta_{\pm 1}$ must be related as

$$\eta_{\pm 1} \propto \left| \int \left[\pm A_1 a_2(t)^3 + B_1 a_2(t)^2 a_1(t) \pm C_1 a_2(t) a_1(t)^2 + D_1 a_1(t)^3 \right] e^{-i\omega t} dt \right|^2 \tag{3.2}$$

whereas for the 0^{th} order, because of the same symmetry reasons, there would be no contribution of odd powers of a_2, and the only terms left are a_1^3 and $a_2^2 a_1$

$$\eta_0 \propto \left| \int \left[B_0 a_2(t)^2 a_1(t) + D_0 a_1(t)^3 \right] e^{-i\omega t} dt \right|^2 \tag{3.3}$$

The bottom sections of Fig. 3.5 show the resulting timetraces for the ± 1 and zeroth diffraction orders, highlighting the integrand in Eq. 3.2. The free parameter choices (A, B, C and D) are discussed later in Section 3.5.4 and in Appendix B.5. The ringdown traces (Fig. 3.5) show beating patterns that are different in each diffraction order. This difference translates into different diffraction efficiencies for the two opposing diffraction orders.

3.5.4 Power dependent nonlinear emission

While this perturbed coupled oscillator model brings out most of the salient physics, namely the possibility of spectral/temporal shaping of THG in each order, and bringing out the possible asymmetry in diffraction efficiency at opposing angles, it fundamentally can not account for any non-trivial power dependence. By construction, all mode amplitudes in this model scale with the input field, and thereby all terms have a common scaling with the input power. This leads to a model in which the overall conversion efficiency will follow a third-power law, but the way in which spectra reshape or diffraction efficiencies distribute asymmetrically is independent of power. To impart a power dependence on the model we take inspiration from the measurement in Fig. 3.4b) in which the conversion efficiency is observed to saturate at high intensities, and to do so particularly at lower intensity for the narrow resonance. This can be understood from the fact that if saturation arises from strong field effects, the large field enhancement at a narrow resonance will cause it to occur already at a lower incident power. We therefore insert a power-dependent saturation function $F_n(P)$, replacing each occurrence of $a_n(t)$ by $F_n(P)a_n(t)$, with P the input power. Inspired by the measurement in Fig. 3.4b), which reveals a second-order power law dependence for the shoulder, we impose that

$$(F_n)^2 = \frac{F^2}{1+(F^2/(F_0^2/Q_n))^{1/3}} \tag{3.4}$$

with F the power dependent variable that follows $F=\sqrt{P}$, Q_n the quality factor Q for oscillator n, and F_0^2 the saturation cross-over power. Effectively, this

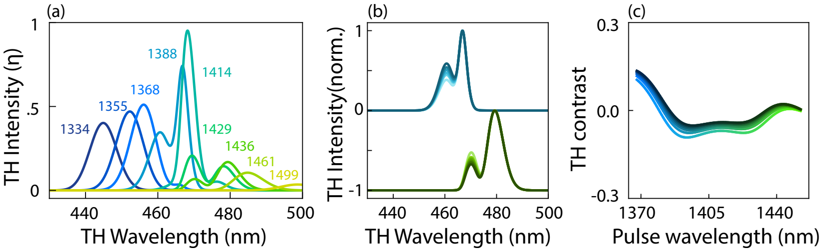

Figure 3.6: Modelled third-harmonic spectra and diffraction contrast as function of input power. (a) Modelled TH spectra as a function of pulse tuning, with each color representing an excitation pulse centered at the wavelength indicated above the spectrum, closely resembling the experimental results from Fig. 3.3b). The TH spectra are obtained from the Fourier transform of the combined ring-down in all diffraction orders. (b) Calculated power dependent TH spectra for input pulses centered at 1388 nm (blue) and 1436 nm (green), where increasing power (lighter to darker shades) is modeled by increasing F in the power dependent saturation function $F_n(P)$, where $F=\sqrt{P}$, with $P = 0.36$ mW, 0.55 mW, 0.70 mW, 0.88 mW, 1.16 mW, 1.47 mW, 2.01 mW. (c) Calculated TH diffraction contrast as a function of pulse central wavelength, plotted for six values of $F=\sqrt{P}$, for P increasing linearly from 0.7 mW to 5.2 mW

power dependent function tends to grow as P for low power or low F, and as $P^{2/3}$ for high power or high F, as to compute the TH output, the amplitudes enter as $(|a_n|^2)^3$. The cross-over power for each oscillator n is determined by F_0^2 corrected by Q_n, meaning that the high quality factor mode a_2 is already entering the quadratic regime at a $\frac{Q_2}{Q_1}$-times lower pump intensity than a_1. The cross-over value is defined as $F_0^2 = 20$ mW, which is analogous to the cross-over powers of 3.4b), where the main peak grows cubic until 2 mW (and $Q_1 \sim 10$), whereas the shoulder shows deviating behavior at the lower end of the input power ($P \sim 0.1$ mW, $Q_2 \sim 300$), With this empirical assumption, we attempt to replicate the data by fitting the free constants A, B, C and D, while the oscillator parameters (including F_0 and input power P) are taken from measured data.

Figure 3.6a) presents calculated TH spectra using this model, obtained by Fourier transforming the ring down traces for each order and summing the resulting spectral intensities over all diffraction orders (± 1 and 0). The colors in the figure correspond to different pulse central wavelengths, similar to Fig. 3.3b). The oscillator parameters for a_1 and a_2 were extracted by fitting experimentally measured linear transmission spectra (as shown in Fig. 3.2b)), while the incident pulse parameters are obtained from Gaussian fits to the measured excitation pulse. All other model parameters values are given in Tab. 3.1 in Appendix B.5. Comparing the calculated TH spectra of Fig. 3.6a) to the measured TH spectra of 3.3b), two key similarities stand out: i) the presence of a shoulder near the Fano resonance and ii) the fact that highest TH conversion efficiency occurs when the pulse is tuned at the resonance. Calculated power dependent spectra for two incident pulse tunings are shown in Fig. 3.6b), describing the experiment in Fig. 3.4a), for F ranging from $\sqrt{0.36}$ to $\sqrt{2.01}$, as are the input powers in the experiment, for light to darker colors. The calculated spectra closely mirror the experimental observations, where the shoulder diminishes at higher input powers, and the TH peak shifts away from the Fano resonance. The calculated TH contrast as a function of driving pulse tuning is plotted for six input powers with curves shaded from bright to dark, corresponding to increasing input powers (0.7 to 5.2 mW, $F = \sqrt{0.7}$ to $\sqrt{5.2}$) in Fig. 3.6c). Although the power dependence is much less pronounced in the calculation, the experimental behavior is qualitatively well reproduced, allowing us to identify the minimal contributors to the observed effects: (1) Spectral reshaping occurs because THG arises not solely from the narrow resonance but also from its interference with THG from the broad resonance; (2) The different symmetries of the two modes lead to nonlinear interference, resulting in an asymmetric diffraction pattern; and (3) Saturation of THG generation efficiency with increasing local field introduces a power dependence in both spectral reshaping and diffraction that reduces the cubic law to quadratic for higher input powers, where specifically the dark mode a_2 cross-over happens at $\frac{Q_2}{Q_1}$-times lower pump intensity than for the bright mode a_1. The model outlined above is based on simple principles, with the goal to demonstrate the minimum physical ingredients that capture the key mechanisms shaping TH spectra and diffraction across different input pulses, providing an initial understanding of the underlying physics. One might be tempted to view the model as a fitteable description of the data, with the possibly complex-valued coefficients A, B, C and D as free fit parameters. While we strongly caution against overinterpreting multiparameter fits to data of such simplified models, we argue that one can indeed adjust the parameters to obtain a consistent parametrization of our data set, from which one could perhaps extrapolate to other driving conditions or metasurface asymmetries. An exploration of calculated TH spectra and power dependent contrasts, for different parameter choices A, B, C and D, and pulse chirp and duration, are found in Appendix B.5.

To further investigate the power dependence of TH diffraction patterns, we fabricated and analyzed a series of metasurfaces with varying asymmetry parameters α ranging from 0 to 0.4. We refer back to Fig. 3.2 for the simulated and experimental linear response of these metasurfaces as gauged by transmission spectra. Figures 3.7a-c) summarize measurements of the TH diffraction contrast, quantified as the intensity ratio between the $+1^{st}$ and -1^{st} diffraction orders, presented as a function of pulse tuning on the horizontal

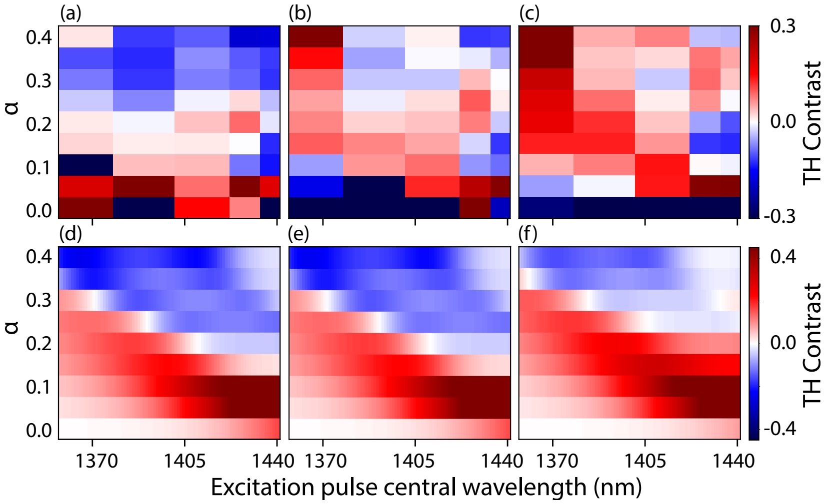

Figure 3.7: TH diffraction contrast across all fabricated asymmetry parameters as a function of five pulse tunings, with color representing the TH contrast favoring the -1 (blue) and +1 (red) orders. The experimental results are shown in (a-c), where we vary the average pulse power as (a) 1.4 mW, (b) 3.3 mW and (c) 5.2 mW (0.37, 0.87, 1.37 mJ/cm^2 resp.). (d-f) Calculated TH contrast for oscillators parameters extracted from the experiment, at similar pulse tuning range for $F = \sqrt{1.4}$ (d), $\sqrt{3.3}$ (e) and $\sqrt{5.2}$ (f), showing similar behavior as the experiment.

axis and asymmetry parameter on the vertical axis. Panels (a), (b), and (c) correspond to different average input powers: 1.4 mW, 3.3 mW, and 5.2 mW (0.37, 0.87, and 1.37 mJ/cm^2), respectively. The color scale spans a TH contrast from -0.3 (blue) to 0.3 (red), indicating a maximum contrast of 30%. Generally, the TH contrast is negative, following the tuning of the Fano resonance with meta-atom asymmetry, and turns positive at wavelengths on either side of the resonance, being more positive for shorter (bluer) pump wavelengths. For small asymmetry values—where the Fano resonance has the highest Q-factor and the weakest spectral overlap with the input pulse—the contrast is predominantly positive. However, we must note that at $\alpha \leq 0.1$, the overall TH intensity is very low, leading to larger measurement uncertainties. A notable trend is that increasing the pump-power shifts the overall contrast toward positive values, especially for longer (redder) wavelengths, while specific contrast depends strongly on pulse tuning. We evaluated the model employing the identical fitted constants (A, B, C and D) as in Fig. 3.5, while using oscillator parameters derived from fitting to the linear transmission data shown in Fig. 3.2d), to calculate power-dependent TH contrast across the same range of excitation pulse tunings as the measurement. The results of the model, presented in Figs. 3.7d-f), demonstrate a clear transition of the TH contrast from positive to negative as the excitation pulse tunes through the resonance. The inflection point of this transition follows the tuning of the Fano resonance with meta-atom asymmetry. Additionally, the increase in the power-dependence results in an overall positive shift in the contrast around the Fano resonance, as well as on both sides of it. This behavior is consistent between the experiment and the model, albeit less pronounced with changes in increased driving power. The reduced strength of the calculated power dependence may arise from an inaccurate estimation of the power cross-over point used to determine F_0 or from a modest choice of the power dependence of Eq. 3.4. Furthermore, although the spectral resolution of the experiment is quite limited compared to the calculations, the measurements still clearly capture the essential qualitative features. In particular, they demonstrate the tunable diffraction contrast through the Fano resonance and its characteristic power dependence, which our model aims to explain. Both the experimental and modeled results reveal that, for specific pulse wavelengths and powers, the TH contrast undergoes a complete reversal. This reversal happens either across two distinct powers at a given wavelength or across two wavelengths at a fixed power. These results highlights the tunable nature of the nonlinear diffraction pattern, which can be precisely controlled by adjusting the driving pulse properties. The observed behavior underlines the crucial role of the interference between the dark and bright modes in shaping the dynamic, wavelength-dependent diffraction contrast, further reinforcing the models ability to capture these complex dynamics.

3.5.5 Phase relation of the coupled nonlinear oscillators

The crucial physics that explains the non-Gaussian shape of the TH spectra and the frequency-dependent TH contrast reversal for the diffraction orders is, according to our model, the interference of the dark and bright mode contributions in the nonlinear far-field diffraction orders. An essential ingredient in this explanation is the phase relation between the bright mode a_1 and the dark mode a_2 mode, where the Fano resonance term a_2 picks up a π phase shift when tuning through resonance. This transduces to a phase shift as function of tuning for the nonlinear diffraction orders, which in turn contributes to the pump-wavelength dependence of the diffraction asymmetry. This rather indirect chain of reasoning has a signature that is directly accessible in experiment. The phase shift is accessible in our experimental set-up by performing wavelength-dispersed real space imaging, wherein the 0^{th}, $+1^{st}$ and -1^{st} orders are all recombined to produce interference. We project a slice of the real space TH signal on the entrance slit of our grating spectrometer, with the asymmetry in the meta-atom aligned along the axis of slit, and the incoming light polarized perpendicular to it. Figure 3.8a) presents dispersed real-space images for the same two pulses as in Fig. 3.4a) (1388 and 1436 nm central wavelength, top and bottom panels resp.) at a pulse power of 0.7 mW. It is important to note that the asymmetry of the meta-atom, and thus the slit and the imbalanced $\pm 1^{st}$ orders are oriented along the vertical y direction of the plots, while the x-axis corresponds to TH wavelength. Colors are plotted in a log-scale to emphasize the low-intensity parts of the image. We indeed observe fringes in the spatial domain because of the interference of the 0^{th}, $+1^{st}$ and -1^{st} orders. Summing intensity along the spatial coordinate should give the TH spectra: indeed the two-component nature of the spectra (shoulders in Fig. 3.4a) are evident, particularly in the bottom panel. The TH Fano resonance spans 468 nm to 473 nm. The periodicity of the fringes along the spatial dimensions equals the metasurface pitch.

In these experimental images the key observations that relates to the phase response of the Fano resonant contribution is a sudden spatial shift of the fringes by half a period which is visible at /near the 468 - 473 nm wavelength range. This observation is direct evidence of the fact that the Fano-resonant terms pick up a phase slip ($n\pi$ for terms containing a_2^n). With the 0^{th} order light acting as phase reference, this expresses as a shift in the fringes. Dispersed real-space calculations are presented in Appendix B.6, which reveal similar interference fringes as Fig. 3.8a), including the phase slip at the TH of the Fano.

3.6 Conclusion and outlook

In summary, we presented observations of TH diffraction and spectra from Fano-resonant metasurfaces, and showed that TH diffraction imbalances and

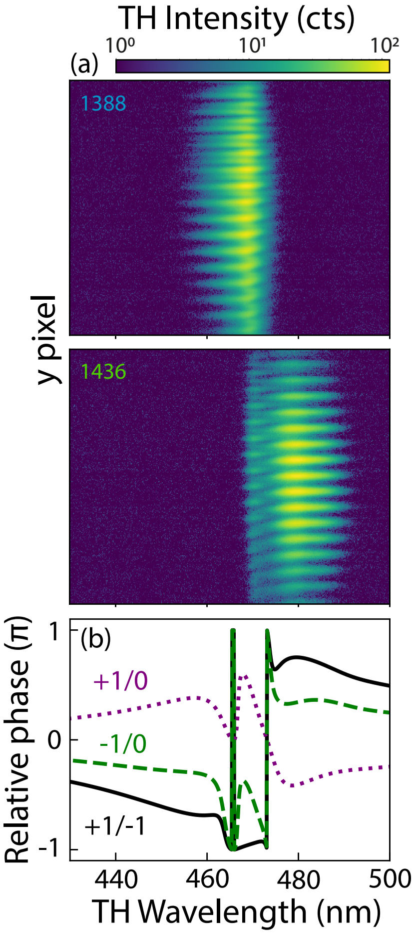

Figure 3.8: Motivation for phase relation of the coupled oscillators: (a) Dispersed real-space images for a metasurface with asymmetry parameter $\alpha = 0.3$ and pulse central wavelength = 1388 nm (1436 nm) on the top (bottom), showing clear phase jumps at the Fano resonance. TH intensity (counts) is plotted on a log-scale to highlight the visualization at low intensity. (b) Calculated relative phase between the $\pm 1^{st}$ and 0^{th} orders showing a strong phase relation around the Fano resonance third-harmonic wavelengths, evidencing the influence of the phase relations of the diffracted orders to the TH spectra.

non-Gaussian TH spectra occur that are strongly dependent on pump pulse power and frequency tuning. These experimental observations were explored through a coupled oscillator model, which successfully replicated the phenomena. The observed TH diffraction imbalance is attributed to the constructive and destructive interference of nonlinear, mixed, contributions from the two coupled oscillators in this model, and we argued how their radiation pattern properties result in asymmetries in TH conversion efficiency in opposing diffraction orders. This interpretation revolves around the idea that input pulse properties control the ring down dynamics of the bright and dark modes responsible for the quasi-BIC Fano resonance characteristics, which in turn results by nonlinear conversion in multi-modal interferences at the third-harmonic frequency. This view is supported by the fact that the signature π-phase slip in the resonant response of the dark mode is directly visible in the experimental data through real-space spectral measurements in which the diffraction orders interfere. Furthermore, we note that the observations point to the importance of saturation with increasing pump power of the TH efficiency. Indeed, power-dependent measurements revealed that the shoulder at the third harmonic of the Fano resonance reduces to a second-order power law, contrasting with the expected third-order behavior at much lower pump-powers than the contribution of the bright mode. The calculated predictions align well with experimental observations, meaning that key features, 1) the asymmetric diffraction efficiencies, 2) the deviation from a purely third-order power law and 3) non-Gaussian shaped TH spectra, can be explained in terms of a relatively simple coupled oscillator model.

An interesting question is how our findings translate to other quasi-BIC metasurfaces that support similar or other types of modes. By their very nature, quasi-BIC resonances exhibit an optical response that combines a broad continuum with a narrow resonance, creating a multi-mode platform that naturally enables spectral reshaping, nonlinear multi-mode interference, and intricate tuning dependencies. In addition, the metasurface period typically permits diffraction channels at the harmonic wavelength. While this is not a defining property of quasi-BIC metasurfaces, this condition is satisfied in most reported works on quasi-BICs. Another important characteristic is the difference in modal symmetry between the continuum and the narrow resonance, which drives diffraction asymmetries as a direct consequence of nonlinear multi-mode interference in the far-field. In this work, we focused on a system supporting a bright and a dark mode with symmetric and antisymmetric far-field emission, respectively. More generally, the rich landscape of quasi-BIC metasurfaces includes a wide variety of mode configurations, involving both in-plane and out-of-plane field components. Many of these systems exhibit modal interference effects [110, 163, 164] and are inherently subject to imbalanced diffraction physics, similar to our experimental observations and captured by our model. The symmetry-breaking route is currently the most used approach to achieve high-Q quasi-BIC metasurface resonances, and our findings generically apply to this class of metasurfaces. These symmetry-broken quasi-BICs can also host fundamentally different types of mode interactions and field distributions [62, 165, 185, 190]. In such cases, multi-mode interference in the nonlinear diffraction orders is still expected, though its expression will differ quantitatively.

An interesting avenue for future research is to incorporate the emission profiles of the modes at the harmonic wavelengths. In the present work, we focused on the emission profiles of the fundamental modes which, when raised to the harmonic order, interfere in the far-field diffracted orders. The fundamental modes consist of an in-plane electric dipole and out-of-plane magnetic dipole, that both yield a typical donut-like emission pattern, characterized by a node along the dipole axis. In the nonlinear diffracted orders, this leads to the even and odd symmetry argument for the electric far-field. Obtaining the harmonic profiles of a single meta-atom would require full-wave simulations to extract the near-field current distribution. However, a full angular dependent emission pattern is not required, since intensity is guaranteed to only appear in the diffraction orders due to the periodicity. Nonetheless, the inclusion of the emission profile of harmonic modes could provide a more complete picture of nonlinear diffraction, which provides more insight and furthermore expands the opportunities for nonlinear beam shaping and steering.

Our findings highlight the importance of driving pulse properties in the design of applications for nonlinear metasurfaces. This insight is highly relevant in the context of recent reports that focus on record-high spectrally integrated conversion efficiencies [98] and nonlinear holograms that promise to produce robust diffraction patterns under varying pumping conditions [194]. Our work reveals that nonlinear diffraction spectra can undergo significant reshaping depending on the input pulse parameters. This spectral transformation presents both challenges and opportunities: on the one hand, it may introduce unpredictability in nonlinear output; on the other, it enables nontrivial control over nonlinear emission profiles. Crucial aspects that are not addressed in this work are the roles of pulse bandwidth, chirp, or the potential of dedicated pulse shaping. These aspects likely provide additional degrees of control over nonlinear diffraction, further emphasizing the necessity and potential of accurately tailoring driving pulse parameters for practical applications. These aspects hold promise for both fundamental studies, such as exploring advanced pulse shaping techniques for time-resolved studies and spectral-temporal control of nonlinear diffraction, and strategies for practical applications in tunable photonic devices, such as efficient optical routing [182] or optical switching [195]. Furthermore, insights from our coupled oscillator model suggest specific design strategies for creating efficient diffraction routers, such as Q-matching and aligning oscillator contributions. These methods could facilitate the development of advanced photonic devices, broadening the scope of metasurface applications by utilizing the deeper understanding of driving pulse properties to achieve tailored nonlinear responses.

Appendices

A Nanofabrication procedure

We employ a standard electron beam lithography (e-beam lithography) recipe to fabricate the nanostructures. Fused quartz substrates (12 × 12 mm, 500 μm thick, Siegert Wafer GmbH) were first cleaned by sonication in deionized water for 10 minutes. This was followed by immersion in a base piranha solution at 75°C for 15 minutes, then rinsed thoroughly with water (2 dips of 15 seconds) and isopropanol (IPA). A 75 nm thick layer of polycrystalline silicon was deposited via e-beam evaporation (Polyteknik Flextura M508 E), using silicon pellets at an emission current of 90 mA, resulting in a deposition rate of 0.1 nm/s. To protect the silicon during later development steps and to improve adhesion to the resist, the samples were exposed to oxygen plasma for 2 minutes to grow a thin passivation layer. Next, a hydrogen silsesquioxane (HSQ) resist layer (Dow Corning XR-1541 E-Beam Resist) with an approximate thickness of 65 nm was spin-coated at 3000 rpm with an acceleration of 1000 rpm/s for 45 seconds, and baked at 180°C for 2 minutes. To suppress charging during e-beam exposure, a conductive Elektra layer (All Resist GmbH, Electra 92) was spin-coated on top at 2000 rpm, 1000 rpm/s, for 60 seconds and baked at 90°C for 2 minutes. Patterning was performed using a RAITH Voyager electron beam lithography system at 50 kV, with an average exposure dose of 1500 $\mu\mathrm{C/cm^2}$. Development began with a 15-second dip in water to remove the Elektra layer, followed by 70 seconds in TMAH at 60°C, and rinsing in water and IPA for 15 seconds each. Finally, the HSQ mask pattern was transferred into the silicon layer using reactive ion etching (Oxford Instruments, Plasma Technologies Plasmalab 80 Plus) with a $CHF_3/SF_6/O_2$ gas mixture (15/10/3 sccm), at a forward power of 150 W and a chamber pressure of 7 mTorr. The etch rate under these conditions was approximately 45 nm/min. Residual resist was not removed, as it was found to have negligible effect on the optical properties or experimental outcomes.

B Coupled oscillator model

Here, we report on the coupled oscillator model in fine detail.

B.1 Equations of motion

Suppose that you have a linear system of two coupled pendulums, leading to the following equations of motion

$$\begin{aligned} \ddot{a}_1 + \gamma_1 \dot{a}_1 + \omega_{0,1}^2 a_1 + \kappa a_2 &= \frac{F_1}{m} \\ \ddot{a}_2 + \gamma_2 \dot{a}_2 + \omega_{0,2}^2 a_2 - \kappa a_1 &= 0 \end{aligned} \tag{3.5}$$

where we will be assuming a_1 to be the broad oscillator (loss γ_1 of order $\omega_{0,1}/5$) of mass m that is directly driven by F_1, and where we assume a_2 to be the indirectly driven oscillator that couples to the driven oscillator, (with $\gamma_2<\gamma_1$) which gives the Fano resonance. $\omega_{(0,n)}$ is the resonance frequency of oscillator n, and κ is the coupling between the two oscillators. For monochromatic driving oscillating of the form $e^{i\omega t}$, we derive to response functions that we call *polarizabilities*. These response functions are sometimes referred to as susceptibilities in literature; however, we shall avoid this terminology to disambiguate from nonlinear material susceptibilities. The polarizabilities are described as

$$\begin{pmatrix} a_1(t) \\ a_2(t) \end{pmatrix} = \begin{pmatrix} \alpha_1(\omega) \\ \alpha_2(\omega) \end{pmatrix} \frac{F_1}{m} e^{i\omega t} \tag{3.6}$$

with

$$\begin{pmatrix} \alpha_1(\omega) \\ \alpha_2(\omega) \end{pmatrix} = \begin{pmatrix} \omega_{0,1}^2 - \omega^2 + i\omega\gamma_1 & \kappa \\ -\kappa^* & \omega_{0,2}^2 - \omega^2 + i\omega\gamma_2 \end{pmatrix}^{-1} \begin{pmatrix} 1 \\ 0 \end{pmatrix} \tag{3.7}$$

These describe the frequency response in a single "modal excitation coefficient" α_n per oscillator n, where we introduced f that tunes leakage for in-output-port calculations. Depending on the parameter choice, this will give rise to Fano resonances in the spectral response, for instance, we visualize the oscillator excitations $\alpha_{1,2}$ by plotting both their absolute values in Fig. 3.9, with α_1 increased 100-fold to enhance visibility. Furthermore, to calculate transmittance from $\alpha_{1,2}$, we start by defining $\mathbf{M}$ as the matrix on the RHS of equation 3.7, and adjust the driving of the first oscillator to include an input coupling rate that is consistent with the oscillator damping rate according to the requirements of coupled mode theory. One obtains a cavity response function of the form

$$\alpha(\omega) = 2i\omega\sqrt{\gamma_1} \cdot \left[\mathbf{M}^{-1}(\omega) \cdot \begin{pmatrix} 1 \\ 0 \end{pmatrix} \right] \tag{3.8}$$

which we can write out as

$$\alpha(\omega) = \frac{2i\omega\sqrt{\gamma_1}\left(i\gamma_2\omega - \omega^2 + \omega_2^2\right)}{\left(-\omega^2 + if\omega\gamma_1 + \omega_1^2\right)\left(i\gamma_2\omega - \omega^2 + \omega_2^2\right) - \kappa^2} \tag{3.9}$$

and the transmittance becomes

$$T(\omega) = |1 - \alpha(\omega)\sqrt{\gamma_1}|^2 \tag{3.10}$$

We fit this expression for the transmittance T to our experimental spectra to obtain the oscillator parameters (resonance frequencies, damping rates, coupling). Figure 3.9b) presents the fitted Fano lineshape to the experimental data, including spectra of the experimental and simulated driving pulses. Note that we could consider complex-valued couplings, which gives rise to the conjugate in equation 3.7. This complex coupling would result in electromagnetically induced absorption, as opposed to transparency. In our work we consider only real-valued coupling coefficients κ.

B.2 Gaussian pulse response

Let us move to discussing driving and response to pulsed excitation for the linear case, i.e. at the fundamental. We assume driving with a Gaussian pulse, such as in the experiment, instead of monochromatic light. The driving will take the form

$$\frac{F_1(t)}{m} = e^{-t^2/2\Delta t^2}\, e^{i\omega_{0p}t}/\sqrt{\Delta t} \tag{3.11}$$

for a carrier frequency ω_{0p} and a pulse width Δt, the Fourier transform gives the spectrum, which for the field associated to the Gaussian pulse reads

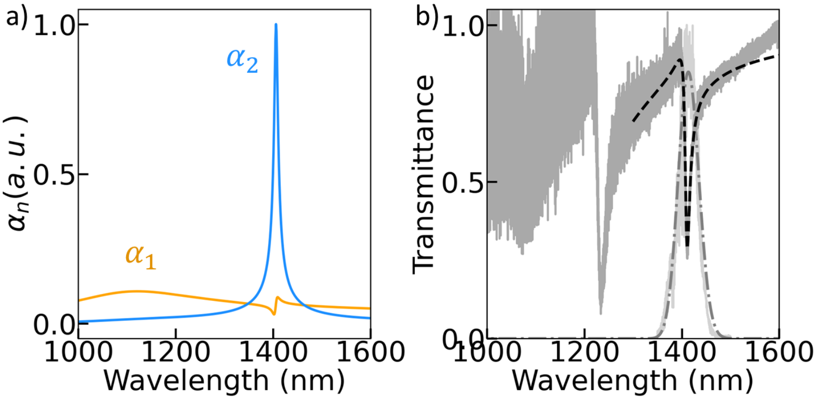

Figure 3.9: a) Modal excitation amplitudes α_1 (orange) and α_2 (blue) of the coupled oscillator model as a function of wavelength, showing the relative contribution of each mode to the overall response. b) Experimentally measured transmittance spectrum (gray) overlaid with the fitted Fano lineshape (black dashed), derived from the coupled oscillator susceptibility model, including experimental driving pulse on the background (lightgray) and modeled driving pulse (darkgray dash-dot). The broad oscillator α_1 is visible in the measured transmittance spectrum, even though with a low signal-to-noise ratio around 1100 nm, whereas the coupled narrow oscillator α_2 is visible near 1400 nm. A second Fano is visbile around 1250 nm, which could be attributed to a magnetic quadrupole or another higher order dark mode that couples to the same broad mode α_1

$$F_1(t)/m = \int E(\omega)\, e^{i\omega t}\, d\omega \tag{3.12}$$

with

$$E(\omega) = \frac{1}{2\pi} \int e^{-t^2/2\Delta t^2}\; e^{i\omega_{0p}t - i\omega t - i\beta t^2} / \sqrt{\Delta t}\, dt \tag{3.13}$$

which is visualized in the top row of Fig. 3.5. Here, we introduced linear chirp β, which might be zero, but can give rise to a linear variation of the instantaneous frequency for nonzero values. The spectrum evaluates to $|E(\omega)| \propto e^{-(\omega-\omega_0)^2\Delta t^2/2}$, stating that the spectrum is Gaussian, centered around ω_0, and has a frequency width of $1/\Delta t$. If we apply this type of driving to the coupled oscillators, we obtain the following transient responses

$$\begin{pmatrix} a_1(t) \\ a_2(t) \end{pmatrix} = \int \begin{pmatrix} \alpha_1(\omega) \\ \alpha_2(\omega) \end{pmatrix} E(\omega)\, e^{i\omega t}\, d\omega \tag{3.14}$$

This gives us the temporal response of the oscillators, commonly referred to as the ringdown. From the ringdown, we can identify four obvious facts: 1) To feed amplitude into the Fano resonance, we need sufficient κ. 2) The ringdown of the high Q resonance α_2 is long, which means that many more cycles contribute to any harmonic generation compared to the ringdown of the broad mode α_1. 3) Unless enough energy is fed into the Fano resonance, the broad mode has a briefer flash but potentially higher modal intensity coefficient. Lastly, 4) matching pulse width and tuning affects the fraction of energy that feeds into the Fano. See Fig. 3.5 for ringdown calculations.

B.3 Third-harmonic generation

The coefficients $\alpha_{1,2}$(t) are the time-dependent modal excitation coefficients that describe the temporal response, while the real-space behavior is contained in electromagnetic mode profiles, which for modes 1 or 2 are associated with electric field distributions $\mathbf{E}_1(\mathbf{r})$ and $\mathbf{E}_2(\mathbf{r})$. This Ansatz means that the instantaneous field distribution induced in the sample at the fundamental frequency reads as a sum of factorized terms

$$\mathbf{E}(\mathbf{r},t) = \mathbf{E}_1(\mathbf{r})\, a_1(t) + \mathbf{E}_2(\mathbf{r})\, a_2(t) \tag{3.15}$$

or in terms of the frequency domain polarizabilities

$$\mathbf{E}(\mathbf{r},t) = \int [\mathbf{E}_1(\mathbf{r})\, \alpha_1(\omega) + \mathbf{E}_2(\mathbf{r})\, \alpha_2(\omega)]\, E(\omega)\, e^{i\omega t}\, d\omega \tag{3.16}$$

Third-harmonic generation is understood to arise through a nonlinear material susceptibility, causing a local time-dependent nonlinear polarization to be induced everywhere where there is a nonzero nonlinear susceptibility $\chi^{(3)}$ (which we assume to be only in the Si meta-atoms)

$$\mathbf{P}_{\mathrm{TH}}(\mathbf{r},t) = \chi^{(3)}(\mathbf{r})\, [\mathbf{E}(\mathbf{r},t)]^3 \tag{3.17}$$

The induced nonlinear polarization can also be viewed as a nonlinear third-harmonic radiating current

$$\mathbf{j}_{\mathrm{TH}}(\mathbf{r},t) = \frac{\partial \mathbf{P}_{\mathrm{TH}}}{\partial t} \tag{3.18}$$

It should be noted that we focus solely on $\chi^{(3)}$ effects and that the $[.]^3$ does not involve an absolute value of the field. Indeed, one should work with the physical field, i.e., just the the real part of the complex-valued electric field in the nonlinear polarization expression. This introduces the full richness of all possible combinations of $e^{\pm i\omega t}$ that arise when expanding the cubic term. This encompasses sum and difference frequency generation, effectively capturing the entire four-wave mixing landscape. Since we are specifically interested in frequencies near the third harmonic, we narrow our focus and disregard the broader complexity of four-wave mixing, retaining only the +++ and — exponent terms that contribute directly to third-harmonic generation. This leads to a nonlinear current distribution of the form

$$\begin{aligned} \mathbf{j}_{\mathrm{TH}}(\mathbf{r},t) \propto \iiint\, & [\mathbf{F}_1(\mathbf{r})\alpha_1(\omega_1) + \mathbf{F}_2(\mathbf{r})\alpha_2(\omega_1)] \cdot [\mathbf{F}_1(\mathbf{r})\alpha_1(\omega_2) + \mathbf{F}_2(\mathbf{r})\alpha_2(\omega_2)] \cdot \\ & [\mathbf{F}_1(\mathbf{r})\alpha_1(\omega_3) + \mathbf{F}_2(\mathbf{r})\alpha_2(\omega_3)] \cdot \\ & E(\omega_1)E(\omega_2)E(\omega_3)\, e^{i(\omega_1+\omega_2+\omega_3)t}\, d\omega_1\, d\omega_2\, d\omega_3 \end{aligned} \tag{3.19}$$

where the spatial dependence of χ is absorbed into the mode profiles $\mathbf{E}_1$ and $\mathbf{E}_2$ to get $\mathbf{F}_1$ and $\mathbf{F}_2$ To proceed, we must introduce further assumptions. If a_1 represents the broad mode and a_2 the narrow mode, then the nonlinear contribution from the broad mode $\mathbf{F}_1$ is expected to be significantly smaller than the contribution from $\mathbf{F}_2$ to the nonlinear current, due to the much weaker normalized field amplitude that is associated with the broad mode. This statement is quantitatively motivated by the observation that in Fano resonant metasurfaces harmonic generation efficiencies remains very low, unless the mode coupling constant and the excitation pulse width and tuning are selected to precisely match the quasi-BIC mode.Under this assumption, it is reasonable to expand the product and order the terms such that the $(\mathbf{F}_2)^3$ contributions lead, while also retaining terms with a single factor $\mathbf{F}_1$, i.e., terms proportional to $(\mathbf{F}_2)^2\,\mathbf{F}_1$, while discarding order contributions with multiple instances of $\mathbf{F}_1$. While in the description of THG Fano-resonant metasurfaces the discussion usually focuses on just the $(\mathbf{F}_2)^3$ term, we note that at least the next term is required to also describe the angle-dependent and pulse dependent effects that are the subject of our work. Note that because of the integration variables ω_n the expression can become quite inelegant to evaluate, and the ringdown traces and spectra of the third harmonic can have complicated shapes, arising from the frequency mixing of different frequency components. In our numerical calculations we perform a time-domain calculation

$$\mathbf{j}_{\mathrm{TH}}(\mathbf{r},t) \approx \left(\mathbf{F}_2(\mathbf{r})\right)^3 \left(a_2(t)\right)^3 + 3\left(\mathbf{F}_2(\mathbf{r})\right)^2 \mathbf{F}_1(\mathbf{r})\, a_2(t)^2 a_1(t) \tag{3.20}$$

which is a posteriori numerically Fourier transformed into frequency space

B.4 Diffraction order intensity asymmetry

Evaluating the THG diffraction efficiencies in Fano-resonant metasurfaces would require to numerically evaluate the far field radiated by each of the nonlinear current distributions in Eq. 3.20, which then need to be coherently summed to obtain the emitted intensity. In the limiting case where the contribution from the broad mode $\mathbf{F}_1$ vanishes, the radiation pattern arises solely from the narrow Fano resonance. If we associate the narrow mode to first order with an out-of-plane magnetic dipole mode, the resulting radiation pattern will be an angularly symmetric yet potentially spectrally structured third-harmonic response. This scenario provides a baseline explanation for experimental observations such as the reported spectral shape presented in Fig. 3.3, and supports the notion that spectral tuning of the excitation pulse to overlap with the Fano feature enhances overall THG efficiency. This response is modeled by considering the temporal overlap integral between the driving pulse and the resonant modes, as well as the dependence on the Fano Q-factor. Within this picture of just a single contributing mode, it is impossible to explain asymmetries in diffraction efficiency ratios, and also to explain any frequency structure therein as function of pulse tuning. This independence on pulse tuning is a direct result of the factorization in the temporal and spatial domain. Within this reasoning, the observed tuning-dependent asymmetry therefore must be a result of interference between multiple nonlinear contributions.

An important observation is that diffraction asymmetries and tuning dependencies do arise from the mixing of the first term with the second term in Eq. 3.20. As the laser is detuned, the relative phase and amplitude of the terms $\mathbf{F}_1$ and $\mathbf{F}_2$ evolve, due to the narrow spectral response of $\alpha_2(\omega)$ and the broader but nontrivial response of $\alpha_1(\omega)$. Moreover, the two terms each individually present an angularly symmetric intensity distribution, but they do have different field symmetries. Because the intensity is calculated only after adding the contributing fields, this phase information is highly relevant, allowing for interference effects that manifest as asymmetry in the emitted TH diffraction pattern and spectra (Fig. 3.3), as well as the dispersed spatial jump (Fig. 3.8).

To understand the tuning dependence of the diffraction efficiency, one can begin by analyzing the symmetry properties of the radiation patterns associated with the nonlinear sources, which in turn arise from the linear currents $\mathbf{F}_1$ and $\mathbf{F}_2$. If the broad mode corresponds to an in-plane bright dipole, and the narrow mode to either an in-plane quadrupole or an out-of-plane magnetic dipole, their emitted field profiles have opposite symmetries (even vs. odd). Assuming the broad mode radiates a symmetric diffraction pattern with in-phase contributions to ±1 orders, and the narrow mode contributes equal amplitude but with anti-phase components, diffraction asymmetry arises from their interference. With this reasoning, we conclude that for the plus and minus diffraction orders the efficiencies take the following form

$$\eta_{\pm 1} \propto \int \left| \int \left[\pm A a_2(t)^3 + B a_2(t)^2 a_1(t) \pm C a_1(t)^2 a_2(t) + D a_1(t)^3 \right] e^{-i\omega t}\, dt \right|^2 d\omega \tag{3.21}$$

and for the zeroth order

$$\eta_0 \propto \int \left| \int \left[B a_2(t)^2 a_1(t) + D a_1(t)^3 \right] e^{-i\omega t}\, dt \right|^2 d\omega \tag{3.22}$$

where we have retained all terms in expanding the cubic product. Here A, B, C and D are unknown parameters that in principle require full-wave simulations of the metasurface resonances. These numbers may be complex valued. We treat them as parameters that are to be adjusted to phenomenologically describe the observed data.

B.5 Model parameters

The presented data in Figs. 3.5 through 3.8, all use the following model parameters (Tab. 3.1):

Unknown parameters	**Pulse properties**
$A = -950 + 950i$ $B = 100 + 90i$ $C = 50 - 50i$ $D = 520 + 520i$	$\Delta t = 130$ fs $\beta = -5 \cdot 10^{24}$ rad/s^2

Table 3.1: Unknown parameters used for model output data presented in Figs. 3.5-3.8, and fitted pulse properties

In Section 3.5.4 we mention that the choices of parameters A, B, C and D strongly impact the modeled output. An optimization endeavor might be interesting to find best fits to the measured data, but is rather cumbersome and un-insightful. Therefore, we focused on comparing the key observations from our model to the measured data. To leave the reader with a minimum intuition to the impact of varying the model parameters, we provide an exploration of parameter dependencies in Fig. 3.10. Each panel shows TH spectra, power dependency and TH diffraction contrast calculations for varying a single parameter, while keeping the other parameters at their original value. For each parameter we provide results both for a a higher value and lower value compared to its original set value, as giving in the table below (Tab. 3.2).

	High	Panel	Low	Panel
A	$-1550+1550i$	a	$-550+550i$	b
B	$150+140i$	c	$50+40i$	d
C	$80-80i$	e	$20-20i$	f
D	$750+750i$	g	$250+250i$	h
Δt	200 fs	i	60 fs	j
β	$-8\cdot 10^{24}$ rad/s^2	k	$-3\cdot 10^{24}$ rad/s^2	l

Table 3.2: Exploration of the free model parameters with chosen high and low parameter values with their corresponding panels in Fig. 3.10, while other parameters are fixed as in Tab. 3.1

B.6 Dispersed real-space calculation

Section 3.5.5 presents spectrally dispersed real space images, highlighting phase jumps in the fringe pattern when traversing the wavelength range of the Fano resonances. Figure 3.11 shows a calculation, in which we form a real space image by summing three plane waves with similar amplitudes, that travel in the z-axis under an angle with the y-axis that is dependent on the metasurface grating pitch, exactly as measured

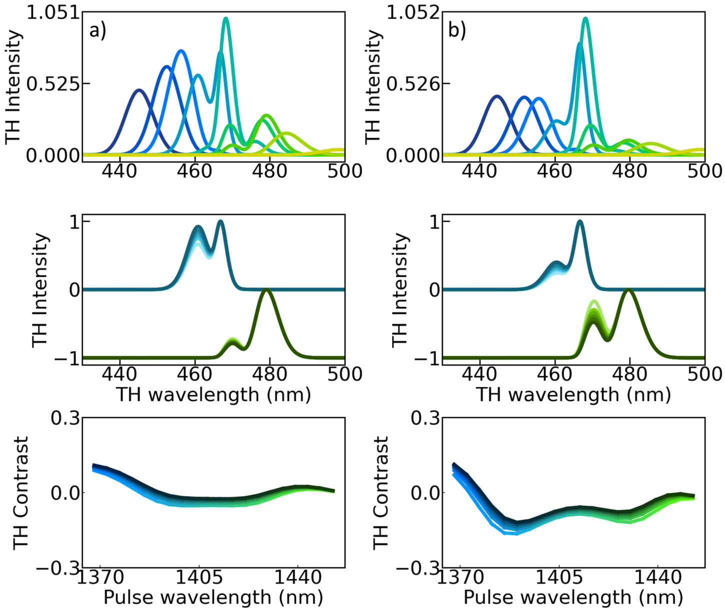

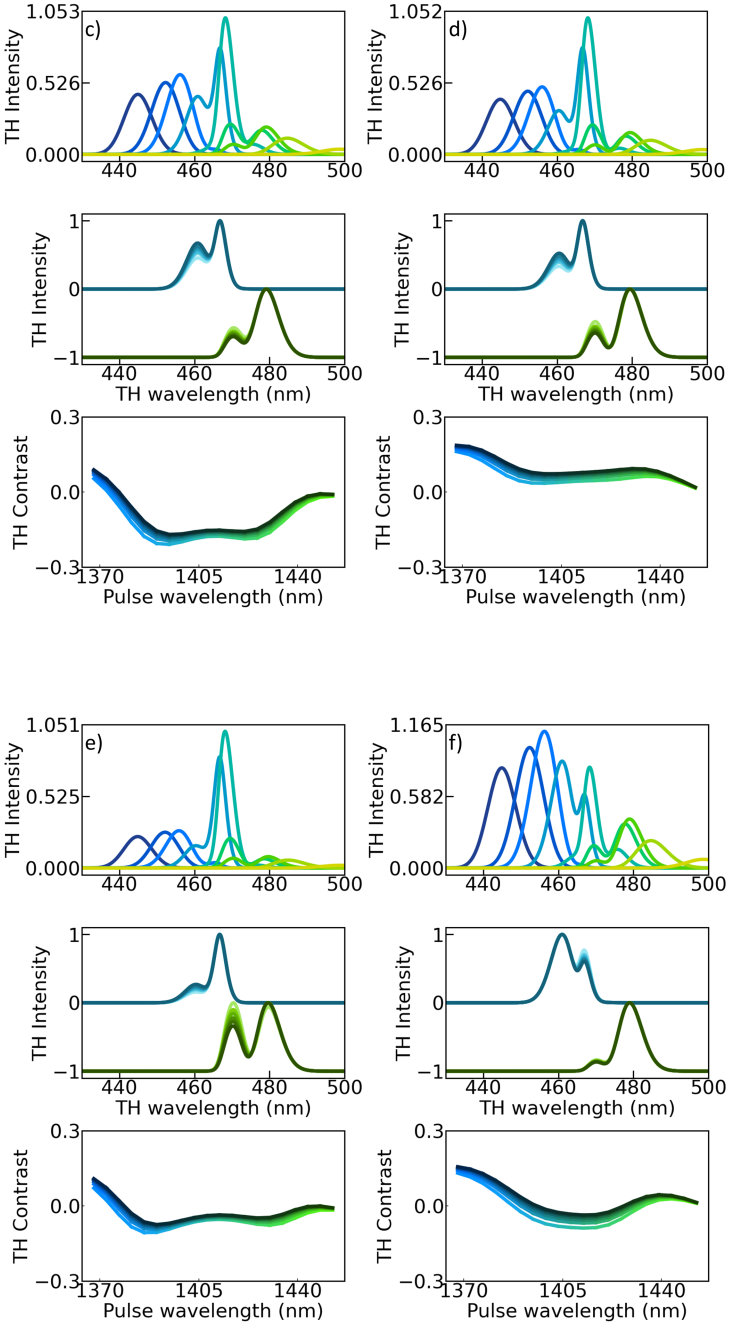
c)
d)
e)
f)
TH Intensity
1.053
0.526
0.000
1.052
0.526
1.051
0.525
1.165
0.582
440
460
480
500
TH wavelength (nm)
1
0
−1
TH Contrast
0.3
0.0
−0.3
1370
1405
1440
Pulse wavelength (nm)

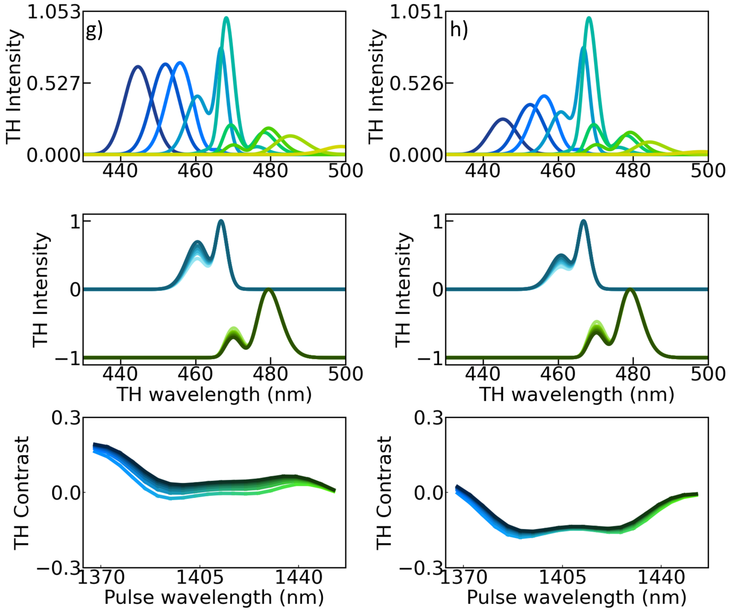
g)
h)
1.053
0.527
0.000
1.051
0.526
0.000
TH Intensity
440
460
480
500
1
0
−1
TH wavelength (nm)
0.3
0.0
−0.3
TH Contrast
1370
1405
1440
Pulse wavelength (nm)

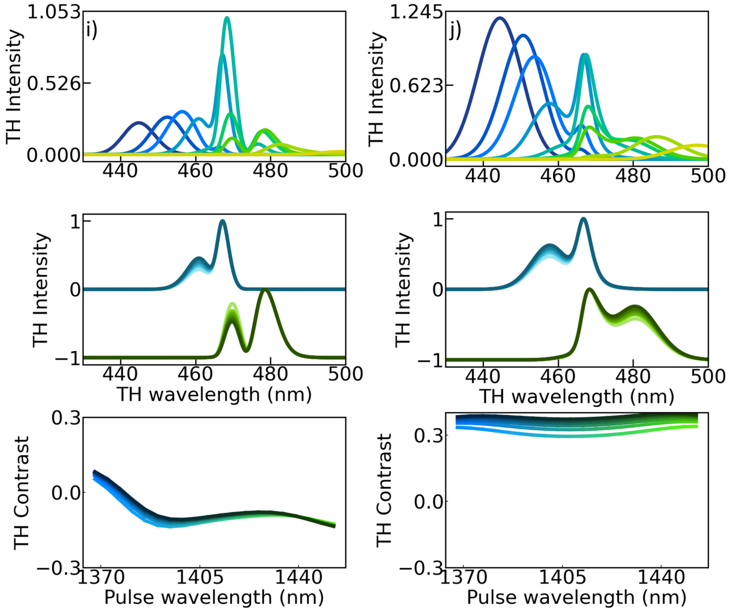
i)
j)
1.053
0.526
0.000
1.245
0.623
0.000
TH Intensity
440
460
480
500
1
0
−1
TH wavelength (nm)
0.3
0.0
−0.3
TH Contrast
1370
1405
1440
Pulse wavelength (nm)

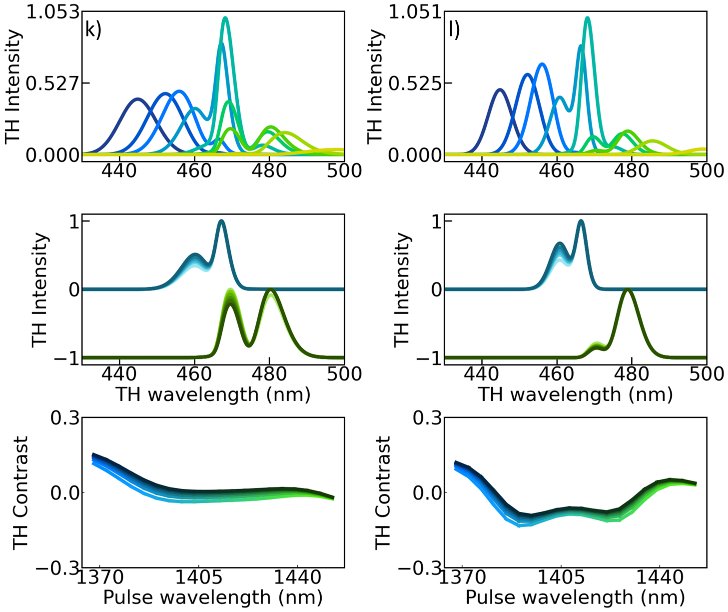

Figure 3.10: Exploration of varying the free parameters in the model. The results show TH spectra, power dependency and TH diffraction contrast, similar to the manuscript, for values given in Table 3.2

in the Fourier space data. Interference between the three waves result from a phase-difference, that is calculated from Eqs. 3.21 and 3.22.

It is important to note the following differences between the measurement and simple model: 1) the measurement is performed with a spatial Gaussian intensity distribution and a Gaussian spectral distribution of the pump beam, whereas the simple model uses plane-waves with homogeneous amplitude over space and frequency, and 2) in this simple calculation, all three diffraction orders (-1,0,+1) carry a similar amplitude, instead of accounting for the actual diffraction efficiencies. However, the important feature in the dispersed real-space the jumps in the fringe pattern at certain wavelengths are independent of these assumptions.

C Experimental setup

Our experimental setup (schematic setup in Fig. 3.12) produces 130 fs pulses at 1 MHz repetition rate that are generated in a LightConversion Orpheus OPA that is fed from a LightConversion Pharos 1030 nm laser. We use the idler to achieve pulses at the wavelength range of interest. A longpass filter of 1000 nm (Thorlabs FELH 1000) removes residual pump. We use a set of a halfwave plate (HWP, Thorlabs AHWP10M-1600) and a linear polarizer (LP, Thorlabs LPVIS050-MP2) to control incoming pulse fluence and polarization. An ND filter with OD = 1 (not shown) is placed after the linear polarizer, further reducing the pump power by one order of magnitude. A broad

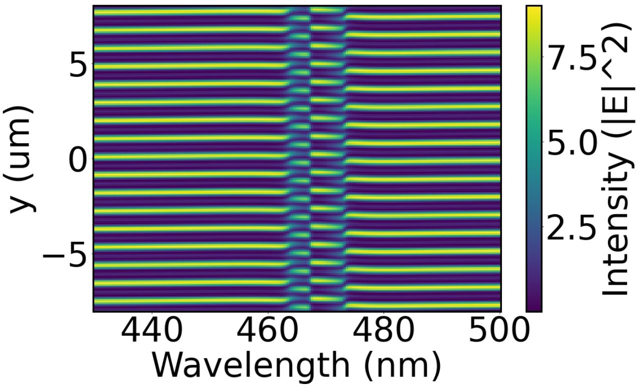

Figure 3.11: Dispersed real-space calculation. The three vertical diffraction orders 0, -1 and +1 interfere under an angle in the y-direction, that is given by the metasurface pitch. The intensity ($|E|^2$) is plotted in colorscale shown in the colorbar.

white light halogen lamp (AvaLight-HAL-S-Mini) can be coupled in to produce spectra at the fundamental wavelength. The beam is loosely focused by a f$=$ 30C-coated lens (Thorlabs) and enters the sample from the backside. Emitted TH and transmitted IR pump, or white light, are collected in transmission side via a microscope objective (Nikon AC API plan, NA 0.9, $100\times$). A dichroic mirror (Edmund Optics 69-900) transmits the IR, that feeds into an optical spectrum analyzer (Thorlabs, OSA202C), and reflects the TH. The TH passes through a set of 2 IR filters (Thorlabs TF1), to further reduce pump intensity, after which it can be fed into a spectrometer (Ximea MC124MG-SY-UB) or directed to a visible camera (Teledyne Prime BSI Express). Via a 1:1 telescope that allows real- and Fourier space filtering, our so-called Fourier lens images the back focal plane of the objective. This allows to measure the angle resolved TH emission information. Without Fourier lens, the sample plane is imaged, creating real space TH images.

D Double gaussian fit to TH spectra

To track the main peak and the shoulder intensities in Fig. 3.4b), we fit a double Gaussian to the TH spectra. The double Gaussian is of the form

$$y(x) = H + A\exp\left(-\frac{(x-x_1)^2}{2\sigma_1^2}\right) + B\exp\left(-\frac{(x-x_2)^2}{2\sigma_2^2}\right) \tag{3.23}$$

with x the wavelength, y the TH intensity, H a constant baseline offset that is in our case close to 0, A the amplitude of the first Gaussian main broad peak with x_1 the center wavelength that we keep close to the fundamental wavelength/3 and σ_1 the standard deviation that controls the peaks spread, and B, x_2 and σ_2 the amplitude, center wavelength and standard deviation of the second shoulder narrow peak that is concentrated around the Fano wavelength/3. Figure 3.13 shows 6 example fits to measured spectra, that are also presented in the manuscript in Fig. 3.4. Figures 3.13a-c) show the double Gaussian fit to spectra acquired by exciting with a pump pulse

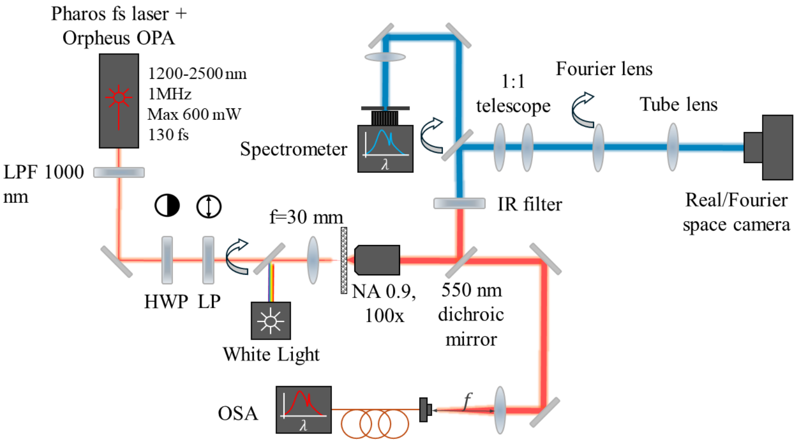

Figure 3.12: Experimental setup of our home-built nonlinear Fourier microscope.

centered at 1388 nm, at a) 0.3 mW, b) 0.6 mW and c) 1.1 mW in black solid, experimental in gray dots. The orange (blue) dashed curve depicts the main (shoulder) Gaussian associated to the output of mode a_1 (a_2), and the filled area beneath the curve indicates the integrated intensity that is plotted in Fig. 4b). Figures 3.13d-f) shows similar example fits, for a pulse that is centered at 1436 nm at d) 0.4 mW, e) 0.7 mW and f) 1.2 mW.

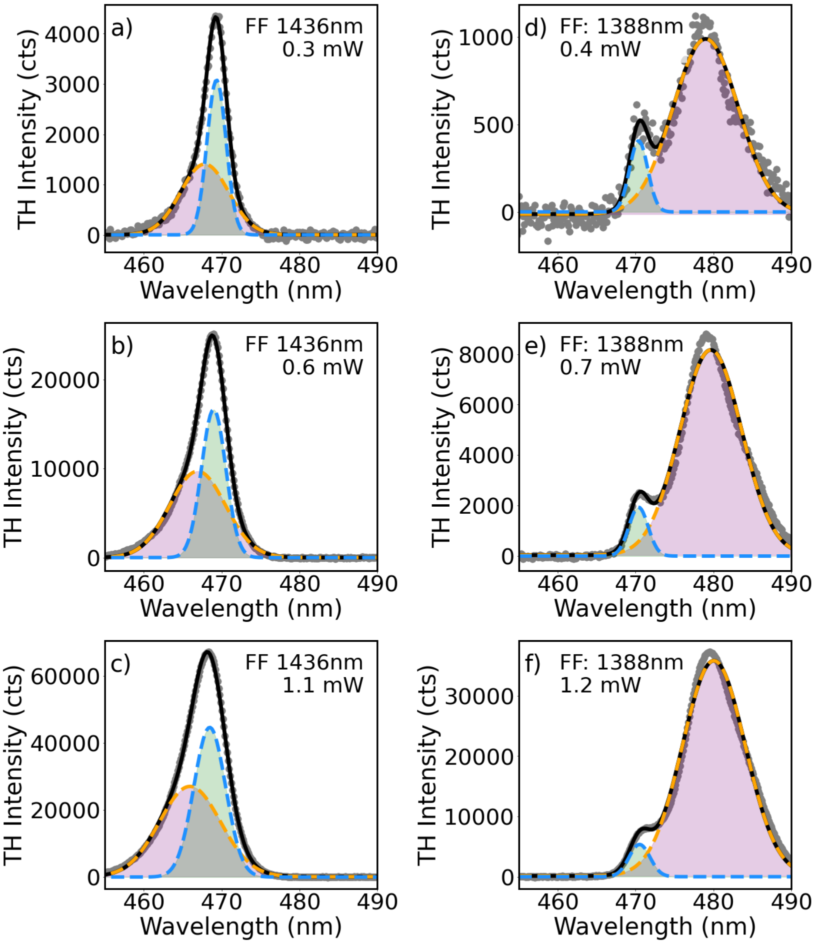

Figure 3.13: Double Gaussian fits to measured TH spectra. The measured spectra are plotted in solid gray dots, the double Gaussian fit in black solid, which is composed of two single Gaussians that are called the main peak in orange dashed and the shoulder in blue dashed. The integrated intensity of the peak is indicated by the marked area beneath the fits.

Chapter 4

Near-Unity All-Optical Modulation of Third-Harmonic Generation with a Fano-Resonant Dielectric Metasurface

We demonstrate all-optical modulation with a near-unity contrast of nonlinear light generation in a dielectric metasurface. We study third-harmonic generation from silicon Fano-resonant metasurfaces excited by femtosecond pulses at 1480 nm wavelength. We modulate the metasurface resonance by free carrier excitation induced by absorption of an 800 nm pump pulse, leading to up to 93% suppression of third-harmonic generation. Modulation and recovery occur on (sub)picosecond times cales. According to the Drude model, the pump-induced refractive index change blue-shifts the metasurface resonance away from the generation pulse, causing a strong modulation of third-harmonic conversion efficiency. The principle holds great promise for spatiotemporal programmability of nonlinear light generation.

4.1 Introduction

In recent years a strong interest has emerged in all-dielectric optical metasurfaces [196]. Metasurfaces are nanopatterned 2D systems of strongly scattering meta-atoms arranged at subwavelength spacings, each tailored in their response through shape, size, and orientation. This provides the capability to manipulate amplitude, phase, and polarization of light passing through metasurfaces in completely new ways, leading to applications as flat imaging optics [197], augmented reality devices [198], holography [199], polarimetry [200], sensing [81], spectroscopy [201], and optical signal processing [202]. Nonlinear metasurfaces offer many additional opportunities, for instance in second, third- and high-harmonic generation and four-wave mixing (SHG, THG, HHG, and FWM) [165, 185]. These opportunities arise through a confluence of unique properties. First, very large conversion efficiencies are possible by engineering strong resonances. Second, since interaction lengths are far below the wavelength scale, phase-matching requirements are absent. Third, complex wavefronts can be imprinted at will on nonlinear output beams by rational design. A potent route to efficient generation is provided by Fano-resonant metasurfaces. Several groups demonstrated efficient THG and HHG [58, 97, 203], nonlinear holography [103], THz wave generation [204], nonlinear beam steering [102], nonlinear imaging [108], and EUV beam shaping [205].

Widespread application of metasurfaces is limited by the fact that function is fixed at fabrication time, and often the ability is lacking to dynamically control function. Removing this limitation is widely recognized as a main objective. For instance, to advance metasurfaces for analog wave-based processing, it is crucial to develop tunable versions that allow high-contrast and ultrafast control over their linear optical responses [191]. Similarly, when metasurfaces are used for nonlinear generation, it is highly desirable to dynamically control output beam profile, brightness, wavefront, or polarization. Efforts to create dynamically controllable metasurfaces [183, 191] have so far mainly relied on changes in geometry [206], in optical environment surrounding the meta-atoms [207], or index changes in the meta-atoms [139, 208, 209]. These changes are realized by temperature tuning [208], electrical gating [210], strain [206], phase-change materials [139], or switchable substrates [207]. Recently, with the use of a nonlinear metasurface, interferometric routing into diffraction orders achieved up to 90% modulation efficiency [211]. Although previous studies demonstrated remarkable modulation depths [137, 210], picosecond switching times [97] and large routing efficiencies [211] it is an open challenge to reach high-contrast ultrafast modulation in the visible and telecom wavelength domain.

In this Chapter, we demonstrate picosecond all-optical modulation of nonlinear light generation by a silicon-based all-dielectric Fano-resonant metasurface with near-unity contrast. On basis of the observed transient harmonic generation deactivation, we argue that the all-optical control is based on free carrier excitation upon absorption of the pump pulse, which modulates the silicon refractive index. This index modulation detunes the sharp Fano resonance, and as a consequence dramatically changes the near-field enhancement for the nonlinear generation process and thereby the harmonic conversion efficiency. We argue that this mechanism is generally applicable to Fano-resonant semiconductor metasurfaces, and provides a route to ultrafast dynamic and spatial control of nonlinear light generation.

4.2 Sample and setup

The main idea of our experiment is sketched in Fig. 4.1: we excite a sample with ‘generation pulses’ around 1480 nm and study the third-harmonic (TH) signal that it generates in a pump-probe set-up, where an 800 nm pump pulse modulates the TH conversion efficiency by detuning the metasurface. We choose a disk-bar metasurface with a Fano resonance near 1480 nm, advantageous for efficient harmonic generation [97]. This design is not specifically tailored for this work, and we take it as a simple, well-established THG generating motif to explore the potential of all-optical modulation of THG generation in Fano-resonant metasurfaces.

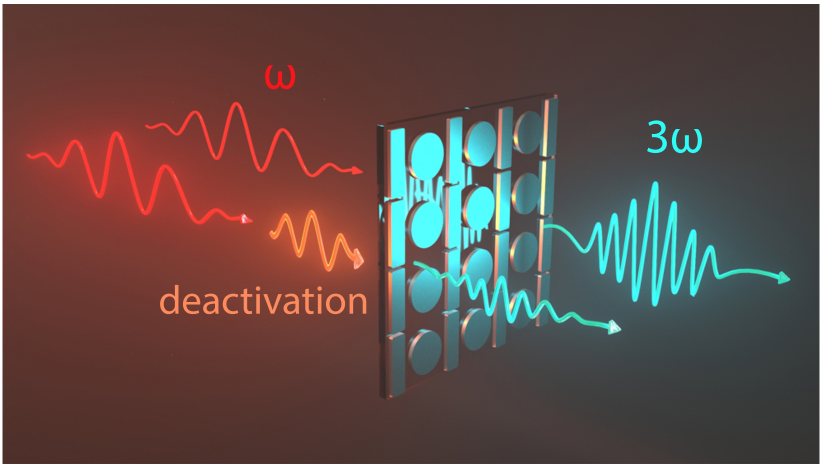

Figure 4.1: Sketch of our scheme to optically modulate harmonic generation by a metasurface. An IR excitation pulse is loosely focused on the Fano-resonant metasurface, and converted into a bright third-harmonic signal. Depending on the time delay Δt with respect to the IR excitation pulse, a visible pump pulse can almost fully suppress the harmonic generation.

4.2.1 Fano resonant disk-bar metasurface

The metasurface (scanning electron micrograph Fig. 4.2a) is fabricated in polycrystalline silicon evaporated (d = 135 nm thickness) on fused quartz, patterned with e-beam lithography. The sample consists of a square grid (900 nm pitch) of unit cells consisting of 240 nm radius disks adjacent to 800×205 nm bars. Appendix A reports in detail on nanofabrication, and Appendix B presents schematics of the experimental setups. The narrow Fano resonances in linear transmission reveal a quality factor of around $Q = 215$, (Fig. 4.2b) and are superimposed on the broad dipole resonance of the bar, which is excited by linear input polarization along the bar. A Fano line shape analysis is found in Appendix A. In a standard THG setup (130 fs pulses at 1 MHz repetition rate, with a spot size radius around $r = 11$ μm, from a LightConversion Orpheus OPA, tuned near the Fano resonance) the sample presents bright THG, as evident from the emission spectrum and power dependence (Fig. 4.2c and d). Compared to bare silicon the THG spectrum is a factor 10^3 brighter, owing to the coupled disk-bar resonance (experimental conditions: integration time 400 ms, at 1 MHZ repetition rate and 0.33 mJ/cm^2 fluence). At modest input fluences (1 mW input power, i.e. 0.1 mJ/cm^2 per pulse), the THG intensity increases with a power law close to 3, while for larger fluences (power above 3 mW) the TH intensity shows a typical saturation behavior. This saturating dependence is commonly ascribed to two-photon and free carrier absorption [165, 188, 190, 212].

4.2.2 Ultra-fast pump-probe setup

The pump-probe setup is based on a Solstice Ace (Spectra-Physics) ultrafast amplifier (2 kHz repetition rate), that amplifies Ti:sapphire laser pulses to millijoule levels. Part of the 800 nm beam feeds into an optical parametric amplifier (TOPAS Prime, LightConversion) that outputs probe pulses at 1480 nm of 51 fs (fwhm) duration. Appendix B reports on pulse characterization. The remainder of the 800 nm beam is used as pump pulse of 72 fs after passing through an attenuator and delay-stage to control the arrival time relative to the probe pulse. Both pump and probe are loosely focused, with an approximate pump spot size of 275 μm covering the entire 200 μm metasurface field, and a smaller probe spot with fwhm 62 μm. Half-wave plates independently control the input polarization of both beams. For the remainder of this Chapter we refer to the 800 nm pump as ‘deactivation pulse’ as it suppresses the harmonics generated by the infrared ’generation pulse’.

4.3 Ultra-fast control of THG

Figure 4.3 presents the main result of our study, i.e., transient, almost complete, suppression of third-harmonic generation. Figure 4.3a reports the

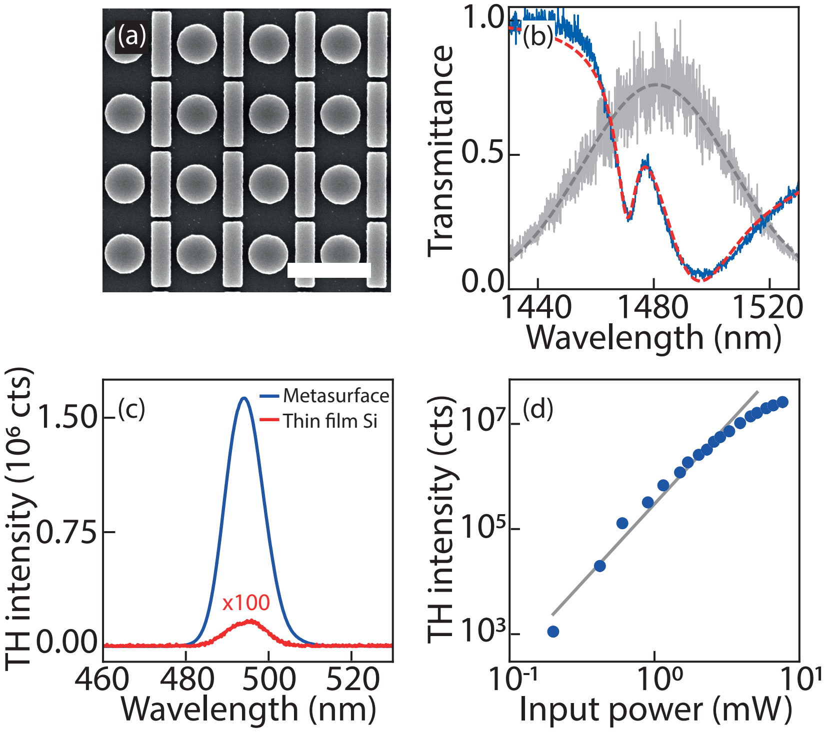

Figure 4.2: Metasurface properties: (a) scanning electron micrograph of silicon disk-bar metasurface (scale bar 1 μm. Pitch 900 nm, disk radius $r = 240$ nm, bar width and length $w = 205$ nm and $l = 800$ nm with gap between disks and bars circa $g = 50$ nm. Si height is $h = 135$ nm). (b) Linear transmittance (blue) with a Fano resonance fit (red dashed) showing a quality factor $Q = 215$. For reference the excitation pulse (grey, Gaussian fit dashed) is also shown. (c) TH spectra generated from the metasurface (blue) and unpatterned silicon film (multiplied by 100 for visibility) on the same substrate. (d) Summed TH signal versus input power (blue dots - line shows cubic power law).

THG spectrum as a function of delay between the generation and deactivation pulse. Negative times correspond to deactivation pulses arriving after the generation pulse, which provides the reference behavior (no deactivation). Just after temporal overlap (maximum suppression occurs at time delay $\Delta t = 100$ fs) the THG signal is clearly reduced by approximately 93%, as also quantified in the crosscuts (panel b). This specific measurement is carried out at a pump fluence of 8.5 mJ/cm^2. The spectra also present a feature at 550 nm which is due to four wave mixing (FWM, occurring at twice 800 nm minus 1480 nm). The FWM signal requires exact temporal pulse overlap owing to the instantaneous nature of the required nonlinearity, and indeed occurs only in a single time bin of 100 fs and therefore serves as a yardstick for $\Delta t = 0$. In contrast, the TH suppression relaxes on a slower time scale of a

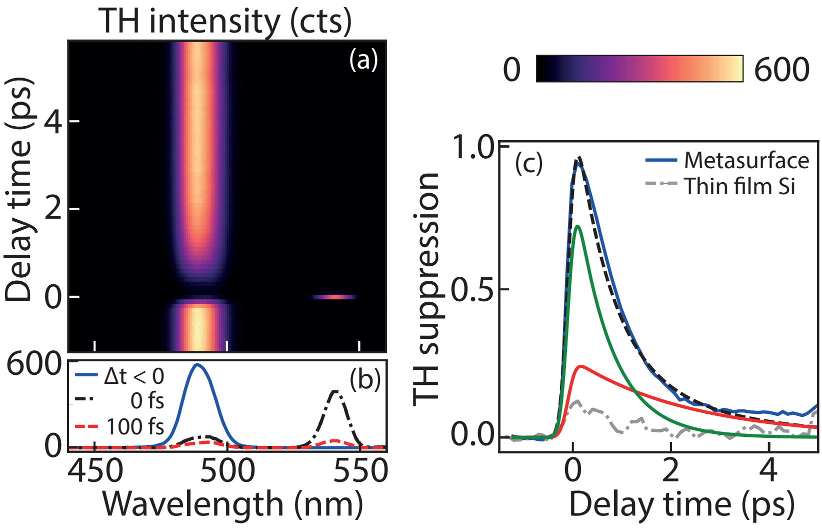

Figure 4.3: Transient behaviour of the THG spectrum, which is exposed to a deactivation pulse (pump fluence 8.5 mJ/cm^2) at time $\Delta t = 0$ps. (a) TH intensity as function of pump-probe delay and wavelength. (b) Spectral crosscuts from panel (a) at time $\Delta t < 0$ (blue),v $\Delta t = 0$ (black dash-dot) and $\Delta t = 100$ fs (red dashed). (c) TH suppression dynamics for the metasurface (blue) and thin film reference (grey dot-dashed), at the same experimental conditions. TH suppression is fitted with a biexponential curve (black dashed) showing two decay mechanisms with a fast (green) and slow decay rate (red).

few picoseconds.

To quantify the intensity reduction dynamics we examine the TH suppression as a function of time, plotted in Fig. 4.3c. The TH suppression is defined as $S = 1 - I(\Delta t)/I_0$ where $I(\Delta t)$ refers to the intensity at delay Δt spectrally integrated from 460 nm to 510 nm, and where we normalize to the integrated THG intensity I_0 in absence of the deactivation pulses (at negative Δt). For reference, we also report the transient TH suppression taken at the same experimental settings but on unpatterned silicon film on the same sample substrate. The very large 93% THG suppression at $\Delta t = 0$ for the metasurface is at least 7.5 times larger than the 12% suppression observed in the thin film reference. This underlines the important advantage of the resonant mode structure of the metasurface, which not only is instrumental for a large THG efficiency, but also for the achievable modulation depth.

4.4 Photo-excitation of carriers

We hypothesize that the remarkably strong modulation of THG results from free carriers that are generated by direct absorption of the pump. Indeed, the picosecond timescales of the suppression point at free carrier dynamics. In

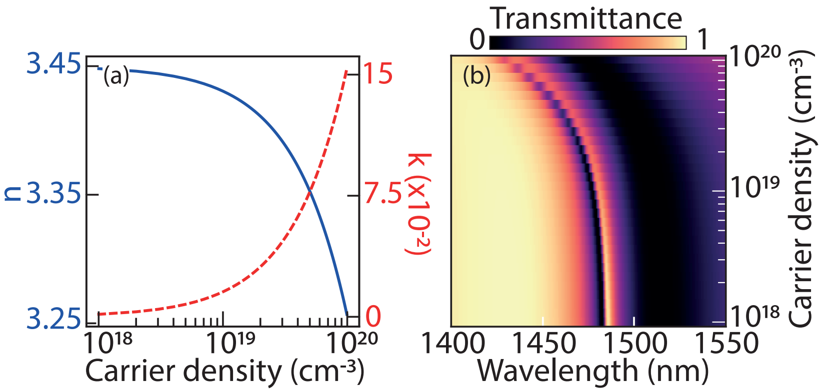

Figure 4.4: Drude model analysis: (a) calculated real (blue) and imaginary (red dashed) refractive index of poly-Si as function of carrier density, (b) simulated metasurface transmittance as function of excited carrier density and wavelength.

this picture, the suppression arises because free carriers change the refractive index, detuning the metasurface relative to the probe. This detuning results in a strong reduction in THG since the conversion efficiency strongly depends on relative tuning of metasurface and generation pulse according to experiments on unswitched metasurfaces excited by wavelength-tuned laser pulses [97, 165, 203]. Optical switching due to free carrier excitation in silicon was studied extensively in context of photonic crystals, starting with work by Leonard et al. [213]. Key expected features are that instantaneous direct pump absorption excites free carriers, which give rise to a strong change of the silicon refractive index at the generation probe frequency described by the Drude model. Thermalization of electrons on time scales of picoseconds, and subsequent carrier recombination on time scales of 10-1000 ps then lead to multi-exponential temporal evolution back to the unexcited state. To evaluate this hypothesis, we computed the complex-valued refractive index change as function of carrier density (Fig. 4.4a) according to the Drude model which we then used as input for COMSOL finite element calculations of metasurface transmittance. A simplified version of the Drude model, lumping together contributions of electrons and holes, reads [214–216]

$$n(\omega) \approx n_{BG} - \frac{1}{2n_{BG}} \left(\frac{\omega_p}{\omega}\right)^2 \left[1 - \frac{i}{\omega \tau_D}\right]$$

with $n_{BG} = 3.45$ the unexcited Si refractive index, $\tau_D \approx 10^{-14}$ s the relaxation time relevant for polycrystalline Si, and ω_p the fluence-dependent plasma frequency $\omega_p^2 = e^2 N/(\epsilon_0 m_{opt}^*)$ with N the density of electrons plus holes, and $m_{opt}^* = (m_e^{-1} + m_h^{-1}) = 0.15 m_e$ the effective carrier mass in units of the mass m_e of the electron. According to the Drude model substantial refractive index changes of order $\Delta n = 0.05$ occur for carrier densities above

$N > 10^{19}$ cm^{-3}, with the change Δn mainly in the real part as we operate at $\omega\tau_D \approx 10$. The metasurface resonances display a large wavelength sensitivity to refractive index changes, associated to strong local fields in the silicon. At carrier densities of order $N = 10^{19}$ cm^{-3} already a full linewidth change of the Fano resonance occurs. At larger excitation density ($N = 5 \cdot 10^{19}$ cm^{-3}) the index changes cause the resonance to be completely shifted spectrally away from the generation pulse.

4.4.1 Excited carrier estimation

To place our experiment in context of the Drude model, we estimate the generated carrier densities by assessing the absorbed photon flux. We illuminate with 800 nm deactivation pulses of circa $\Phi \approx 7 \cdot 10^{15}$ photons / cm^2 as estimated for 1 μJ pulse energy, and circa 275 μm spot diameter. COMSOL simulations predict an absorption coefficient A of order 3.4% at 800 nm (see Appendix D), indicating that we reach excited carrier densities of up to $N \approx 2\Phi A/d = 10^{19}$ cm^{-3} (with $d = 135$ nm the Si thickness). Resonance shifts by a full linewidth are hence fully in range of our experiment. As the THG intensity scales with third power of the near-field intensity of the generation pulse, even small modulations of the resonance cause a large suppression (e.g., the 93% suppression requires only a 58% change in near field intensity for the fundamental). Our observation of THG suppression can thus be rationalized as a blue-shift of the resonant feature caused by excited carriers, which thereby shifts spectrally away from the generation pulse, causing a strong reduction in THG conversion efficiency. As we estimate $\omega\tau_D = 10$, our model favors the blueshift over free carrier absorption as main contributor.

4.5 Saturation and polarization analysis

TH suppression measurements were carried out for pump fluences between 0.2 and 8.5 mJ/cm^2. Figure 4.5a shows that the suppression saturates with increasing pump fluence. A modest 50% suppression is already reached at 1.6 mJ/cm^2, whereas the extreme 93% suppression is achieved at 8.5 mJ/cm^2. Higher input fluence resulted in sample damage. To understand the recovery dynamics of the THG as a function of pump fluence, we fitted biexponential transients for all pump fluences and extracted recovery rates. Transient suppression data and fits for all pump fluences are found in Appendix C. The suppression dynamics are excellently fitted by a biexponential $S(\Delta t) = a_1 e^{-\gamma_1 \Delta t} + a_2 e^{-\gamma_2 \Delta t}$ with associated fitted decay rates γ_1 and γ_2 shown in Fig 4.5b. We ascribe the fast decay to thermalization of excited carriers, which are slightly faster than reported timescales in other works for monocrystalline Si [213, 217, 218]. Our metasurface is actually made of polycrystalline silicon, which makes thermalization likely to happen on a faster timescale [219]. The

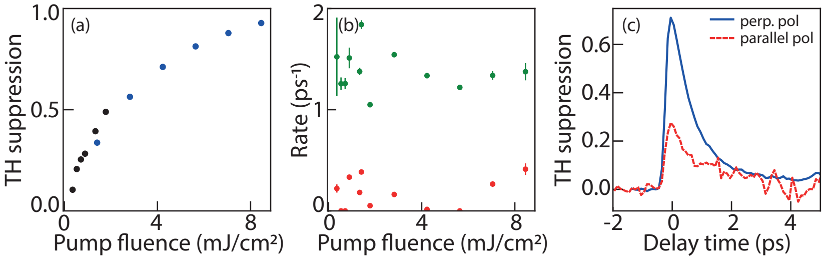

Figure 4.5: (a) Maximum TH suppression versus deactivation pulse fluence. Different colors (black and blue) correspond to two separate measurement runs. (b) Green (red) symbols: fitted decay rates for biexponential transients versus deactivation pulse fluence for the fast (slow) decay component (c) TH suppression transients at a deactivation pulse fluence of 5.3 mJ/cm^2, polarized perpendicular (parallel) to the generation pulse in blue (red dashed).

slow decay rate we ascribe to carrier recombination. The fitted timescales range from 2 ps to $\gg$ 10 ps (exceeding the range of our experiment), slightly faster than values reported in literature [217]. The rates are essentially independent of pump fluence.

We measured THG suppression for perpendicular and parallel polarization of the deactivation pulse relative to the metasurface bar (Fig. 4.5c). At perpendicular polarization the suppression is a factor $\sim$ 3 larger compared to the parallel case at identical power. We ascribe this to a different near-field distribution and concomitant difference in absorbed power depending on polarization of the deactivation pulse. COMSOL simulations predict 2.3% absorbed power at 800 nm for parallel polarization, versus 3.4% at perpendicular polarization (Appendix D). As THG is a third order process, the absorbed power ratio $(2.3/3.4)^3$ is commensurate with the observed threefold in suppression. The structures at hand are not particularly optimized for polarization dependent near-field distributions at the pump wavelength. In principle, this observation shows that shaping the pump near field provides a route to spatio-temporal control of harmonic generation. Pump field shaping can be achieved by structuring the paraxial incident beam and by engineering the meta-atoms to present spatially varying responses to the pump through, *e.g.*, polarization/orientation and local resonance engineering.

4.6 Conclusion

In summary, we observed near-unity contrast optically controlled suppression of third-harmonic generation that is generated in an all-dielectric resonant metasurface. We explain the suppression by transient detuning of the metasurface resonances relative to the probe pulse, which occurs due to modulation of the complex refractive index of the material through optical excitation of free carriers. These results, combined with the fact that we achieved a very strong modulation strength in an easily fabricated, indirect semiconductor band-gap, and un-optimized metasurface, have important implications for a wide range of nonlinear metasurface applications. Nonlinear metasurfaces attract large interest as efficient nonlinear sources of structured light beams, high harmonic beams, and even nonlinear holograms, with applications in free space optics, EUV metrology, microscopy, and as integrated optics sources. The work presented in this Chapter enables high-contrast, fast dynamical control and spatial programmability of generated light, greatly advancing the versatility of nonlinear metasurfaces beyond function fixed at nanofabrication. While the suppression achieved here is already remarkably strong, there are many avenues for optimization. Recent work by Koshelev et al. indicates that nonlinear conversion efficiency depends not only on detuning, but also on linewidth matching of probe spectrum and metasurface resonance [165]. This offers the perspective of control not only via resonance tuning, but also via optically induced quality-factor control. Monotonic tuning from high to low Q (*e.g.,* by induced free carrier absorption) can lead to both TH enhancement (bringing a system from undercoupling to critical coupling), and TH suppression (into the overcoupled regime). Further, by engineering an absorption resonance at the pump wavelength we anticipate that the required pump fluences can be reduced by an order of magnitude. Since these effects essentially rely on refractive index tuning at the fundamental wavelength and not on, e.g., Kerr-type wave-mixing [220], it will also directly apply to high harmonic generation [185]. An interesting direction for future research (which is presented in the next Chapter 5) is to apply pump beams that are structured in space or polarization, thereby imprinting dynamically controllable spatial structure in the harmonic suppression or enhancement [123]. The harmonic generation inherits not only its amplitude but also its local phase pickup from the metasurface. Together, this provides rich opportunities to dynamically control nonlinear generation of structured light [102, 125], such as orbital angular momentum and vector vortex beams [221, 222]. Finally, in combination with structured illumination our system allows a better understanding of spatiotemporally varying and temporally switched near fields in metasurfaces, accessible via microscopic and interferometric mapping of third-harmonic conversion efficiency.

Appendices

A Sample fabrication and resonance characterization

A standard e-beam lithography recipe was used to fabricate the nanostructures. First, fused quartz substrates of 12×12 mm and 500 μm thick (Siegert Wafer GmbH) were cleaned by sonication in H_2O for 10 minutes, followed by a dip in a base piranha solution at 75°C for 15 minutes and afterwards rinsed with water and isopropanol (IPA). A layer of 135 nm polycrystalline silicon was evaporated by e-beam evaporation (Polyteknik Flextura M508 E) heating silicon pellets with an emission current of 90 mA to generate a deposition rate of 0.1 nm/s. Next, the sample is put in an oxygen plasma for 2 minutes to grow a thin passivation layer to protect the silicon during development later and to promote adhesive capabilities to the resist layer. Then, a Hydrogen silesquioxane (HSQ) resist layer (Dow Corning, XR-1541 E-Beam Resist) of ca. 65 nm is spincoated with 3000 rpm, 1000 rpm/s, 45 s, and baked at 180°C for 2 minutes. To avoid charging during patterning, a thin conductive layer of Elektra (All Resist GmbH, Electra 92) spincoated, 2000 rpm, 1000 rpm/s, 60 s, on top of the HSQ and baked for 2 minutes at 90°C. Patterning is done by exposure to an electron beam in Raiths Voyager system, using an average dose of 1500 μC/cm^2 (50 kV). The development consists of a dip in water for 15 seconds to remove the elektra layer, 70 seconds in TMAH at 60°C, followed by a rinse of water and IPA for 15 seconds each. The last step is to transfer the HSQ mask in the silicon, which we did via reactive ion etching (Oxford Instruments, Plasma Technologies Plasmalab 80 Plus) using a chemistry of $CHF_3/SF_6/O_2$ (15/10/3 sccm, Forward power 150 W, chamber pressure 7 mTorr), which etches ca. 45 nm/minute. Excess resist layer is not removed, as this did not change the optical properties or impact the quality of the experiment significantly.

The metasurfaces were designed such to present Fano lineshapes between 1400 and 1550 nm. Fano resonances are a result of the coupling between a broad (bright) and a narrow (dark) resonance. In our case, the broad mode is an electric dipole that is located along the long axis of the bar, whereas the narrow mode is a magnetic mode located inside the disk, pointing out of the plane. To calculate the quality factor Q of the Fano resonance, the following procedure is used. First, we set up an equation for the transmission profile of a set of coupled oscillators

$$T = 1 - \chi\sqrt{\gamma_1} \tag{4.1}$$

with γ_1 the total loss of the broad resonator, and χ the susceptibility

$$\chi = M \cdot I \cdot 2\sqrt{\gamma_1}\, i\omega \tag{4.2}$$

with I the unity matrix, ω the frequency of the light, and M the coupled oscillator matrix

$$M = \begin{pmatrix} -\omega^2 + if\omega\gamma_1 + \omega_1^2 & -i\kappa_{12} & -i\kappa_{13} \\ i\kappa_{12} & -\omega^2 + i\omega\gamma_2 + \omega_2^2 & 0 \\ i\kappa_{13} & 0 & -\omega^2 + i\omega\gamma_3 + \omega_3^2 \end{pmatrix} \tag{4.3}$$

where f tunes leakage (and $f = 1$ means impedance matched), ω_n the resonance frequency of the n^{th} oscillator, κ_{12} the coupling between the broad and narrow resonator, κ_{13} the coupling between the broad and another broad resonator, and γ_2 and

γ_3 the losses of the narrow and second broad resonators respectively. We introduced a third oscillator in our analysis, as our experimental data showed a typical strong asymmetric Fano lineshape, superimposed on a slight asymmetric broader resonance profile. This slight asymmetric broad resonance, we ascribed to the coupling between two broad resonances.

Fitting to experimental data, we found the values

$\lambda_1 = \frac{c}{\omega_1}$	$\lambda_2 = \frac{c}{\omega_2}$	$\lambda_3 = \frac{c}{\omega_3}$	$Q_1 = \frac{\omega_1}{\gamma_1}$	$Q_2 = \frac{\omega_2}{\gamma_2}$	$Q_3 = \frac{\omega_3}{\gamma_3}$	κ_{12}	κ_{13}	f
1502.8 nm	1472.4 nm	1530.5 nm	48.98	215.6	20.81	$(20.22\,\gamma_2)^2$	$(4\,\gamma_3)^2$	1

Table 4.1: Fitted parameter values of the Fano model to experimental transmission data.

Note that the quality factor Q is calculated as ω/γ, as it gives the amount of oscillations at a given frequency. The quality factor $Q = 215$, stated in the main text, is the Q_2 extracted from this fit. These values lead to the fit to the experimental transmission presentend in Fig. 4.6

B Experimental setup and pulse characterization

In this Appendix, we present schematics of the experimental setups that were used for sample characterization and ultrafast TH suppression measurements. Furthermore, the deactivation and generation pulses are characterized and analyzed.

B.1 Setup schematics

In the experimental setup for sample characterization measurements, pulses from a femtosecond optical parametric amplifier (idler from OrpheusF, LightConversion) are slightly focused on the sample. A collection objective of NA 0.9 (100×, Nikon, CFI Plan

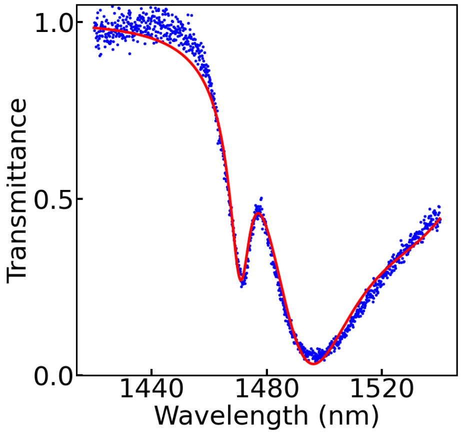

Figure 4.6: Transmittance measurement for the metasurface described in the main text in blue dots, with a coupled oscillator Fano lineshape fit plotted as the red solid line.

Apo BD) collects all light in transmission. A set of filters (Thorlabs Inc., FESH0650) in combination with a dichroic mirror (not shown in the schematic, Edmund Optics, Dichroic longpass filter 600nm 69-879) transmits the third-harmonic, while blocking out the infrared light. The schematic of this setup is presented in Fig. 4.7.

The experimental setup used for transient deactivation measurements is based on a modified Mach-Zehnder-interferometer. One path sends a converted 1480 nm beam through the sample for harmonic generation. The other path is for the 800 nm beam. The 800 nm beam passes through a delay stage, allowing for control over the time of arrival with respect to the 1480 nm beam. In addition, a set of HWP and linear polarizer (Eksma, thin-film polarizer) is used as attenuator.

B.2 Deactivation pulse characterization

The wavelength and the duration of the deactivation pulse were measured via the frequency-resolved optical gating (FROG) technique. We measured the second harmonic of the pulse, generated in a 20 μm thick β-barium borate crystal (BBO), as this was easier in our setup. Figure 4.9 presents the pulse characterization measurements, with on the left: reconstructed FROG trace showing intensity as a function of both wavelength and time, and on the right: normalized intensity plotted as a function of time. A Gaussian distribution is fitted to the date, which gives a FWHM of 72 fs.

B.3 Beam profile measurement

The beam profile was measured for the deactivation pulse at 800 nm. In Fig. 4.10, Gaussian distributions are fitted to the beam profile with $\sigma_x = 131$ μm and $\sigma_y = 102$ μm. These correspond to full-width half-maximums in the x-direction of 310 μm and in the y-direction 241 μm. Our estimation of the spot size of 275 μm derives from these values.

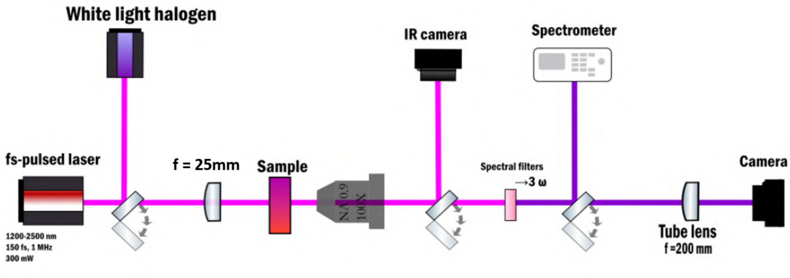

Figure 4.7: Schematic of the experimental setup that is used for sample characterization measurements, shown in Fig. 4.2

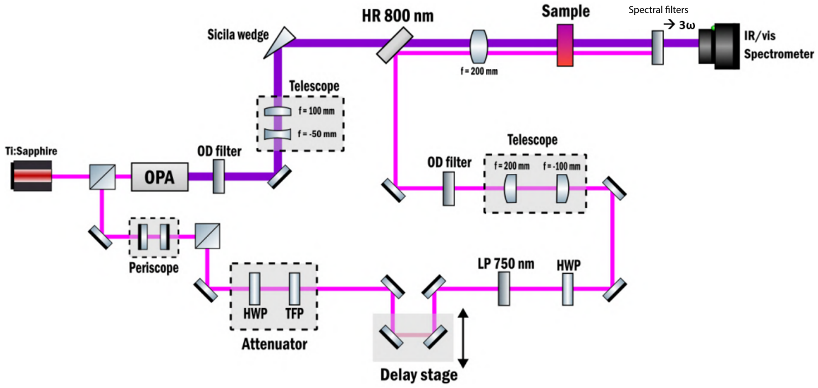

Figure 4.8: Schematic of the experimental setup that is used for transient deactivation measurements, shown in Fig. 4.3

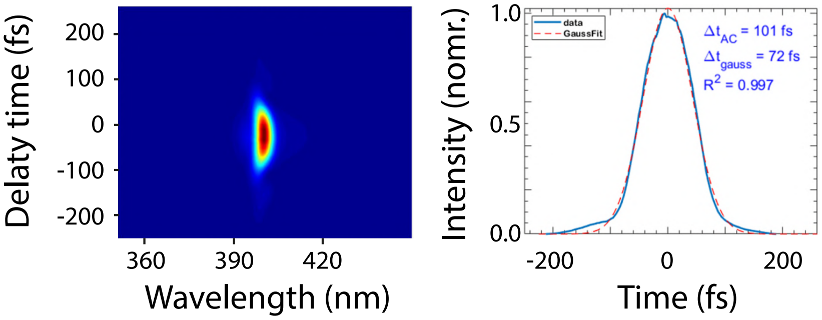

Figure 4.9: FROG and time trace measurements to characterize the deactivation spatial and temporal pulse width.

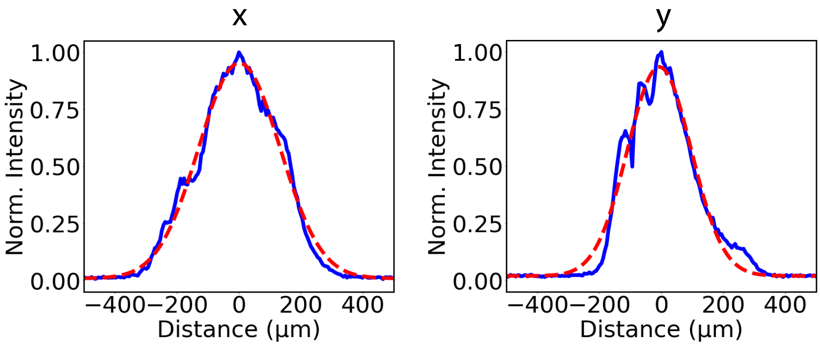

Figure 4.10: Beam profile measurements for the deactivation pulse. Experimental data is plotted as the blue solid line, and the Gaussian fit in red dashed line.

B.4 Generation pulse spectral measurement

The spectrum of the generation pulse was measured and a Gaussian with a FWHM $= 62$ nm was fitted to the spectrum. This relates to a (transform-limited) pulse of 51 fs. The non-Gaussian shape/roughness of the spectrum is an experimental artifact that comes from a problem with either the spectrometer or the fiber leading to the spectrometer.

C All transient TH suppression

This Appendix shows TH suppression timetraces for each measured pump fluence, with biexponential fits that correspond to the datapoints in Fig. 4.5. The pump fluences are given in each transient data plot. From around 4.2 mJ/cm^2 there is a second suppression peak visible around 5 ps delay time. We attribute this to reflection of the deactivation pulse within the substrate. The substrate thickness of 500 μm, translates to ~ 5 ps travel time. The second peak appears to grow more strongly than the 0 ps main suppression peak. We attribute this to the fact that in this regime the main suppression at 0 ps is already in the saturation regime.

In Fig. 4.5b), we plotted the fitted parameter values to the decay traces as decay rates, as these are directly extracted from the fit, and generally used to describe decay mechanisms. For researchers wishing to assess the decay times associated with the fast component, we also present a decay time vs pump fluence plot in Fig. 4.13.

Note that we did not include the slow decay time $1/\gamma_1$ in this plot, as these timescales vary much and are quite larger than $1/\gamma_2$.

D Polarization dependent absorbed power simulations

Here, we present the COMSOL simulations that are used to calculate absorbed power. Figure 4.14 presents the normalized electric near field, both represented with the same color scale. These simulations are performed at a single frequency as opposed to pulsed excitation, with incoming vacuum wavelength set to 800 nm. Dimensions are similar as described in the main text. The left (right) image is for vertical (horizontal)

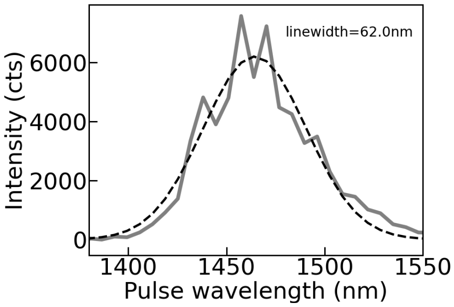

Figure 4.11: Generation pulse spectrum, where the experimental data is plotted as the grey solid line and the Gaussian fit to determine pulse width as the black dashed line.

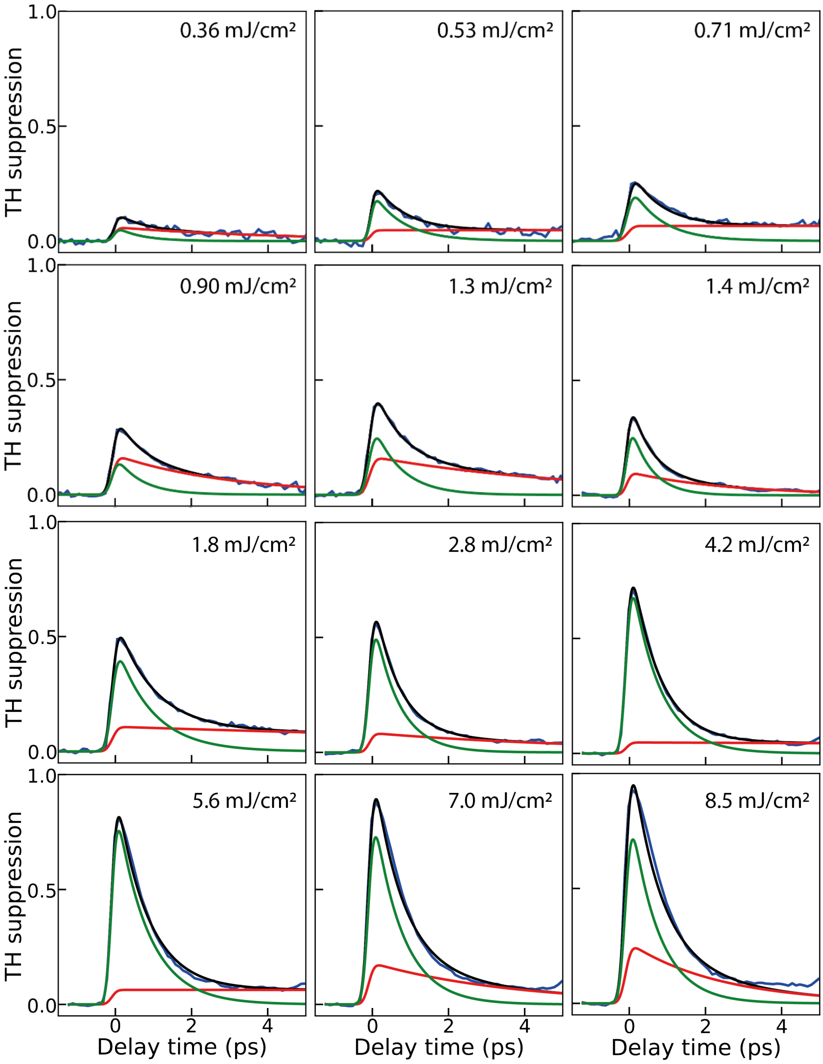

Figure 4.12: Transient TH suppression data for all measured pump fluences. The experimental data is plotted as the blue curve, the black curve presents the biexponential fit, whereas the green (red) lines present the fast (slow) decaying exponentials.

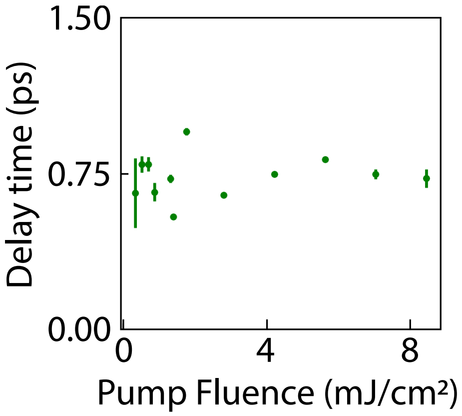

Figure 4.13: Decay time $1/\gamma_2$ as function of pump fluence, as extracted from the fast decay exponential fits in Fig. 4.12.

polarization. Absorbed power in the disk plus bar are 2.3% for the vertical polarization case and 3.4% for horizontal polarization.

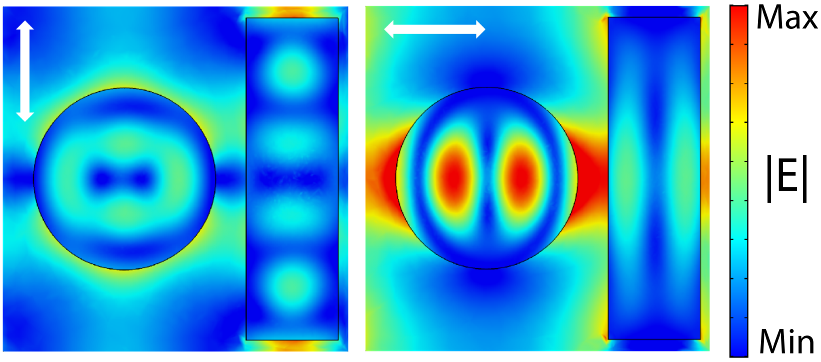

Figure 4.14: COMSOL simulation to calculate absorbed power. One meta-atom is simulated with periodic boundary conditions, and the color bar represents normalized electric field. The polarization of the field is given by the white arrow in the top left corner.

Chapter 5

All-Optical Nonlinear Real and Fourier Space Shaping with All-Dielectric Fano Resonant Metasurfaces

A main goal within the metasurface community is to develop dynamic, ultrafast tuning strategies for controlling beam profiles and directionality, especially in the ultraviolet regime. We present all-optical nonlinear beam shaping in both beam profile and its angular distribution. We use a digital mirror device within a pump-probe setup that allows spatial pump patterns of a visible light pulse to spatio-temporally coincide with an infrared probe pulse onto an all-dielectric Fano resonant metasurface. The infrared pulse is tuned near the Fano resonance to generate strong third harmonics, and the pump pulse locally deactivates harmonic generation due to excitation of carriers that broaden and blue-shift the resonance. The scattering of spatially periodic pump patterns convolve with the third-harmonic diffraction pattern, which generates satellite orders that evidence coherent emission and directional control. This work opens the door to ultra-fast precise control over harmonic beam profiles and directionality at generation stage.

5.1 Introduction

Nonlinear all-dielectric metasurfaces have enjoyed increased attention over the last decade [96, 111]. By harnessing the strong field enhancement inside meta-atom particles, metasurfaces can achieve harmonic generation with conversion efficiencies orders of magnitude higher than those of unstructured films, resulting in exceptionally bright emission [97], while eliminating phase-matching constraints [95, 223] and allowing tailorable wavefronts that are imprinted by nanostructure design [103]. These advantages have been demonstrated across a range of nonlinear processes, including second-harmonic generation (SHG) [224, 225], third-harmonic generation (THG) [102, 165], four-wave mixing (FWM) [226], and high-harmonic generation (HHG) [185, 203]. The required strong field enhancements are generally achieved by designing metasurfaces to support (interfering) Mie modes [52, 92]. High quality factor (Q) Fano resonances can arise from the interference between bright and dark modes [68]. These Fano resonances are shown to enhance nonlinear conversion efficiencies significantly [227]. Common approaches include coupling a dark mode to a bright mode via the near-field [97], or breaking symmetries to introduce radiative leakage into otherwise non-radiative, forbidden modes, a mechanism also referred to a quasi-bound states in the continuum (q-BIC) [99, 110, 165, 185].

A key feature of nonlinear metasurfaces is the diversity in functionality. Nonlinear effects, such as harmonic generation, add a plethora of possibilities to shape and control light emission [96]. This is especially relevant for imaging and microscopy using sources at UV wavelengths, where beam shaping by conventional linear optical components is difficult and often fails to perform effectively [228, 229]. Shaping the Fourier space–namely, controlling the directionality of light emission–has become a critical area of research [102, 230], next to the generation of orbital angular momentum beams [231], vector vortex beams [232] and structured light [233, 234]. Even though metasurfaces offer these diverse solutions, one main drawback is that metasurface function is fixed at fabrication. Over the past decade, tunable metasurfaces have been explored as a solution to counter the fixed functionality [235], for instance based on thermo-optical effects [236], electric biasing [237], liquid crystals [238], interferometric routing [182], and mechanical tuning [239]. However, tunability mechanisms tend to be slow and offer little room for desired wavelength ranges [191], such as for shaping UV beams. Consequently, there is significant ongoing effort within the metasurface community to develop dynamic tuning strategies capable of ultra-fast control over beam profiles and directionality, particularly in challenging and desired wavelength regimes.

In this Chapter, we present all-optical, ultra-fast, high-contrast nonlinear beam shaping in both real space (nonlinear source beam profile at the metasurface) and Fourier space (directionality). We use a digital mirror device (DMD) within a pump-probe setup that allows spatial patterns to be imprinted on a pumping (or switching) pulse, which spatiotemporally coincides with an infrared (IR) probe pulse onto an all-dielectric Fano resonant metasurface. The IR pulse is tuned near the Fano resonance to generate strong third harmonics (TH). The pump light (pulses chosen in the visible regime in this Chapter) projects an image of the DMD onto the metasurface. This pump pulse locally deactivates harmonic generation due to excitation of carriers that broaden and blue-shift the resonance, as hypothesized in the previous Chapter 4. Non-periodic pump patterns (such as alphabetic characters) are successfully imprinted onto the TH beam, demonstrating spatial wavefront control. Furthermore, we show, using spatially periodic and aperiodic pump patterns, that the angular distribution of TH emission convolves with the structured pumps spatial frequency components. The convolution produces satellite diffraction orders that evidence coherent emission and enable directional control. We found that the spatial programming of the pump is effective down to a minimum resolution of a single meta-atom, which is necessary to trigger harmonic deactivation. However, the deactivation mechanism features a transition region spanning about two meta-atoms. Only beyond this spatial threshold, full deactivation is reached, which we attribute to the intrinsically nonlocal nature of the Fano resonance. Furthermore, by controlling the time delay between the IR probe and visible pump pulse, we reveal the linear transient resonant response of the metasurface and the impact on THG conversion efficiency. Our findings demonstrate a powerful platform for all-optical dynamic beam shaping with nonlinear metasurfaces. As this method holds for any harmonic order, it opens the door to ultra-fast precise control over UV beam profiles and directionality at generation stage.

5.2 Concept of structured deactivation

The main concept of our experiment is visualized in Fig. 5.1. A 130 fs IR (1480 nm) pulse excites a Fano resonant metasurface, thereby generating third-harmonic emission. The metasurface consist of silicon meta-atoms comprising a disk adjacent to a bar on quartz. The disk-bar meta-atom structure has been studied extensively, also in the context of third and high-harmonic generation [97, 203]. The Fano resonance appears due to the interference of a bright electric dipole (ED) mode that is associated with the long axis of the bar, and a dark magnetic dipole (MD) mode pointing out of the plane that arises from circulating displacement currents in the disk. The strong field enhancement of the resonance allows for a large harmonic generation efficiency [93]. By means of a separate beam path, that passes through a delay stage and reflects from a digital mirror device (DMD), a 515 nm pump pulse projects a spatially programmable pump pattern onto the metasurface. As the pulse carries light with an energy that is larger than the bandgap of silicon, part of the pump light is absorbed by the nanoparticles, which excites carriers to the conduction

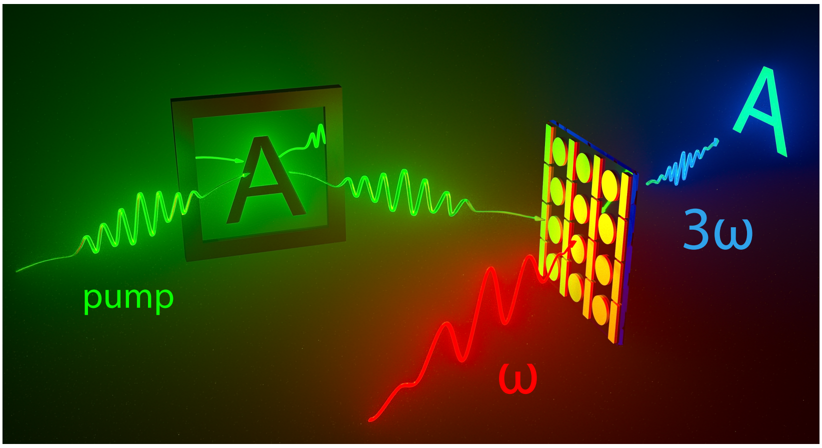

Figure 5.1: Illustration of our scheme to optically shape nonlinear beam profiles and control directionality. An IR pulse (ω, red) illuminates the sample to generate bright TH (3ω, blue) from a Fano resonant disk-bar metasurface. A second pulse (pump, green) reflects from a DMD to project a spatial pump pattern on the metasurface, that is negatively imprinted onto the TH emission profile.

band. The excited free carriers are associated with a refractive index change, which in turn blue-shift and broaden the resonance [240], reducing the THG efficiency (see Chapter 4). Since in this scenario the pump light absorption is associated with a reduction in THG generation, the negative of the pump pattern is transferred into the TH emission.

5.3 Transient dynamics

We fabricated disk-bar metasurfaces in polycrystalline silicon (135 nm thickness) that was evaporated onto fused quartz, and patterned with e-beam lithography. The meta-atoms are arranged in a square grid of 900 nm pitch, with each unit cell containing one disk of 240 nm radius adjacent to a 800×205 nm bar (scanning electron micrograph in the inset of Fig. 5.2a). Appendix A, of the previous Chapter 4, reports in detail on the nanofabrication procedure. Our experimental setup allows for exciting the metasurface with minimum angular spread, by using a long focal distance lens ($f = 200$ mm, Thorlabs) that focuses in the back focal-plane (BFP) of a microscope objective (Nikon 50×, NA 0.8), effectively de-magnifying our parallel IR beam to a radius of 20 μm. By using the rather broad bandwidth of the 130 fs pulse, linear infrared transmission measurements (presented in Fig. 5.2a), solid black) reveal a narrow Fano resonance with a quality factor $Q \simeq 500$, with light polarized along the long axis of the bar, measured by a grating based spectrometer equipped with an InGaAs detector (Avantes,

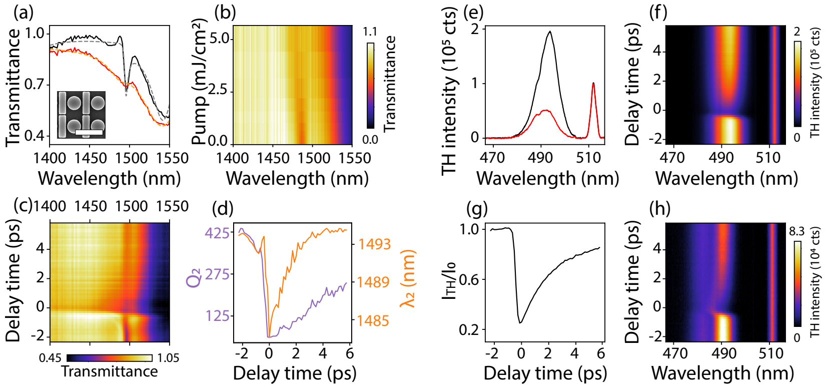

Figure 5.2: Transient Fano modulation and TH deactivation. a) Linear transmittance through a disk-bar metasurface (SEM inset, scale bar 1 μm). A Fano resonance of $Q \simeq 500$ appears at 1490 nm that is apparent without pumping (solid black) and disappears with pump (solid red), at time t_0 and pump fluence = 2.52 mJ/cm^2. The dashed curves are coupled oscillator fits to the data in order to extract Q and resonant wavelength. b) Transmittance as function of pump fluence on the vertical axis. c) Transient transmittance at pump fluence 2.52 mJ/cm^2, with pulse delay time on the vertical axis. d) Quality factor of the Fano Q_2 (purple) and the resonant wavelength λ_2 (orange). e) Emitted TH spectrum at $t < t_0$ (black) and at $t = t_0$ (red), showing a clear reduction of THG efficiency. Residual pump light that is not filtered out by the notch filter is visible as the peak near 515 nm. f) Transient TH spectrum for a probe wavelength of $\lambda = 1480$ nm. g) TH deactivation obtained by spectrally integrating the TH spectrum from 490 to 500 nm. h) Transient TH spectrum for a non-resonant probe pulse of wavelength $\lambda = 1440$ nm, showing THG enhancement at the Fano resonance (centered at 1490 nm. Pumping visibly induces blueshift at $t = 0$ps.

AvaSpec-NIR256/512-1.7-HSC-EVO). The bright ED mode is visible in the transmission spectrum (Fig. 5.2a) as the broad dip near 1550 nm and the coupled dark MD mode as the narrow dip near 1490 nm.

5.3.1 Resonance response to pump excitation

A 515 nm pump pulse (pulse length 130 fs, circa 3 nm bandwidth) passes through a delay stage (Newport, power supply: DL-PS, delay line kit: DL-BKIT2U-S-M, stage DL125), in double-pass setup, to precisely control time delay between 515 nm pump and IR probe. The pump projects a 50× demagnified image ($f = 200$ mm lens, Thorlabs, focuses in the BFP of the 50×, NA 0.8 microscope objective) of the DMD (Texas Instruments, DLP LightCrafter Single DLPC900 EVM, controller: DLPC900, chip: DLP6500) onto our disk-bar metasurface. The pixel size of the DMD is 7.56 μm, or 151 nm in the sample plane, which is about 2.1 pixels per diffraction limited length of $\lambda/2\text{NA} \simeq 322$ nm. The pump and probe beams are combined right before the objective via a beamsplitter (Thorlabs, BS025). With all pixels on the DMD set to reflective, it effectively functions as a mirror, so that the

Gaussian beam profile of the pump beam is projected on the metasurface. In all experiments we maintain an operating repetition rate of 1 MHz. Figure 5.2a) shows a transmittance spectrum (red solid line) with pump and probe pulses overlapping in time and space, at a pump fluence 2.52 mJ/cm^2. Here the DMD is set to operate as a mirror, and we have precisely tuned the pump power and delay time for overlap. In this switched configuration, no trace of the Fano resonance is evident. In the previous Chapter 4, we hypothesized and validated via simulations, based on earlier work on ultrafast switching of silicon photonic structures, that the pump light is directly absorbed in the silicon. This absorption leads to free carriers that modulate the refractive index, which we described with a Drude model. In this picture, one expects a reduction of the real part of the refractive index n, and an increase in the imaginary part k. According to electromagnetic simulations, this refractive index change in turn causes a blue-shift of the metasurface resonances, accompanied by a deterioration of the quality factors due to free carrier absorption at infrared wavelengths. Recent work shows similar blue-shifting optical resonance control via light-induced pumping [241]. The experiment presented in Fig. 5.2b) examines the dependence of this resonance modulation as a function of pump fluence, with the delay time fixed at t_0, measured by an optical spectrum analyzer (Thorlabs, OSA202C). Temporal overlap t_0 in this work was determined by maximum harmonic deactivation (see discussion below of the THG signal). The observed broadening and shift in the linear IR transmission of both the narrow and broad resonant modes confirm our hypothesis, consistent with direct absorption of the pump pulse and subsequent carrier excitation.

5.3.2 Transient response of resonance

Having confirmed the pump-induced resonance shift and broadening at temporal overlap, we next investigate the transient dynamics of the metasurface response. Transient changes in the resonant behavior of the metasurface are studied by keeping the pump fluence fixed, while scanning over delay time. Figure 5.2c) presents a time trace of 8 picoseconds in steps of 133.3 fs, at pump fluence 2.52 mJ/cm^2, captured with the same spectrometer as Fig. 5.2a). At the onset of t_0, a very strong broadening and shift is observed in the transmittance spectrum. This effect is maintained for at least a few picoseconds, likely determined by thermalization and carrier recombination times in the nanostructured polycrystalline silicon, next to carrier diffusion from hotspots to the rest of the nanoparticles [143, 242, 243]. The long lasting dynamics evidence the absorptive nature of the effect, rather than nonlinear effects that solely occur instantaneously [95]. The transient blue-shifting behavior of the resonance under pumping is similarly observed by recent work [241]. Ultrafast dynamics, and even enhancement, are visible before the onset of t_0, which might be due to the long lifetime of the Fano resonance. Transient IR probe spectra are found in the Appendix A, as well as the normalized IR transmittance ratio T/T_0, where T_0 is the transmittance spectrum at $t = -2$ ps to highlight pump-induced changes. The shift and broadening of the resonance is further investigated by fitting a coupled oscillator function (example fits in Fig 5.2a), dashed lines) to the transmittance spectrum at each time step. The time trace of the fitted quality factor Q_2 and resonant wavelength λ_2 of the dark mode is presented in Fig. 5.2d). The quality factor is indeed greatly reduced, while the resonant wavelength blue-shifts at time t_0, and recovers over picoseconds.

5.3.3 Transient response of THG

Panels e-h) of Fig. 5.2 present transient TH deactivation measurements. The IR probe pulse is centered near the Fano resonance to increase THG conversion efficiency. TH signal is collected in reflection, where it reflects off a dichroic mirror (550 nm, Edmund Optics) right after the microscope objective, passes through a 1:1 telescope (Thorlabs 2x $f = 150$ mm), a notch filter (Thorlabs NF514-17), and short-pass filter (Thorlabs FESH0500) to remove the pump pulse. Afterwards, it is focused on the slit of a grating based spectrometer (Andor Shamrock 163i, 163 mm focal length, 300 lines/mm, 25 μm slit width, with a CMOS camera Ximea MC124MG-SY-UB) to measure TH spectra, or onto a set of two cameras: one images the real-space plane of the TH emission from the metasurface (Basler acA 1920-40 μm), while the other uses an additional lens ($f = 200$ mm, Thorlabs AC254-200-AB) that focuses in the BFP of the objective to image the Fourier-space plane to study the angular distribution of the TH emission (Thorlabs CS2100M-USB). Appendix B presents an overview of the experimental setup. Figure 5.2e) presents two TH spectra, where the black spectrum shows the regular TH spectrum without pump and the red spectrum shows the TH spectrum under pumping at t_0 (pump fluence 2.52 mJ/cm^2). The THG efficiency is greatly reduced due to the resonance being pumped out of spectral overlap with the IR probe pulse and the introduced loss to the resonance by excited free carrier absorption. We scan the same time delay range as Fig. 5.2c), to study the transient TH deactivation. Figure 5.2f) shows almost 80% deactivation of THG at t_0, slowly recovering the signal over picoseconds. By integrating over a narrow spectral band (490-500 nm), we study the total dynamic TH suppression and the associated timescales (Fig. 5.2g). This relatively large modulation is consistent with work presented in the previous Chapter 4, which reported even higher modulation strengths. In general, the modulation strength can be optimized by adjusting parameters such as pump fluence, pulse tuning and length, and polarization. However, such optimization is not the topic of the present work, and we consider a modulation depth of approximately 80% sufficient for our spatial deactivation purposes. To further evidence the dominant contribution of the Fano resonance to the THG efficiency, we chose an IR pulse that is spectrally blue-shifted (centered at ∼1450 nm) from the Fano resonance (∼1490 nm). Figure 5.2h) shows a TH spectrum time trace where two key observations can be made. First, even though the central wavelength of the IR pulse is at 1450 nm (= 485 nm × 3 nm), strongest THG occurs in the spectral tail of the pulse near the Fano resonance at 496 nm (496 nm × 3= 1490 nm) [165, 190]. Second, at time zero, the peak of the THG is blue-shifted and is even enhanced for a small bandwidth, before slowly returning to its original wavelength. These two observations further evidence the spectral overlap dependence and the effect of the blue-shift of the resonance on the THG efficiency.

5.4 TH real-space shaping

The previous measurements reveal the linear and nonlinear dynamic metasurface response to uniform excitation. Next, we explore how spatial structuring of the pump field affects the nonlinear emission. We use the DMD to project binary spatial patterns, *i.e.*, fully black and white intensity patterns without intermediate gray levels. These binary patterns impose a strong spatial modulation on the pump intensity, which through absorption in the metasurface material, is expected to induce local variations in the meta-atom resonance,

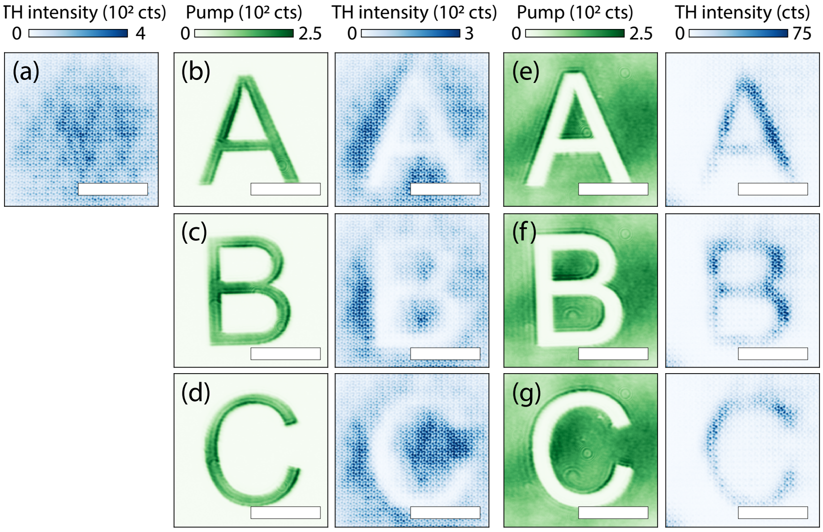

Figure 5.3: Nonlinear real-space shaping. Obtained TH signal is depicted in blue, while pump patterns are depicted in green, with color bars above the plots. The scale bars depict 10 μm. a) Measured TH spot without pump pulse. b) Pump pulse pattern depicting an 'A' on the left, generated a TH spot with the letter subtracted on the right. c) Similar results for B and d) for C. e) Pump pulse pattern showing the inverse of (b) on the left, which generates an A in TH signal, with f) B and g) C.

enabling control over the spatial profile of the nonlinear emission. Figure 5.3 shows six examples of dynamically shaped harmonic beams, measured using real-space microscopy of the sample at the TH wavelength. For reference, Fig. 5.3a) represents the spatial distribution of THG for a fully reflective DMD (no pattern projected, camera integration time 200 ms). Even though the TH real-space images are slightly out of focus on the camera, the individual unit cells are visible. This results from the fact that although the metasurface is sub-diffractive at the fundamental wavelength (1480 nm), the unit cell pitch (900 nm) is well within the diffraction limit for the THG wavelength (490 nm light, NA 0.8, in air). Figures 5.3b–d) display the pump field on the left in green and the corresponding third-harmonic real-space image in blue on the right, at pump fluence 0.63 mJ/cm^2. In each case, the pump field is shaped as the letter A, B, or C, resulting in a TH signal that appears as a bright spot with the respective letter subtracted. Figures 5.3e-g) present the results for pumping the inverse of the letters A, B, C, which are displayed on the left side, with the corresponding TH images images on the right, at pump fluence 0.32 mJ/cm^2. In all TH real-space images, a gradient of TH deactivation is visible from the left bottom to the top right, which could be due to a small angle of incidence difference between probe and pump pulse, resulting in non-parallel wavefronts, or due to a spatial chirp that introduces a spatially dependent t_0. There is a notable width difference of the letters in the deactivated (Figs. 5.3b-d) and activated (Figs. 5.3e-g) cases. This raises the question of the spatial extent of (de)activation, which will be examined in the spatial resolution experiments, discussed in 5.6.

5.5 TH Fourier-space shaping

A crucial feature of nonlinear metasurfaces is that the harmonic generation is coherent, meaning that spatial structuring in the near field of the sample should also immediately impact the angular distribution of emitted third-harmonic light. As such, we envision our method of all-optical spatial structuring to also present a method for all-optical structuring of directionality. This capability is not immediately evident from the real-space images: real-space amplitude demodulation by a deactivating pulse can, in principle, be replicated using incoherent sources such as fluorescence, but in that case the angular distribution remains unaffected. We demonstrate nonlinear Fourier-space shaping in Fig. 5.4. The pump fluence in this measurement set was kept at an average of 5 mJ/cm^2. A plethora of pump patterns were used to study the angular emission, including hexagonal lattices, 2D grids and hyperuniform patterns. Without pumping, we expect a square TH diffraction pattern that consists of discrete nonlinear gratings orders, i.e. discrete points at angles that derive from the TH wavelength λ_{TH} and metasurface pitch p through θ_m =arcsin($\frac{-m\lambda}{p}$) $= 0.58k_0$, with m the order ±1. A Fourier image

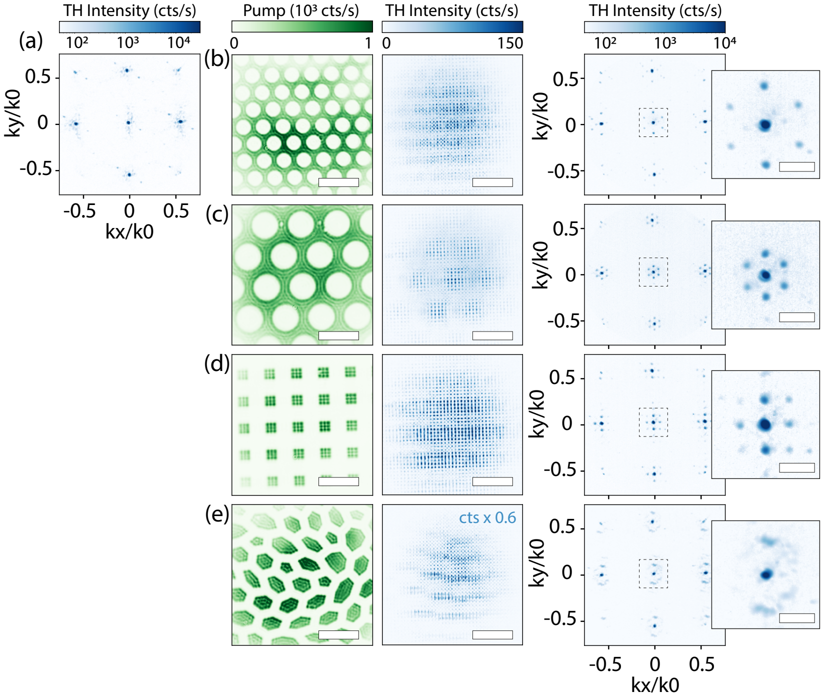

Figure 5.4: Nonlinear Fourier-space shaping. Scale bar depicts 10 μm. a) Measured Fourier-space pattern without pump. b–e) The spatial pump patterns are shown on the left in green, with the accompanying produced TH real (Fourier) space image in the middle (on the right). On the far right is an enlarged Fourier space image of the dashed area ($|k_{x,y}/k_0| < 0.155$) to highlight changes around k_0, with scale-bar $k_{x,y}/k_0 = 0.1$. The spatial TH deactivation is visible in the real-space image, which produces hexagonal (b,c) or square (d) satellite orders around the metasurface diffracted orders. The hyperuniform pattern (e) produces a scattered ring around all diffraction orders.

confirming this intuition is displayed in Fig. 5.4a). In the pumped cases, we expect a similar diffraction pattern, convolved with the Fourier transform of the (photo-negative) of the pump pattern. This follows the logic of X-ray diffraction and antenna array theory, translated to the case of nonlinear sources. Following this logic, the near field nonlinear source distribution is written as the product of the source distribution (a lattice with the metasurface pitch) in absence of the pump, multiplied by an amplitude mask induced by the switching pattern. Consequently, the far field is expected to be the convolution of the lattice radiation pattern (grating orders), and the transform of the amplitude mask. By way of example, Fig. 5.4b) shows a hexagonal hole pump pattern on the left, its generated TH real-space image in the middle, and the Fourier-space angular emission profile on the right in log-scale, to highlight subtle low-intensity differences. Compared to the reference case, hexagonal satellite orders are generated around each diffraction order. In Fig. 5.4c), the hexagonal directionality is generated at a smaller reciprocal lattice vector, as the pump pattern (shown on the left) pitch is increased. The 2D square grid, presented in Fig. 5.4d), reveals square satellite diffraction orders. Furthermore, this is not restricted to periodic amplitude masks. As example, in Fig. 5.4e) we use an amplitude mask of patches and veins that is a so-called ‘hyperuniform’ pattern: its Fourier transform presents a ring in Fourier space [244]. Indeed, the THG shows isotropic scattering rings around the grating orders. The hyperuniform pattern was provided by Alex Lambertz. The set of measurements presented in Fig. 5.4 clearly shows the wide variety of shaping nonlinear directional emission by spatial deactivation with a pump.

5.6 Spatial extent of harmonic deactivation

Finally, we assess some of the limits of this approach. In particular, we examine the spatial extent, or, spatial resolution of this form of harmonic deactivation. Note, for example, the notable width difference of the letters in Fig. 5.3. On the one hand, one might argue that our DMD and pump light combination has the resolution to engage (sub-)single metasurface unit cells. On the other hand, Fano-resonances in metasurfaces are nonlocal, suggesting that effectively the spatial resolution is limited to a few unit-cells. To address this question experimentally, we produce a set of pump patterns that include a circular window or a circular spot, with variable radius, and a periodic 2D square checkerboard pattern with variable gap linewidth. The goal of this exercise is to extract an estimate for the minimum amount of meta-atoms necessary for harmonic generation or deactivation.

5.6.1 Real-space analysis

Figure 5.5a) shows the circular window (spot) pump pattern on the left (right) side, at radius $r = 2.3$ μm. In this measurement set, the pump fluence was kept at an average of 4.41 mJ/cm^2, and the time at t_0. Examples of produced TH real-space patterns are displayed in Fig. 5.5b), for the window (spot) on the left (right) side, at $r = 3.8$ μm. We study the TH brightness by integration of the counts inside the pump area, which is indicated by the black dashed circle in Fig. 5.5b). The square root of the integrated counts as function of pump radius is presented in Fig. 5.5c). At $r > 0.9$ μm (indicated by the vertical dashed line at meta-atom 2), the square of the TH integrated intensity for both the window or spot logically follows a straight line, as the TH counts grow as the square of the area. The slope of the TH light as function of pump radius is determined by deactivation (spot, purple) or no deactivation (window, orange). At values $r < 0.45$ μm (indicated by the area left of the vertical dashed

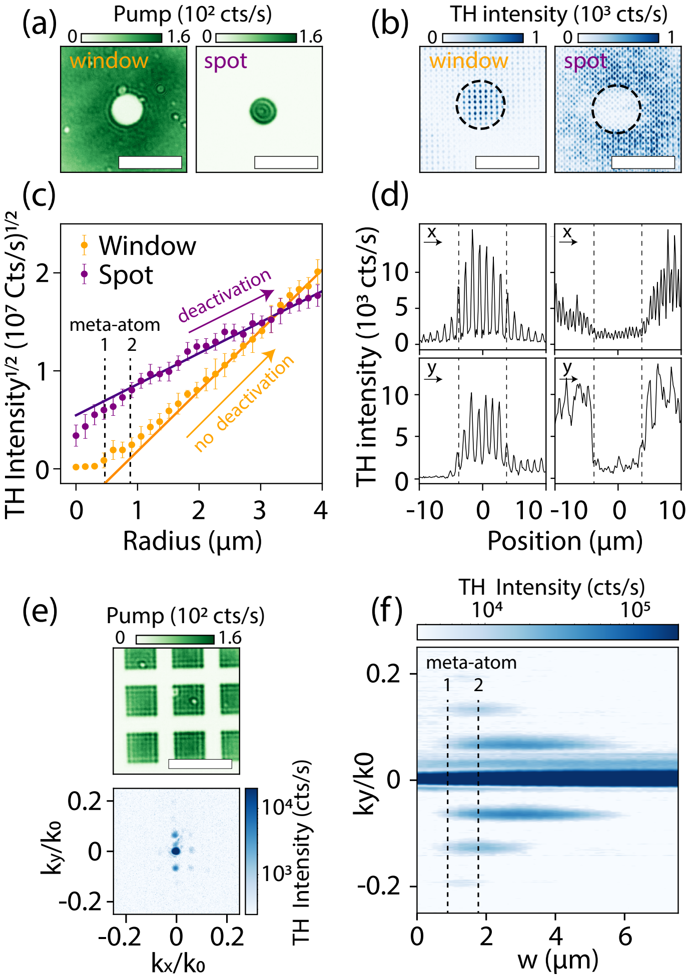

Figure 5.5: Spatial TH deactivation extent study. a) Pump image of the window (spot) at radius $r = 2.3$ μm on the left (right), scale bare depicts 10 μm. b) TH realspace images for window (spot) on the left (right) at radius $r = 3.8$ μm, with integration boundary indicated by the dashed black circle. c) The square of the TH intensity in the integration area for window (orange markers) and spot (purple markers) as a function of pump radius, with linear fits to the region $r > 1.5$ μm (solid lines). The vertical dashed lines indicates where the diameter spans 1 and 2 meta-atoms. d) TH intensity cross-cuts summed over a band of 3 μm in the center of the window (spot) on the left (right), where the horizontal (vertical) direction is on the top (bottom). Dashed vertical lines indicate the pump area region of $r = 3.8$ μm. e) (top) 2D checkerboard pump pattern (at gap linewidth $w = 2.3$ μm, (bottom) generates square satellite orders around the metasurface diffraction orders in TH Fourier space (image taken at gap linewidth $w = 3.8$ μm). f) Vertical TH Fourier cross-cut summed over a small band of $-0.008 < k_x < 0.008$ as a function of pump checkerboard gap linewidth w. Dashed vertical lines indicate where w spans 1 and 2 meta-atoms.

line called meta-atom 1), the TH intensity within the window area (orange markers) increases only slowly, indicating that the radius is insufficient to activate harmonic generation. In the same range, the integrated TH intensity in the spot area (purple markers) exhibits a steeper increase compared to the region beyond $r > 0.9$ μm. A clear change of slope in integrated TH intensity for both pump patterns is observed between $r = 0.45$ μm and $r = 0.9$ μm. These observations indicate that a minimum of >1 meta-atom ($r = 0.45$ μm, at metasurface pitch $p_m = 900$ nm) is necessary for resonance modification by pumping, whereas the nonlocal nature of the resonance is maintained at more than 2 meta-atoms. This result is further supported by analyzing a cross-cut (transversely summed over 3 μm) of the TH real-space image, presented in Fig.5.5d), which reveals the number of unit cells involved in the transition from the activated to the deactivated region. Especially in the vertical cross-cuts, displayed in the bottom two graphs, a transition is visible of 1-2 unit-cells.

5.6.2 Fourier-space analysis

In addition to the real-space spatial extent analysis, we also examine the system's behavior in Fourier space, providing complementary insight into its momentum-resolved characteristics. Figure 5.5e) shows the periodic 2D checkerboard pump (top, example image at $w = 2.3$ μm) and TH Fourier image (bottom, at $w = 3.9$ μm). We focus on the satellite diffraction orders produced around k_0. Figure 5.5f) tracks a vertical cross-cut of the TH intensity (summed over a band $-0.008 < k_x < 0.008$), as a function of the gap linewidth between checkerboard blocks w. No satellite orders are created below pattern line widths $w < 0.9$ μm (indicated by vertical dashed line meta-atom 1), whereas the TH intensity starts leaking into the satellite diffraction orders at gap linewidths of $w > 0.9$ μm, which is consistent with the previous estimate that at least a single meta-atom is required to (de)activate harmonic generation. To confirm that this observation is really attributable to the modulation mechanism, and not to a property of linear diffraction theory, in Appendix C we show calculated diffraction efficiencies according to linear diffraction theory for binary grids (*i.e.*, supposing that the modulation has sub-single meta-atom resolution). In this case, satellite orders already appear at $w < 0.9$ μm. We can thus conclude from our observation that the nonlocal nature of the Fano resonance places a physical limit on the modulation resolution. Based on this spatial extent analysis, we conclude that at least one meta-atom is required to initiate TH deactivation (leading to the minimum resolution of a single meta-atom), with a transition region to complete deactivation that spans 2 meta-atoms.

5.7 Conclusion

In summary, we presented all-optical nonlinear beam shaping both in real-space beam profile and its Fourier-space angular distribution. We achieved this demonstration via pumping a Fano resonant all-dielectric metasurface with a visible pump pulse that broadens and blue-shifts the resonance due to photon absorption induced excited carriers, thereby deactivating harmonic generation from an IR probe pulse tuned to the Fano resonance. By controlling the time delay between the probe and pump pulse, we revealed the transient resonant response and the impact on the THG. We spatially structured the pump pulse via a DMD to locally deactivate harmonic generation, and presented nonlinear real- and Fourier-space shaping, evidencing the coherent nature of TH emission. Furthermore, we found that the spatial pump is effective down to a minimum resolution of a single meta-atom, which is necessary to trigger harmonic generation or deactivation. The deactivation mechanism exhibits a transition region spanning 2 meta-atoms, beyond which complete deactivation is achieved.

To better understand the spatial extent of resonance shaping, one could perform hyperspectral mapping of the metasurface, revealing the local optical response as a function of pumping. When carried out at the level of a single meta-atom (or even sub-unit-cell resolution) this approach could uncover the true nature of resonance modulation at the nanoscale. We emphasize that our nonlinear beam shaping approach holds for any harmonic order. This fact brings UV beam shaping within reach, especially as the mechanisms of nonlinear emission from solids continue to be better understood [122, 205, 209]. Given the limited availability of conventional UV optics, the ability to shape the beam profile and control the emission direction at generation stage could be a game-changer.

Appendices

A Transient IR probe spectra

For researchers interested in the complete IR probe transmission data, Fig. 5.6a) displays the IR transmission spectra (x-axis) as a function of pumpprobe time delay (y-axis). This probe signal corresponds to the same measurement shown in Fig. 5.2. Additionally, Fig. 5.6b) presents the transient IR transmittance, plotted as the normalized ratio T/T_0, where T_0 is the transmittance spectrum at $t = -2$ ps, to highlight changes.

As an example, Fig. 5.7 presents IR probe reference (*i.e.*, the IR excitation pulse) and IR probe spectrum and corresponding transmittance, defined as the ratio of IR probe to reference, for time delays: $\Delta t = -2$ ps (before temporal overlap) and at $\Delta t = 0$ ps (at temporal overlap).

B Experimental setup for structured TH deactivation

The components within the experimental setup are described in detail in Section 5.3.1; here, we provide a schematic illustration for clarity (Fig. 5.8). The colors in the schematic are used symbolically to ease the understanding and reflect the real colors in the experiment. The IR pulse generates TH light in the metasurface, which, due to the reflective setup, retraces the same optical path (indicated in orange) back toward the dichroic mirror. The dichroic mirror then guides the TH signal into the collection path (shown in blue). In practice, the 515 nm pump pulse is also reflected from the metasurface and follows the same return path as the TH signal, but it is blocked by a notch filter, which represented in the schematic as the '515 filter'.

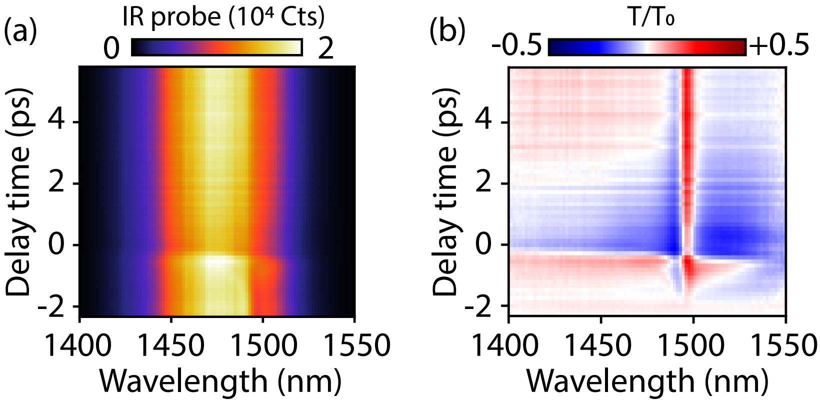

Figure 5.6: a) Transient IR probe spectra (x-axis) for a delay time trace (y-axis). b) Normalized IR transmittance ratio T/T_0, where T_0 is the transmittance spectrum at $t = -2$ ps.

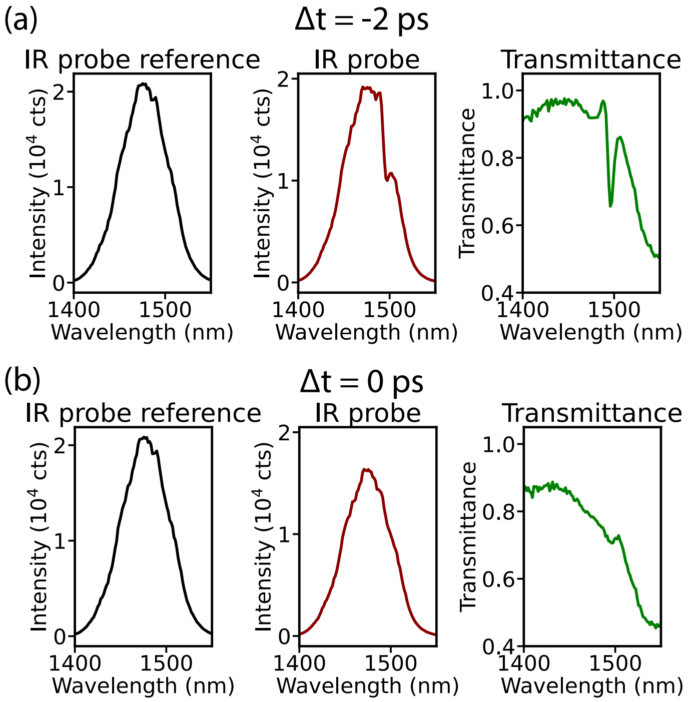

Figure 5.7: Example cross-cuts or the IR excitation pulse (left), IR transmission (middle) and IR transmittance before temporal overlap at delay time $\Delta t = -2$ ps (a) and at overlap $\Delta t = 0$ ps (b).

C Diffraction efficiency calculations

To assess whether the reduced diffraction efficiency observed below a single meta-atom in the experiment (Fig. 5.5f) arises from limitations in deactivation capability or is intrinsic to the nature of convolved 2D grids, we perform a numerical calculation. In this approach, all quantities are redefined in terms of discrete "pixels", meaning that the full analysis presents discrete Fourier transforms (which might lead to artifacts). Since the DMD generates a series of 2D grid patterns with varying gap linewidths, we interpret these gap widths as integer pixel values. All spatial dimensions are subsequently converted to this pixel-based scale. Considering the demagnification of the pump pattern onto the sample (one DMD pixel corresponds to 151 nm in the metasurface plane), the effective number of pixels per metasurface pitch is calculated as 955 [nm] / 151 [nm/pixel] $\sim$ 6 pixels.

Starting from a 2D grid with a lattice spacing of 6 pixels, we impose a circular Gaussian mask to mimic the spatial Gaussian profile of the excitation beam, shown in Fig. S3.1a).

The discrete Fourier transform (DFT) of the metasurface lattice yields discrete diffraction orders at similar k-values as the experiment (Fig. 5.9b). The second grid, corresponding to the block pattern, is a binary mask with variable gap linewidth w

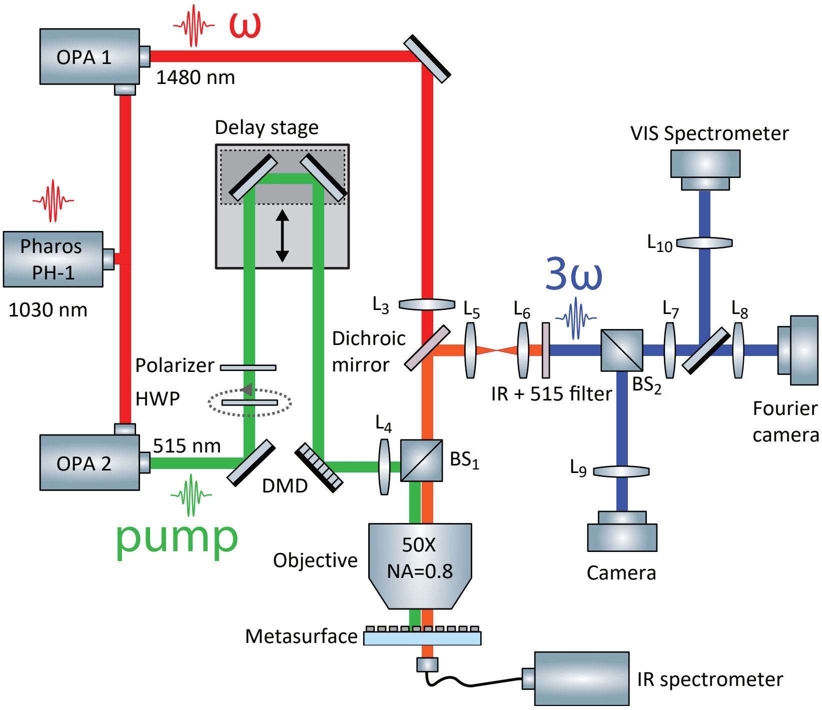

Figure 5.8: Schematic of the experimental setup used for structured TH deactivation experiment. The details of the components are described in Section 5.3.1

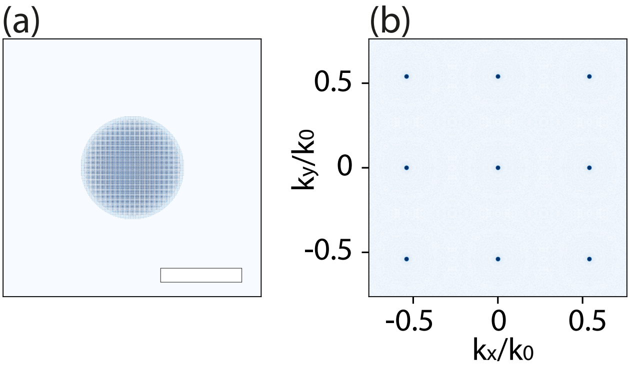

Figure 5.9: Assumed real-space 2D grid with metasurface pitch. b) Discrete Fourier transform yields diffraction orders.

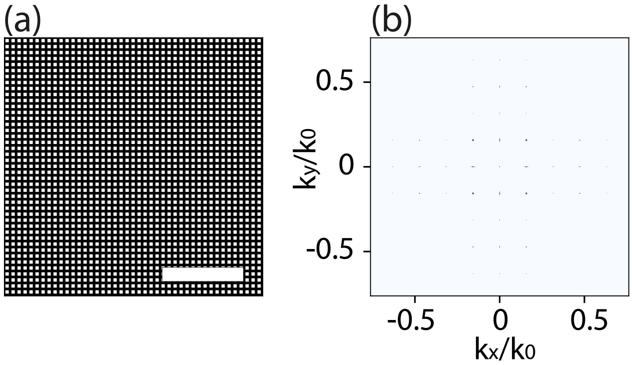

Figure 5.10: Binary pump grid used in the experiment for projection on the DMD, and in the calculation as input for a DFT to obtain the Fourier pattern, which is presented in (b).

ranging from 0 to 50 pixels (Fig. 5.10a, example at w = 22 pixels), that represents the real space DMD pump pattern. Its Fourier transform (Fig. 5.10b) is then multiplied with the Fourier pattern of the metasurface lattice to produce the convolved diffraction pattern (Fig. 5.11a).

Following the same procedure as in the main text, we sum over a small band in k_x and plot k_y versus gap linewidth w (Fig. 5.11b).

Finally, we sum the intensity in each satellite diffraction orders (both of experimental data as numerical calculation) to compare the onset of TH deactivation, presented in Fig. 5.12. The experimental data show that TH signal in the satellite orders emerges only once the deactivation area reaches a single meta-atom, while the calculated inten-

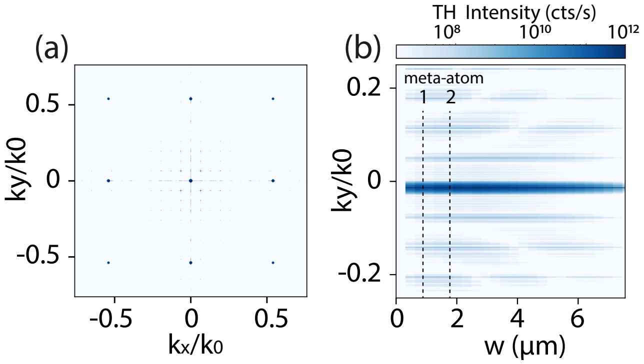

Figure 5.11: Calculated Fourier space of the convolution between the metasurface emission and the binary pump grid, revealing clear discrete diffraction orders as well as satellite features arising from the spatial modulation. b) Calculation of k_y as a function of gap linewidth w, analogous to the experimental data shown in Fig. 5.5f). In the numerical calculation, TH intensity already flows into the diffracted satellite orders below 1 meta-atom.

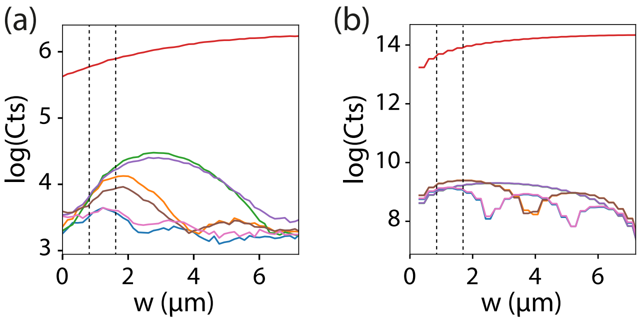

Figure 5.12: Summed intensities in the diffracted satellite orders (red: 0, green/purple: +1/-1, orange/brown: +2/-2, pink/blue: +3/-3) for experiment (a) and calculation (b). Where almost no TH intensity flows in the diffracted satellite orders below 1 meta-atom experimentally, the calculation shows a steady increase well below 1 meta-atom.

sity ramps up from $w = 0$ μm. This evidences that a minimum deactivation resolution of one meta-atom is experimentally required, in contrast to the calculation, where gradual modulation is possible even below this scale.

Summary

Dynamic nonlinear light control and metrology with resonant metasurfaces

Humanity's pursuit of progress is etched into our innovative desire to make things faster, smaller and more efficient. Few endeavors reflect this ambition more clearly than the ever-advancing world of microelectronic chips. Enabled by extreme ultraviolet lithography, these remarkable miniaturization advancements lay at the basis of virtually all modern digital infrastructure, from smartphones and autonomous systems to artificial intelligence hardware and cloud data centers. An essential step in manufacturing such intricate nanostructures is the precise inspection of nanoscale features, a process known as metrology. Advanced nanolithography demands equally advanced metrology to guarantee device fidelity. As device dimensions shrink, extracting metrology parameters becomes increasingly challenging, since conventional optical metrology is fundamentally bound by Abbes diffraction limit.

Nonlinear emission from resonant optical metasurfaces offers a compelling direction to meet this challenge. Metasurfaces are carefully engineered surfaces that comprising arrays of subwavelength nanostructures (often referred to as meta-atoms) arranged in (a)periodic patterns. These metasurfaces are designed to manipulate light with a degree of control not achievable with conventional optics. Strong resonant effects, such as Fano resonances, can be exploited to enhance contrast in linear metrology. Adding to this foundation, resonant metasurfaces have emerged as one of the most powerful platforms for enhancing nonlinear optical effects, where the interaction of intense light fields with nanostructured surfaces generates new frequencies with shorter wavelengths (harmonic generation). Nonlinear optical metrology presents us two key advantages. First, the generated harmonic wavelengths are (much) shorter than the fundamental. Shorter wavelengths are still subject to Abbes diffraction limit, yet shifting to a smaller scale logically enables improved resolution. Second, the nonlinear polarization scales with a power of the electric near field. This means that small changes in local geometry or fundamental near-field distribution can lead to disproportionately large variations in the emitted harmonic far-field intensity.

The work presented in this Thesis is inspired by the desire to establish the link between semiconductor metrology and nonlinear optical control in nanophotonic structures. The approach of using nonlinear light for metrology presents us two distinct scenarios. In the first, the metasurface serves as the metrology target itself: its coherent harmonic generation provides increased metrology sensitivity due to power-law dependence of the nonlinear polarization. In this picture, tiny geometrical variations translate into large changes in the nonlinear emission, that can directly be related to metrology information of the scattering target. In the second, metasurfaces are used to

develop compact (extreme) ultraviolet light sources with precisely tailored wavefronts that are in turn used to interrogate integrated circuits for more advanced metrology information.

Through this work, we aim to lay the foundation for bringing the rich physics of nonlinear diffractive metasurfaces into the realm of applied, high-precision semiconductor metrology. We set out on a scientific adventure to understand the mechanisms behind nonlinear emission from resonant metasurfaces. To achieve this future goal, we must answer a set of fundamental questions. For scenario 1: How can resonances be harnessed for linear metrology? And, How does the nonlinear response of Fano resonances change under excitations of ultra-fast light pulses? For scenario 2, we explore: How can a metasurface function as a dynamic nonlinear light source with precisely tailored wavefronts?

In **Chapter 2**, we focus our initial effort to understanding how resonant effects can be employed to enhance linear metrology. We demonstrate critical dimension metrology using quasi-bound state in the continuum resonant metasurfaces. The key to our work is that these resonances produce sharp Fano lineshapes that have the advantageous property of being extremely sensitive to minute geometrical changes of the meta-atom architecture. We show a creative approach that relies on linear transmission measurements of metrology targets based on a dielectric disk-hole metasurface design, where the design of the void (or hole) is structurally filled with the nanoscale features under interrogation. In this Chapter, we present both experimental and simulated results for various structure-in-void metasurface designs, and attribute the spectral change of the resonance to the sensitivity to an effective refractive index in the void of the meta-atom, which is directly linked to the critical dimension. This approach could be directly implemented in current semiconductor production lines by filling the void in the metasurface design with standard optical scatterometry targets, thereby significantly enhancing optical contrast.

Chapter 3 embarks on a first endeavor to study nonlinear emission from Fano resonant metasurfaces for varying excitation pulses. We study third-harmonic generation from a similar disk-hole quasi-bound state in the continuum metasurface, opening the door for nonlinear optical metrology. In this chapter, we investigate how modal interference between bright and dark modes, together with pulse characteristics, shape the nonlinear response and we demonstrate that metasurface nonlinearity is inherently coupled to its driving field. We observe asymmetries in third-harmonic diffraction and non-Gaussian spectral profiles that vary strongly near the fundamental Fano resonance. A coupled-oscillator model explains these observations by describing the interplay of the driving field to the modal nonlinear response, offering a predictive route to optimize tunable third-harmonic diffraction. The results presented in this Chapter establish pulse-engineered metasurfaces as a powerful platform for nonlinear wavefront shaping and frequency conversion applications. Furthermore, it paves the way for nonlinear optical metrology, in which cleverly engineered metrology targets can translate pulse properties into highly sensitive, tunable signals.

Chapter 4 is motivated by the question in what way nonlinear metasurfaces can be used as a dynamic light source. We explore all-optical modulation of nonlinear emission via a secondary ultra-fast light pulse, establishing a basis for dynamic control of light generated through nonlinear processes. Specifically, we study third-harmonic generation from silicon Fano-resonant metasurfaces, where the resonance is tuned by free-carrier excitation by absorption of a visible pump pulse. The resonance tuning results in nearly complete suppression of third-harmonic generation. Modulation and recovery occur on (sub)picosecond timescales. According to the Drude model, the pump-induced refractive index change blue-shifts the metasurface resonance away from the generation pulse, causing a strong modulation of third harmonic conversion efficiency.

Finally, in **Chapter 5**, we apply the insights gained from the all-optical modulation study for spatial programmability of nonlinear light generation. Here, we demonstrate ultra-fast nonlinear beam shaping by using structured pump light to control both the spatial profile and directionality of third-harmonic emission. In our pumpprobe setup, a digital micro-mirror device generates spatial pump patterns of a visible pulse that are spatio-temporally overlapped with an infrared probe pulse on an all-dielectric Fano-resonant metasurface. In the previous Chapter (Ch. 4) we hypothesized a strong blue-shift of the resonance under pumping. In this Chapter (Ch. 5) we present experimental results that support this hypothesis, while also offering deeper insight into the effects of the photo-excited carriers, revealing that the resonances broadens more than it shifts. We study how the local harmonic deactivation of the spatially engineered pump pattern allows the generation of any harmonic beam profile. Furthermore, we analyze how the scattering of spatially periodic pump patterns convolve with the TH diffraction pattern, generating satellite orders that evidence coherent emission and directional control. Finally, we study the limits of this approach, via a spatial resolution analysis of the harmonic deactivation. This work opens the door to ultra-fast, precise control over harmonic beam profiles and directionality at generation stage. In doing so, it unlocks the potential for the original motivation that set this work in motion: to control spatially engineered, dynamic ultraviolet wavefronts, enabling highly precise and ultra-fast semiconductor metrology with nonlinear metasurfaces.

Future perspectives

Altogether, this Thesis provides new insights into the fields of semiconductor metrology and nonlinear optical control in nanophotonic structures. Balancing at the interface of both fields, we present experiments that deepen our understanding of the role of the effective index in quasi-bound state in the continuum metasurfaces; we present results that advance our knowledge of harmonic generation in Fano resonant metasurfaces with ultra-fast light pulses; and, we demonstrate ultra-fast dynamic spatial light control from nonlinear metasurfaces. These results demonstrate promising potential for nonlinear metasurfaces for advanced metrology and dynamic light control, and lay a strong foundation for practical applications and future perspectives. These include:

Nanostructures embedded in Fano resonant metasurface metrology Our work solely focused on a handful of simple structure-in-void metasurface designs, to study effective index and extract CD. This structure-in-void metrology principle holds for any kind of quasi-BIC metasurface design. One could pick any architecture from the vast pool of symmetry-broken quasi-BIC metasurface literature, with the asymmetry parameter serving as a direct link to the metrology parameter. Additionally, this approach does not stop at CD metrology. One could for example exploit symmetry protection in a third dimension, where the out of plane symmetry plays a role for OV metrology. Furthermore, new metasurface designs (such as meta-rings) could offer a significantly smaller footprint while still harnessing strong resonances, making them well-suited for applications including interlaced metrology. Finally, a direct implementation would be to include current metrology scattering targets inside a quasi-BIC metasurface void, instantly boosting optical scatterometry contrasts, and hence sensitivity and throughput.

Pulse engineered nonlinear emission: In general, most active metasurface research is dedicated to optimizing metasurface design for any specific functionality. Our results show that nonlinear metasurface output can not be seen separate from the external driver. This means that the nonlinear emission of a metasurface could, in principle, be engineered through excitation with a shaped optical pulse. By understanding the phase relationship in the nonlinear modal interference between a bright and a dark mode, one could design a temporal profile of the excitation pulse, that manipulates nonlinear emission in specific ways. For example, in the time trace of the pulse, it reaches an amplitude of one only when the nonlinear emission of the modes constructively interfere into a specific diffraction order, allowing total control of beam steering. This temporal trace can then be Fourier-transformed into the spectral domain, where it becomes accessible for precise pulse shaping.

Tailored ultra-small wavefront metrology: The search for optimal illumination that maximizes metrology sensitivity is an area of high interest. This becomes especially powerful when combined with dynamic wavefront shaping of UV and EUV beams. While our work focused on third-harmonic generation, future studies should explore higher-order nonlinearities, such as fifth-harmonic generation or even high-harmonic generation, to access EUV wavefronts. When paired with optimal illumination strategies (which could be as simple as gratings or other periodic modulations on structured surfaces) this approach could be exceptionally powerful for next-generation edge placement error, overlay, and critical dimension metrology techniques, allowing extreme fine resolution at the speed of light.

Samenvatting

Dynamische controle over niet-lineair licht en metrologie met resonante meta-oppervlakken

De drang van de mensheid naar vooruitgang is diep verankerd in onze innovatieve behoefte om dingen sneller, kleiner en efficiënter te maken. Weinig ontwikkelingen belichamen deze ambitie zo sterk als de voortdurend vernieuwende wereld van micro-elektronische chips. Dankzij extreme-ultravioletlithografie zijn indrukwekkende stappen in miniaturisatie mogelijk geworden, die aan de basis liggen van vrijwel alle moderne digitale infrastructuur, van smartphones en autonome systemen tot hardware voor kunstmatige intelligentie en cloud-datacenters. Een essentiële stap in de fabricage van zulke complexe nanostructuren is de nauwkeurige inspectie van details op de nanoschaal, een proces dat bekendstaat als metrologie. Geavanceerde lithografie kan slechts slagen met even zo geavanceerde metrologietechnieken, die niet-destructief werken en tegelijk een hoge snelheid, precisie en nauwkeurigheid op de nanoschaal behalen. Naarmate chipstructuren verder krimpen, wordt het steeds uitdagender om de juiste metrologieparameters te extraheren, aangezien conventionele optische metrologie fundamenteel begrensd is door de diffractielimiet van Abbe.

Niet-lineaire emissie van resonante optische meta-oppervlakken biedt een veelbelovende richting om deze uitdaging het hoofd te bieden. Metaoppervlakken zijn zorgvuldig ontworpen oppervlakken die bestaan uit reeksen van sub-golflengte nanostructuren (vaak aangeduid als meta-atomen), gerangschikt in periodieke of aperiodieke patronen. Deze metastructuren zijn ontworpen om licht te manipuleren met een hoge mate van controle die met conventionele optica niet haalbaar is. Sterke resonante effecten, zoals Fano-resonanties, kunnen worden benut om het contrast in lineaire metrologie te vergroten. Daarbovenop zijn resonante meta-oppervlakken uitgegroeid tot een van de krachtigste platforms voor het versterken van niet-lineaire optische effecten, waarbij de interactie van intense lichtvelden met nanogestructureerde oppervlakken leidt tot de generatie van nieuwe frequenties met kortere golflengtes (harmonische generatie). Niet-lineaire optische metrologie biedt twee belangrijke voordelen. Ten eerste zijn de gegenereerde harmonische golflengtes (veel) korter dan de fundamentele. Hoewel kortere golflengtes nog steeds onderhevig zijn aan de diffractielimiet van Abbe, maakt verschuiving naar kleinere schalen logischerwijs een verbeterde resolutie mogelijk. Ten tweede schaalt de niet-lineaire polarisatie met een macht van het elektrische nabije veld. Dit betekent dat kleine veranderingen in de lokale geometrie of de fundamentele nabijeveldverdeling kunnen leiden tot onevenredig grote variaties in de uitgezonden harmonische verre-veldintensiteit.

Het werk dat in dit Proefschrift wordt gepresenteerd is geïnspireerd door de wens om een koppeling te leggen tussen halfgeleider-metrologie en niet-lineaire optische controle in nanofotonische structuren. De methode waarbij niet-lineair licht wordt gebruikt voor metrologie levert twee verschillende scenarios op. In het eerste scenario fungeert het metaoppervlak zelf als metrologiedoelwit: de coherente harmonische generatie zorgt voor een verhoogde metrologiegevoeligheid dankzij de machtsafhankelijke aard van de niet-lineaire polarisatie. In dit kader leiden kleine geometrische variaties tot grote veranderingen in de niet-lineaire emissie, die direct kunnen worden gekoppeld aan metrologie-informatie van het verstrooiingsdoelwit. In het tweede scenario worden meta-oppervlakken gebruikt om compacte (extreem) ultravioletlichtbronnen te ontwikkelen die op hun beurt metrologiedoelwitten of microelektronische structuurelementen met nauwkeurig gevormde golffronten beschijnen voor het verkrijgen van geavanceerde metrologie-informatie.

Met dit werk willen we de basis leggen om de rijke natuurkunde van niet-lineaire diffractieve meta-oppervlakken binnen het domein te brengen van toegepaste, precieze halfgeleider-metrologie. We zijn een wetenschappelijk avontuur aangegaan om de mechanismen achter niet-lineaire emissie van resonante meta-oppervlakken te begrijpen. Om dit toekomstbeeld te realiseren, moeten we een reeks fundamentele vragen beantwoorden. Voor scenario 1: Hoe kunnen resonanties worden benut voor lineaire metrologie? En, Hoe verandert de niet-lineaire respons van Fano-resonanties onder excitatie met ultrakorte lichtpulsen? Voor scenario 2 verkennen we: Hoe kan een meta-oppervlak functioneren als een dynamische niet-lineaire lichtbron met nauwkeurig gevormde golffronten?

In **Hoofdstuk 2**, richten we onze eerste inspanningen op het begrijpen hoe resonante effecten kunnen worden ingezet om lineaire metrologie te verbeteren. We demonstreren metingen van kritieke afmetingen van structuurelementen met behulp van resonante meta-oppervlakken gebaseerd op quasi-gebonden toestanden in het continuüm-resonanties. De kern van ons werk is dat deze resonanties scherpe Fano-lijnvormen vertonen, die het voordeel hebben uiterst gevoelig te zijn voor minimale geometrische veranderingen in de architectuur van de meta-atomen. We laten een creatieve methode zien die gebaseerd is op lineaire transmissiemetingen van metrologiedoelwitten op basis van een metaoppervlak met diëlektrische schijf-gatstructuren. In het ontwerp van deze structuren is de holte (of het gat) structureel is opgevuld met de nanostructuren voor metrologie. In dit Hoofdstuk presenteren we zowel experimentele als gesimuleerde resultaten voor verschillende metaoppervlak-ontwerpen met structuren in een holte, en we schrijven de spectrale verschuiving van de resonantie toe aan de gevoeligheid voor een effectieve brekingsindex in de holte van de meta-atomen. Uit de gemeten transmissie kan direct de effectieve index worden bepaald en daarmee de kritieke afmeting. Deze benadering zou direct kunnen worden geïmplementeerd in bestaande productieprocessen voor halfgeleiders, door de holte in het metasurface-ontwerp op te vullen met standaard optische verstrooiingsdoelwitten, waarmee het optisch contrast aanzienlijk kan worden versterkt.

Hoofdstuk 3 zet onze eerste stap in het onderzoek naar niet-lineaire emissie van Fano-resonante metaopprvlakken onder variërende excitatiepulsen. We bestuderen derde-harmonische generatie in een vergelijkbaar schijf-gat metaoppervlak met een quasi-gebonden toestand in het continuüm resonantie, als opstap naar niet-lineaire optische metrologie. In dit Hoofdstuk analyseren we hoe de interferentie tussen heldere en donkere resonantiestanden, evenals in combinatie met de eigenschappen van de excitatiepuls, de niet-lineaire emissie beïnvloeden. We tonen aan dat het ontwerp van een niet-lineaire metaoppervlak niet los kan worden gezien van de externe aandrijving. Onze experimenten tonen asymmetriën in derde-harmonische diffractie-efficiënties en niet-Gaussisch gevormde spectrale kenmerken van de derde harmonische, die sterke variaties vertonen in de buurt van de fundamentele Fano-resonantie. We verklaren de onderliggende natuurkunde van deze observaties met een gekoppeld-oscillatormodel dat de wisselwerking tussen het externe aandrijvingsveld en de niet-lineaire respons van de resonantiestanden beschrijft. Dit model biedt een voorspellend kader om de resonantie interactie te benutten voor het optimaliseren van afstembare derde-harmonische diffractie-efficiëntie. De resultaten die in dit Hoofdstuk worden gepresenteerd positioneren puls-bestuurbare meta-oppervlakken als een krachtig platform voor niet-lineaire golfvormmanipulatie en frequentieconversie. Bovendien opent dit de weg naar niet-lineaire optische metrologie, waarin slim ontworpen metrologiedoelen pulskenmerken kunnen vertalen naar uiterst gevoelige, afstembare signalen.

Hoofdstuk 4 is gemotiveerd door de vraag op welke manier niet-lineaire meta-oppervlakken kunnen worden ingezet als dynamische lichtbron. We onderzoeken de met licht bestuurbare modulatie van niet-lineaire emissie via een secundaire ultrakorte lichtpuls, om zo de basis te leggen voor dynamische controle over niet-lineair gegenereerd licht. We bestuderen derde-harmonische generatie in silicium Fano-resonante meta-oppervlakken en regelen de metaoppervlak-resonantie via vrije ladingsdragers, opgewekt door absorptie van de tweede zichtbare pomp puls. Dit leidt tot een vrijwel volledige onderdrukking van de derde-harmonische generatie. Modulatie en herstel van de derde-harmonische generatie vinden plaats op (sub)picoseconde-tijdschaal. Volgens het Drude-model zorgt de pomp-geïnduceerde verandering in de brekingsindex voor een blauwverschuiving van de metaoppervlak-resonantie, spectraal weg van de generatie-lichtpuls, wat resulteert in een sterke modulatie van de efficiëntie van derde-harmonische conversie.

Tot slot, in **Hoofdstuk 5** passen we de inzichten die zijn verkregen uit de optische-modulatiestudie toe voor de ruimtelijke programmeerbaarheid van niet-lineaire lichtgeneratie. Hier laten we de realisatie zien van ultrakorte niet-lineaire lichtbundel patronen, waarbij gestructureerd pomplicht wordt gebruikt om het emissieprofiel en de richtingsgevoeligheid van de derde harmonische te regelen. We gebruiken een digitaal micro-spiegelsysteem in een pomp-sonde-opstelling, waarmee pomp-patronen van een zichtbare lichtpuls ruimtelijk en tijdelijk samenvallen met een infrarode sonde-puls op een volledig diëlektrische Fano-resonant metaoppervlak. In het vorige Hoofdstuk (Hoofdstuk 4) stelden we de hypothese dat de resonantie onder pomp-excitatie sterk blauw verschuift. In dit Hoofdstuk (Hoofdstuk 5) presenteren we experimentele resultaten die deze hypothese ondersteunen, en tegelijkertijd meer inzicht geven in de rol van de licht-aangeslagen ladingsdragers, waaruit blijkt dat de resonantie eerder verbreedt dan verschuift. We onderzoeken hoe lokale harmonische deactivering door het ruimtelijk ontworpen pomppatroon het mogelijk maakt om willekeurige harmonische lichtprofielen te genereren. Daarnaast analyseren we hoe de verstrooiing van ruimtelijk periodieke pomppatronen convolueert met het diffractiepatroon van de derde harmonische, waarbij satellietordes ontstaan die getuigen van coherente emissie en richtingscontrole. Ten slotte bestuderen we de grenzen van deze benadering aan de hand van een ruimtelijke resolutie-analyse van de harmonische deactivering. Dit werk opent de deur naar ultrasnelle, precieze controle over harmonische lichtprofielen en richtingsgevoeligheid tijdens het generatie stadium. Daarmee opent zich het potentieel van de oorspronkelijke motivatie achter dit onderzoek: het controleren van ruimtelijk ontworpen, dynamische ultraviolet-golffronten, waarmee uiterst nauwkeurige en ultrasnelle halfgeleider-metrologie met niet-lineaire meta-oppervlakken mogelijk wordt.

Toekomstperspectieven

Alles bij elkaar genomen biedt dit Proefschrift nieuwe inzichten in de vakgebieden van halfgeleider-metrologie en niet-lineaire optische controle in nanofotonische structuren. Op het raakvlak van beide disciplines presenteren we experimenten die ons begrip verdiepen van de rol van de effectieve brekingsindex in meta-oppervlakken met quasi-gebonden toestanden in het continuüm; we tonen resultaten die onze kennis over harmonische generatie in Fano-resonante meta-oppervlakken met ultrakorte lichtpulsen vergroten; en we demonstreren ultrasnelle, dynamische ruimtelijke lichtcontrole met niet-lineaire meta-oppervlakken. Deze bevindingen tonen het veelbelovende potentieel van niet-lineaire meta-oppervlakken voor geavanceerde metrologie en dynamische lichtsturing, en vormen een sterke basis voor praktische toepassingen en toekomstperspectieven. Deze omvatten onder meer:

Nanostructuren in Fano-resonante meta-oppervlakken-metrologie: Ons werk richtte zich uitsluitend op een beperkt aantal eenvoudige structuur-in-holte-metaoppervlakontwerpen, met als doel het bestuderen van de effectieve brekingsindex en het meten van de kritieke afmeting. Het onderliggende principe van deze structuur-in-holte-metrologie is echter toepasbaar op elk type quasi-gebonden toestanden in het continuüm-metaoppervlakeontwerp. Men zou elke architectuur kunnen kiezen uit de rijke literatuur over symmetrie-gebroken quasi-gebonden toestanden in het continuüm-meta-oppervlakken, waarbij de asymmetrieparameter direct kan worden gekoppeld aan de metrologie-parameter. Bovendien stopt deze benadering niet bij kritieke afmeting-metrologie. Zo kan men bijvoorbeeld symmetriebreking in een derde dimensie benutten, waarbij de symmetrie buiten het vlak relevant wordt voor uitlijn-metrologie. Nieuwe metaoppervlakontwerpen, zoals meta-ringen, kunnen bovendien een aanzienlijk kleinere oppervlak bieden, terwijl ze nog steeds sterke resonanties vertonen. Dit maakt ze bijzonder geschikt voor toepassingen zoals ”interlaced”-metrologie, een techniek waarbij het ontwerp van patronen uit verschillende lithografiestappen vervlochten is. Tot slot zou een directe implementatie kunnen bestaan uit het integreren van bestaande metrologie-doelwitstructuren in de holte van een quasi-gebonden toestanden in het continuüm-metaoppervlak, waarmee het optisch verstrooiingscontrast onmiddellijk wordt versterkt, daarmee ook de gevoeligheid en de doorvoersnelheid.

Gepulste excitatie bestuurbare niet-lineaire emissie: In het algemeen is het grootste deel van het onderzoek naar actieve meta-oppervlakken gericht op het optimaliseren van het metaoppervlakontwerp voor een specifieke functionaliteit. Onze resultaten tonen echter aan dat de niet-lineaire emissie van een metaoppervlak niet los gezien kan worden van de externe aandrijving. Dit impliceert dat de niet-lineaire emissie van een metaoppervlak in principe gestuurd kan worden via excitatie met een vormgegeven optische puls. Door het faseverloop te begrijpen van de niet-lineaire modale interferentie tussen een heldere en een donkere resonantiestanden, kan men het tijdsprofiel van de excitatiepuls zodanig ontwerpen dat de niet-lineaire emissie op specifieke manieren wordt gemanipuleerd. Zo kan bijvoorbeeld in het tijdverloop van de puls de amplitude zo worden ontworpden dat het slechts een waarde heeft op het moment dat de niet-lineaire emissie van de resonanties constructief interfereert in een specifieke diffractieorde, wat volledige controle over lichtbundelsturing mogelijk maakt. Dit tijdverloop kan vervolgens worden getransformeerd naar het spectrale domein via een Fourier-transformatie, waar het toegankelijk wordt voor nauwkeurige puls-vormgeving.

Op maat gemaakte ultra-kleine golffrontmetrologie: De zoektocht naar optimale verlichting die metrologiegevoeligheid maximaliseert, is een onderwerp van groot interesse. Dit wordt bijzonder krachtig wanneer het wordt gecombineerd met dynamisch vormbare golffrontprofielen van UV- en EUV-bundels. Hoewel ons werk zich richtte op derde-harmonische generatie, zouden toekomstige studies hogere-orde niet-lineariteiten moeten verkennen, zoals vijfde-harmonische generatie of zelfs hoge-harmonische generatie, om toegang te krijgen tot EUV-golffronten. In combinatie met optimale belichtingsstrategieën (die al zo eenvoudig kunnen zijn als roosters of andere periodieke modulaties op gestructureerde oppervlakken), kan deze methode buitengewoon krachtig zijn voor de volgende generatie metrologietechnieken. Dit maakt extreem fijne resolutie mogelijk, met de snelheid van het licht.

References

[1] E. Mansfield, B. Barnes, R. J. Kline, A. E. Vladar, Y. Obeng, and A. Davydov, *(IEEE) international roadmap for devices and systems^{TM} 2023 edition metrology*, IEEE pp. doi: 10.60627/FF6X–D213 (2023).

[2] K. Schuegraf, M. C. Abraham, A. Brand, M. Naik, and R. Thakur, *Semiconductor logic technology innovation to achieve sub-10 nm manufacturing*, IEEE J. Electron Devices Soc. **1**, 66 (2013).

[3] L. Li, X. Liu, S. Pal, S. Wang, C. K. Ober, and E. P. Giannelis, *Extreme ultraviolet resist materials for sub-7 nm patterning*, Chem. Soc. Rev. **46**, 4855 (2017).

[4] N. G. Orji, M. Badaroglu, B. M. Barnes, C. Beitia, B. D. Bunday, U. Celano, R. J. Kline, M. Neisser, Y. Obeng, and A. Vladar, *Metrology for the next generation of semiconductor devices*, Nat. Electron. **1**, 532 (2018).

[5] M. Lundstrom, *Moore's law forever?*, Science **299**, 210 (2003).

[6] C. A. Mack, *Fifty years of Moore's law*, IEEE Trans. Semicond. Manuf. **24**, 202 (2011).

[7] T. N. Theis, and H.-S. P. Wong, *The end of Moore's law: A new beginning for information technology*, Comput. Sci. Eng **19**, 41 (2017).

[8] F. OBrien, *The Apollo Guidance Computer: Architecture and operation* (Springer, 2010).

[9] A. J. den Boef, *Optical wafer metrology sensors for process-robust CD and overlay control in semiconductor device manufacturing*, Surf. Topogr. Metrol. Prop. **4**, 023001 (2016).

[10] A. C. Diebold, *Handbook of silicon semiconductor metrology* (CRC press, 2001).

[11] R. Rohrich, G. Oliveri, S. Kovaios, V. T. Tenner, A. J. Den Boef, J. T. Overvelde, and A. F. Koenderink, *Uncertainty estimation and design optimization of 2D diffraction-based overlay metrology targets*, ACS Photonics **7**, 2765 (2020).

[12] P. Leray, S. Cheng, D. Kandel, M. Adel, A. Marchelli, I. Vakshtein, M. Vasconi, and B. Salski, *Diffraction based overlay metrology: accuracy and performance on front end stack*, in *Proc. SPIE, Metrol. Inspect. Process Control Microlithogr. XXII* (SPIE, 2008), vol. 6922, pp. 252–263.

[13] U. Celano, D. Schmidt, C. Beitia, G. Orji, A. V. Davydov, and Y. Obeng, *Metrology for 2D materials: a perspective review from the international roadmap for devices and systems*, Nanoscale Adv. **6**, 2260 (2024).

[14] B. Su, T. Pan, P. Li, J. Chinn, X. Shi, and M. Dusa, *Sidewall angle measurements using CD SEM*, in *IEEE/SEMI 1998 IEEE/SEMI Advanced Semiconductor Manufacturing Conference and Workshop (Cat. No. 98CH36168)* (IEEE, 1998), pp. 259–261.

[15] ASML, *TWINSCAN EXE:5000 - high-NA EUV lithography system* (2024), accessed: 2025-07-29, URL `https://www.asml.com/en/products/euv-lithography-systems/twinscan-exe-5000`.

[16] J. Mulkens, B. Slachter, M. Kubis, W. Tel, P. Hinnen, M. Maslow, H. Dillen, E. Ma, K. Chou, X. Liu, et al., *Holistic approach for overlay and edge placement error to meet the 5nm technology node requirements*, in *Proc. SPIE, Metrol. Inspect. Process Control Microlithogr. XXXII* (SPIE, 2018), vol. 10585, pp. 375–388.

[17] C. Messinis, T. T. van Schaijk, N. Pandey, V. T. Tenner, S. Witte, J. F. de Boer, and A. den Boef, *Diffraction-based overlay metrology using angular-multiplexed acquisition of dark-field digital holograms*, Opt. Express **28**, 37419 (2020).

[18] B. Hoefflinger, in *Chips 2020: a guide to the future of nanoelectronics* (Springer, 2011), pp. 161–174.

[19] C. Messinis, T. T. van Schaijk, N. Pandey, A. Koolen, I. Shlesinger, X. Liu, S. Witte, J. F. de Boer, and A. Den Boef, *Aberration calibration and correction with nano-scatterers in digital holographic microscopy for semiconductor metrology*, Opt. Express **29**, 38237 (2021).

[20] N. Kossowski, Y. Tahmi, A. Loucif, M. Lepers, B. Wattellier, G. Vienne, S. Khadir, and P. Genevet, *Metrology of metasurfaces: optical properties*, npj Nanophotonics **2**, 5 (2025).

[21] L. Verstappen, E. Mos, P. Wardenier, H. Megens, E. Schmitt-Weaver, K. Bhattacharyya, O. Adam, G. Grzela, J. van Heijst, L. Willems, et al., *Holistic overlay control for multi-patterning process layers at the 10nm and 7nm nodes*, in *Proc. SPIE, Metrol. Inspect. Process Control Microlithogr. XXX* (SPIE, 2016), vol. 9778, pp. 645–652.

[22] J. Maas, M. Ebert, K. Bhattacharyya, H. Cramer, A. Becht, S. Keij, R. Plug, A. Fuchs, M. Kubis, T. Hoogenboom, et al., *Yieldstar: a new metrology platform for advanced lithography control*, in *27th European Mask and Lithography Conference* (SPIE, 2011), vol. 7985, pp. 146–155.

[23] A. E. Vladár, J. S. Villarrubia, J. Chawla, B. Ming, J. R. Kline, S. List, and M. T. Postek, *10nm three-dimensional CD-SEM metrology*, in *Proc. SPIE, Metrol. Inspect. Process Control Microlithogr.y XXVIII* (SPIE, 2014), vol. 9050, pp. 53–63.

[24] G. F. Lorusso, T. Ohashi, A. Yamaguchi, O. Inoue, T. Sutani, N. Horiguchi, J. Bömmels, C. J. Wilson, B. Briggs, C. L. Tan, et al., *Enabling CD SEM metrology for 5nm technology node and beyond*, in *Proc. SPIE, Metrol. Inspect. Process Control Microlithogr. XXXI* (SPIE, 2017), vol. 10145, pp. 367–375.

[25] S. W. Hell, and J. Wichmann, *Breaking the diffraction resolution limit by stimulated emission: stimulated-emission-depletion fluorescence microscopy*, Opt. Lett. **19**, 780 (1994).

[26] E. Betzig, G. H. Patterson, R. Sougrat, O. W. Lindwasser, S. Olenych, J. S. Bonifacino, M. W. Davidson, J. Lippincott-Schwartz, and H. F. Hess, *Imaging intracellular fluorescent proteins at nanometer resolution*, Science **313**, 1642 (2006).

[27] M. J. Rust, M. Bates, and X. Zhuang, *Sub-diffraction-limit imaging by stochastic optical reconstruction microscopy (storm)*, Nat. Methods **3**, 793 (2006).

[28] T. T. Van Schaijk, C. Messinis, N. Pandey, A. Koolen, S. Witte, J. F. De Boer, and A. Den Boef, *Diffraction-based overlay metrology from visible to infrared wavelengths using a single sensor*, J. Micro/Nanopattern. Mater. Metrol. **21**, 014001 (2022).

[29] H. Zang, Z. Zhang, Z. Huang, Y. Lu, and P. Wang, *High-precision two-dimensional displacement metrology based on matrix metasurface*, Sci. Adv. **10**, eadk2265 (2024).

[30] M. Singh, J. F. Sargent Jr, and K. M. Sutter, *Semiconductors and the semiconductor industry.*, Congressional Research Service (CRS) Reports and Issue Briefs pp. R47508–R47508 (2023).

[31] CSI Market, *ASML Holding NV - segment & geographic revenue breakdown* (2025), accessed: 2025-07-29, URL `https://csimarket.com/stocks/segments.php?code=ASML`.

[32] H.-T. Chen, A. J. Taylor, and N. Yu, *A review of metasurfaces: physics and applications*, Rep. Prog. Phys. **79**, 076401 (2016).

[33] W. Cai, and V. M. Shalaev, *Optical Metamaterials* (Springer, New York, NY, 2010).

[34] N. Engheta, and R. W. Ziolkowski, *Metamaterials: physics and engineering explorations* (John Wiley & Sons, 2006).

[35] G. Yoon, T. Tanaka, T. Zentgraf, and J. Rho, *Recent progress on metasurfaces: applications and fabrication*, J. Phys. D: Appl. Phys **54**, 383002 (2021).

[36] P. Lalanne, and G. M. Morris, *Highly improved convergence of the coupled-wave method for TM polarization*, J. Opt. Soc. Am. A **13**, 779 (1996).

[37] N. Yu, P. Genevet, M. A. Kats, F. Aieta, J.-P. Tetienne, F. Capasso, and Z. Gaburro, *Light propagation with phase discontinuities: generalized laws of reflection and refraction*, Science **334**, 333 (2011).

[38] R. M. Walser, *Electromagnetic metamaterials*, in *Complex Mediums II: beyond linear isotropic dielectrics* (SPIE, 2001), vol. 4467, pp. 1–15.

[39] J. B. Pendry, D. Schurig, and D. R. Smith, *Controlling electromagnetic fields*, Science **312**, 1780 (2006).

[40] A. Sihvola, *Metamaterials in electromagnetics*, Metamaterials **1**, 2 (2007).

[41] A. Sihvola, in *Advances in Electromagnetics of Complex Media and Metamaterials*, edited by A. P. Vinogradov (Springer, Dordrecht, Netherlands, 2003), pp. 3–17.

[42] D. R. Smith, W. J. Padilla, D. C. Vier, S. C. Nemat-Nasser, and S. Schultz, *Composite medium with simultaneously negative permeability and permittivity*, Phys. Rev. Lett. **84**, 4184 (2000).

[43] R. A. Shelby, D. R. Smith, and S. Schultz, *Experimental verification of a negative index of refraction*, Science **292**, 77 (2001).

[44] D. Schurig, J. J. Mock, B. Justice, S. A. Cummer, J. B. Pendry, A. F. Starr, and D. R. Smith, *Metamaterial electromagnetic cloak at microwave frequencies*, Science **314**, 977 (2006).

[45] C. L. Holloway, E. F. Kuester, J. A. Gordon, J. O'Hara, J. Booth, and D. R. Smith, *An overview of the theory and applications of metasurfaces: The two-dimensional equivalents of metamaterials*, IEEE Antennas Propag. Mag. **54**, 10 (2012).

[46] Y. Zhao, N. Engheta, and A. Alù, *Homogenization of plasmonic metasurfaces modeled as transmission-line loads*, Metamaterials **5**, 90 (2011).

[47] N. Yu, and F. Capasso, *Flat optics with designer metasurfaces*, Nat. Mater. **13**, 139 (2014).

[48] A. F. Koenderink, A. Alù, and A. Polman, *Nanophotonics: Shrinking light-based technology*, Science **348**, 516 (2015).

[49] J. A. Schuller, E. S. Barnard, W. Cai, Y. C. Jun, J. S. White, and M. L. Brongersma, *Plasmonics for extreme light concentration and manipulation*, Nat. Mater. **9**, 193 (2010).

[50] G. Mie, *Beiträge zur Optik trüber Medien, speziell kolloidaler Metallösungen*, Ann.

Phys. **330**, 377 (1908).

[51] S. Kruk, and Y. Kivshar, *Functional meta-optics and nanophotonics governed by Mie resonances*, ACS Photonics **4**, 2638 (2017).

[52] K. Koshelev, and Y. Kivshar, *Dielectric resonant metaphotonics*, ACS Photonics **8**, 102 (2020).

[53] A. I. Kuznetsov, A. E. Miroshnichenko, M. L. Brongersma, Y. S. Kivshar, and B. Luk'yanchuk, *Optically resonant dielectric nanostructures*, Science **354**, aag2472 (2016).

[54] A. I. Kuznetsov, A. E. Miroshnichenko, Y. H. Fu, J. Zhang, and B. Luk'yanchuk, *Magnetic light*, Sci. Rep. **2**, 492 (2012).

[55] A. B. Evlyukhin, S. M. Novikov, U. Zywietz, R. L. Eriksen, C. Reinhardt, S. I. Bozhevolnyi, and B. N. Chichkov, *Demonstration of magnetic dipole resonances of dielectric nanospheres in the visible region*, Nano Lett. **12**, 3749 (2012).

[56] S. Person, M. Jain, Z. Lapin, J. J. Sáenz, G. Wicks, and L. Novotny, *Demonstration of zero optical backscattering from single nanoparticles*, Nano Lett. **13**, 1806 (2013).

[57] A. E. Miroshnichenko, A. B. Evlyukhin, Y. F. Yu, R. M. Bakker, A. Chipouline, A. I. Kuznetsov, B. Luk'yanchuk, B. N. Chichkov, and Y. S. Kivshar, *Nonradiating anapole modes in dielectric nanoparticles*, Nat. Commun. **6**, 8069 (2015).

[58] Y. Yang, I. I. Kravchenko, D. P. Briggs, and J. Valentine, *All-dielectric metasurface analogue of electromagnetically induced transparency*, Nat. Commun. **5**, 5753 (2014).

[59] M. F. Limonov, M. V. Rybin, A. N. Poddubny, and Y. S. Kivshar, *Fano resonances in photonics*, Nat. Photon. **11**, 543 (2017).

[60] B. Hopkins, D. S. Filonov, A. E. Miroshnichenko, F. Monticone, A. Alù, and Y. S. Kivshar, *Interplay of magnetic responses in all-dielectric oligomers to realize magnetic Fano resonances*, ACS Photonics **2**, 724 (2015).

[61] M. V. Rybin, K. L. Koshelev, Z. F. Sadrieva, K. B. Samusev, A. A. Bogdanov, M. F. Limonov, and Y. S. Kivshar, *High-Q supercavity modes in subwavelength dielectric resonators*, Phys. Rev. Lett. **119**, 243901 (2017).

[62] K. Koshelev, S. Lepeshov, M. Liu, A. Bogdanov, and Y. Kivshar, *Asymmetric metasurfaces with high-Q resonances governed by bound states in the continuum*, Phys. Rev. Lett. **121**, 193903 (2018).

[63] S. R. K. Rodriguez, A. Abass, B. Maes, O. T. Janssen, G. Vecchi, and J. Gómez Rivas, *Coupling bright and dark plasmonic lattice resonances*, Phys. Rev. X **1**, 021019 (2011).

[64] J. von Neumann, and E. P. Wigner, in *The Collected Works of Eugene Paul Wigner: Part A: The Scientific Papers* (Springer, 1993), pp. 294–297.

[65] H. Friedrich, and D. Wintgen, *Interfering resonances and bound states in the continuum*, Phys. Rev. A **32**, 3231 (1985).

[66] Y. Plotnik, O. Peleg, F. Dreisow, M. Heinrich, S. Nolte, A. Szameit, and M. Segev, *Experimental observation of optical bound states in the continuum*, Phys. Rev. Lett. **107**, 183901 (2011).

[67] K. Koshelev, A. Bogdanov, and Y. Kivshar, *Meta-optics and bound states in the continuum*, Sci. Bull. **64**, 836 (2019).

[68] U. Fano, *Effects of configuration interaction on intensities and phase shifts*, Phys. Rev. **124**, 1866 (1961).

[69] C. Ott, A. Kaldun, P. Raith, K. Meyer, M. Laux, J. Evers, C. H. Keitel, C. H. Greene, and T. Pfeifer, *Lorentz meets Fano in spectral line shapes: a universal phase and its laser control*, Science **340**, 716 (2013).

[70] I. Staude, A. E. Miroshnichenko, M. Decker, N. T. Fofang, S. Liu, E. Gonzales, J. Dominguez, T. S. Luk, D. N. Neshev, I. Brener, et al., *Tailoring directional scattering through magnetic and electric resonances in subwavelength silicon nanodisks*, ACS Nano **7**, 7824 (2013).

[71] M. Decker, I. Staude, M. Falkner, J. Dominguez, D. N. Neshev, I. Brener, T. Pertsch, and Y. S. Kivshar, *High-efficiency dielectric Huygens surfaces*, Adv. Opt. Mater. **3**, 813 (2015).

[72] C. U. Hail, M. Foley, R. Sokhoyan, L. Michaeli, and H. A. Atwater, *High quality factor metasurfaces for two-dimensional wavefront manipulation*, Nat. Commun. **14**, 8476 (2023).

[73] L. Wang, S. Kruk, H. Tang, T. Li, I. Kravchenko, D. N. Neshev, and Y. S. Kivshar, *Grayscale transparent metasurface holograms*, Optica **3**, 1504 (2016).

[74] A. Cordaro, H. Kwon, D. Sounas, A. F. Koenderink, A. Alù, and A. Polman, *High-index dielectric metasurfaces performing mathematical operations*, Nano Lett. **19**, 8418 (2019).

[75] S.-J. Kim, I. Kim, S. Choi, H. Yoon, C. Kim, Y. Lee, C. Choi, J. Son, Y. W. Lee, J. Rho, et al., *Reconfigurable all-dielectric Fano metasurfaces for strong full-space intensity modulation of visible light*, Nanoscale Horiz. **5**, 1088 (2020).

[76] R. Sokhoyan, C. U. Hail, M. Foley, M. Y. Grajower, and H. A. Atwater, *All-dielectric high-Q dynamically tunable transmissive metasurfaces*, Laser Photonics Rev. **18**, 2300980 (2024).

[77] C. Cui, C. Zhou, S. Yuan, X. Qiu, L. Zhu, Y. Wang, Y. Li, J. Song, Q. Huang, Y. Wang, et al., *Multiple Fano resonances in symmetry-breaking silicon metasurface for manipulating light emission*, ACS Photonics **5**, 4074 (2018).

[78] Y. Hu, X. Wang, X. Luo, X. Ou, L. Li, Y. Chen, P. Yang, S. Wang, and H. Duan, *All-dielectric metasurfaces for polarization manipulation: principles and emerging applications*, Nanophotonics **9**, 3755 (2020).

[79] J. Hu, T. Lang, and G.-h. Shi, *Simultaneous measurement of refractive index and temperature based on all-dielectric metasurface*, Opt. Express **25**, 15241 (2017).

[80] G.-D. Liu, X. Zhai, L.-L. Wang, Q. Lin, S.-X. Xia, X. Luo, and C.-J. Zhao, *A high-performance refractive index sensor based on Fano resonance in Si split-ring metasurface*, Plasmonics **13**, 15 (2018).

[81] J. Wang, J. Kühne, T. Karamanos, C. Rockstuhl, S. A. Maier, and A. Tittl, *All-dielectric crescent metasurface sensor driven by bound states in the continuum*, Adv. Funct. Mater. **31**, 2104652 (2021).

[82] R. D. Buijs, T. A. Wolterink, G. Gerini, E. Verhagen, and A. F. Koenderink, *Programming metasurface near-fields for nano-optical sensing*, Adv. Opt. Mater. **9**, 2100435 (2021).

[83] X. Chen, Y. Zhang, G. Cai, J. Zhuo, K. Lai, and L. Ye, *All-dielectric metasurfaces*

with high Q-factor Fano resonances enabling multi-scenario sensing, Nanophotonics **11**, 4537 (2022).

[84] H.-H. Hsiao, Y.-C. Hsu, A.-Y. Liu, J.-C. Hsieh, and Y.-H. Lin, *Ultrasensitive refractive index sensing based on the quasi-bound states in the continuum of all-dielectric metasurfaces*, Adv. Opt. Mater. **10**, 2200812 (2022).

[85] Z. Liu, T. Guo, Q. Tan, Z. Hu, Y. Sun, H. Fan, Z. Zhang, Y. Jin, and S. He, *Phase interrogation sensor based on all-dielectric BIC metasurface*, Nano Lett. **23**, 10441 (2023).

[86] T. A. Wolterink, R. D. Buijs, G. Gerini, E. Verhagen, and A. F. Koenderink, *Calibration-based overlay sensing with minimal-footprint targets*, Appl. Phys. Lett **119**, 111104 (2021).

[87] L. Kühner, L. Sortino, R. Berté, J. Wang, H. Ren, S. A. Maier, Y. Kivshar, and A. Tittl, *Radial bound states in the continuum for polarization-invariant nanophotonics*, Nat. Commun. **13**, 4992 (2022).

[88] N. Feldman, K. M. Goeloe, A. J. den Boef, L. V. Amitonova, and A. F. Koenderink, *Nanometer interlaced displacement metrology using diffractive Pancharatnam-Berry and detour phase metasurfaces*, ACS Photonics **11**, 5229 (2024).

[89] R. Röhrich, *Unconventional metrology: Merging nanophotonics with computational imaging*, Ph.D. thesis, University of Amsterdam, Amsterdam, The Netherlands (2020).

[90] R. D. Buijs, N. J. Schilder, T. A. Wolterink, G. Gerini, E. Verhagen, and A. F. Koenderink, *Super-resolution without imaging: Library-based approaches using near-to-far-field transduction by a nanophotonic structure*, ACS Photonics **7**, 3246 (2020).

[91] G. H. Yuan, and N. I. Zheludev, *Detecting nanometric displacements with optical ruler metrology*, Science **364**, 771 (2019).

[92] G. Grinblat, *Nonlinear dielectric nanoantennas and metasurfaces: frequency conversion and wavefront control*, ACS Photonics **8**, 3406 (2021).

[93] B. Sain, C. Meier, and T. Zentgraf, *Nonlinear optics in all-dielectric nanoantennas and metasurfaces: a review*, Adv. Photon. **1**, 024002 (2019).

[94] Z. Wang, R. Lin, J. Yao, and D. P. Tsai, *All-dielectric nonlinear metasurface: from visible to vacuum ultraviolet*, npj Nanophotonics **2**, 4 (2025).

[95] R. W. Boyd, A. L. Gaeta, and E. Giese, in *Springer Handbook of Atomic, Molecular, and Optical Physics* (Springer, 2008), pp. 1097–1110.

[96] P. Vabishchevich, and Y. Kivshar, *Nonlinear photonics with metasurfaces*, Photonics Res. **11**, B50 (2023).

[97] Y. Yang, W. Wang, A. Boulesbaa, I. I. Kravchenko, D. P. Briggs, A. Puretzky, D. Geohegan, and J. Valentine, *Nonlinear Fano-resonant dielectric metasurfaces*, Nano Lett. **15**, 7388 (2015).

[98] L. Xu, M. Rahmani, K. Zangeneh Kamali, A. Lamprianidis, L. Ghirardini, J. Sautter, R. Camacho-Morales, H. Chen, M. Parry, I. Staude, et al., *Boosting third-harmonic generation by a mirror-enhanced anapole resonator*, Light Sci. Appl **7**, 44 (2018).

[99] Z. Liu, Y. Xu, Y. Lin, J. Xiang, T. Feng, Q. Cao, J. Li, S. Lan, and J. Liu, *High-Q quasibound states in the continuum for nonlinear metasurfaces*, Phys. Rev. Lett. **123**,

253901 (2019).

[100] K. Koshelev, S. Kruk, E. Melik-Gaykazyan, J.-H. Choi, A. Bogdanov, H.-G. Park, and Y. Kivshar, *Subwavelength dielectric resonators for nonlinear nanophotonics*, Science **367**, 288 (2020).

[101] R. Sarma, J. Xu, D. De Ceglia, L. Carletti, S. Campione, J. Klem, M. B. Sinclair, M. A. Belkin, and I. Brener, *An all-dielectric polaritonic metasurface with a giant nonlinear optical response*, Nano Lett. **22**, 896 (2022).

[102] L. Wang, S. Kruk, K. Koshelev, I. Kravchenko, B. Luther-Davies, and Y. Kivshar, *Nonlinear wavefront control with all-dielectric metasurfaces*, Nano Lett. **18**, 3978 (2018).

[103] Y. Gao, Y. Fan, Y. Wang, W. Yang, Q. Song, and S. Xiao, *Nonlinear holographic all-dielectric metasurfaces*, Nano Lett. **18**, 8054 (2018).

[104] K. Koshelev, Y. Tang, Z. Hu, I. I. Kravchenko, G. Li, and Y. Kivshar, *Resonant chiral effects in nonlinear dielectric metasurfaces*, ACS Photonics **10**, 298 (2023).

[105] T. Santiago-Cruz, S. D. Gennaro, O. Mitrofanov, S. Addamane, J. Reno, I. Brener, and M. V. Chekhova, *Resonant metasurfaces for generating complex quantum states*, Science **377**, 991 (2022).

[106] P. R. Sharapova, S. S. Kruk, and A. S. Solntsev, *Nonlinear dielectric nanoresonators and metasurfaces: Toward efficient generation of entangled photons*, Laser Photonics Rev. **17**, 2200408 (2023).

[107] R. Camacho-Morales, M. Rahmani, S. Kruk, L. Wang, L. Xu, D. A. Smirnova, A. S. Solntsev, A. Miroshnichenko, H. H. Tan, F. Karouta, et al., *Nonlinear generation of vector beams from AlGaAs nanoantennas*, Nano Lett. **16**, 7191 (2016).

[108] C. Schlickriede, S. S. Kruk, L. Wang, B. Sain, Y. Kivshar, and T. Zentgraf, *Nonlinear imaging with all-dielectric metasurfaces*, Nano Lett. **20**, 4370 (2020).

[109] S. S. Kruk, L. Wang, B. Sain, Z. Dong, J. Yang, T. Zentgraf, and Y. Kivshar, *Asymmetric parametric generation of images with nonlinear dielectric metasurfaces*, Nat. Photon. **16**, 561 (2022).

[110] L. Xu, K. Zangeneh Kamali, L. Huang, M. Rahmani, A. Smirnov, R. Camacho-Morales, Y. Ma, G. Zhang, M. Woolley, D. Neshev, et al., *Dynamic nonlinear image tuning through magnetic dipole quasi-BIC ultrathin resonators*, Adv. Sci. **6**, 1802119 (2019).

[111] A. Krasnok, M. Tymchenko, and A. Alù, *Nonlinear metasurfaces: a paradigm shift in nonlinear optics*, Mater. Today **21**, 8 (2018).

[112] G. New, *Introduction to nonlinear optics* (Cambridge University Press, 2011).

[113] S. Liu, M. B. Sinclair, S. Saravi, G. A. Keeler, Y. Yang, J. Reno, G. M. Peake, F. Setzpfandt, I. Staude, T. Pertsch, et al., *Resonantly enhanced second-harmonic generation using III–V semiconductor all-dielectric metasurfaces*, Nano Lett. **16**, 5426 (2016).

[114] F. Timpu, J. Sendra, C. Renaut, L. Lang, M. Timofeeva, M. T. Buscaglia, V. Buscaglia, and R. Grange, *Lithium niobate nanocubes as linear and nonlinear ultraviolet Mie resonators*, ACS Photonics **6**, 545 (2019).

[115] A. Sergeyev, R. Geiss, A. S. Solntsev, A. A. Sukhorukov, F. Schrempel, T. Pertsch, and R. Grange, *Enhancing guided second-harmonic light in lithium niobate nanowires*,

ACS Photonics **2**, 687 (2015).

[116] J. Ma, F. Xie, W. Chen, J. Chen, W. Wu, W. Liu, Y. Chen, W. Cai, M. Ren, and J. Xu, *Nonlinear lithium niobate metasurfaces for second harmonic generation*, Laser Photonics Rev. **15**, 2000521 (2021).

[117] J. Zyss, *Molecular nonlinear optics: materials, physics, and devices* (Academic press, 2013).

[118] I. Staude, and J. Schilling, *Metamaterial-inspired silicon nanophotonics*, Nat. Photon. **11**, 274 (2017).

[119] Y. Kivshar, *All-dielectric meta-optics and non-linear nanophotonics*, Natl. Sci. Rev. **5**, 144 (2018).

[120] F. Bijloo, A. F. Koenderink, P. M. Kraus, and A. J. Den Boef, *Method for nonlinear optical measurement of parameter*, WO Patent No. 2024/165217 A1 (2024), World Intellectual Property Organization. Available at: `https://patents.google.com/patent/WO2024165217A1/en`.

[121] J. A. Squier, M. Müller, G. Brakenhoff, and K. R. Wilson, *Third harmonic generation microscopy*, Opt. Express **3**, 315 (1998).

[122] K. Murzyn, M. L. van der Geest, L. Guery, Z. Nie, P. van Essen, S. Witte, and P. M. Kraus, *Breaking Abbes diffraction limit with harmonic deactivation microscopy*, Sci. Adv. **10**, eadp3056 (2024).

[123] A. Forbes, M. de Oliveira, and M. R. Dennis, *Structured light*, Nat. Photonics **15**, 253 (2021).

[124] D. Bouchet, J. Seifert, and A. P. Mosk, *Optimizing illumination for precise multi-parameter estimations in coherent diffractive imaging*, Opt. Lett. **46**, 254 (2021).

[125] S. Keren-Zur, O. Avayu, L. Michaeli, and T. Ellenbogen, *Nonlinear beam shaping with plasmonic metasurfaces*, ACS Photonics **3**, 117 (2016).

[126] F. Walter, G. Li, C. Meier, S. Zhang, and T. Zentgraf, *Ultrathin nonlinear metasurface for optical image encoding*, Nano Lett. **17**, 3171 (2017).

[127] J. Scheuer, *Metasurfaces-based holography and beam shaping: engineering the phase profile of light*, Nanophotonics **6**, 137 (2017).

[128] S. Keren-Zur, L. Michaeli, H. Suchowski, and T. Ellenbogen, *Shaping light with nonlinear metasurfaces*, Adv. Opt. Photonics **10**, 309 (2018).

[129] T. Cui, B. Bai, and H.-B. Sun, *Tunable metasurfaces based on active materials*, Adv. Funct. Mater. **29**, 1806692 (2019).

[130] A. M. Shaltout, V. M. Shalaev, and M. L. Brongersma, *Spatiotemporal light control with active metasurfaces*, Science **364**, eaat3100 (2019).

[131] L. Kang, R. P. Jenkins, and D. H. Werner, *Recent progress in active optical metasurfaces*, Adv. Opt. Mater. **7**, 1801813 (2019).

[132] J. Yang, S. Gurung, S. Bej, P. Ni, and H. W. H. Lee, *Active optical metasurfaces: comprehensive review on physics, mechanisms, and prospective applications*, Rep. Prog. Phys. **85**, 036101 (2022).

[133] A. L. Holsteen, S. Raza, P. Fan, P. G. Kik, and M. L. Brongersma, *Purcell effect for active tuning of light scattering from semiconductor optical antennas*, Science **358**, 1407 (2017).

[134] N. I. Zheludev, and E. Plum, *Reconfigurable nanomechanical photonic metamaterials*, Nat. Nanotechnol. **11**, 16 (2016).

[135] J.-Y. Ou, E. Plum, L. Jiang, and N. I. Zheludev, *Reconfigurable photonic metamaterials*, Nano Lett. **11**, 2142 (2011).

[136] M. Z. Alam, I. De Leon, and R. W. Boyd, *Large optical nonlinearity of indium tin oxide in its epsilon-near-zero region*, Science **352**, 795 (2016).

[137] G. Kafaie Shirmanesh, R. Sokhoyan, R. A. Pala, and H. A. Atwater, *Dual-gated active metasurface at 1550 nm with wide (> 300) phase tunability*, Nano Lett. **18**, 2957 (2018).

[138] Q. Wang, E. T. Rogers, B. Gholipour, C.-M. Wang, G. Yuan, J. Teng, and N. I. Zheludev, *Optically reconfigurable metasurfaces and photonic devices based on phase change materials*, Nat. Photon. **10**, 60 (2016).

[139] A. Karvounis, B. Gholipour, K. F. MacDonald, and N. I. Zheludev, *All-dielectric phase-change reconfigurable metasurface*, Appl. Phys. Lett **109**, 051103 (2016).

[140] A. Komar, Z. Fang, J. Bohn, J. Sautter, M. Decker, A. Miroshnichenko, T. Pertsch, I. Brener, Y. S. Kivshar, I. Staude, et al., *Electrically tunable all-dielectric optical metasurfaces based on liquid crystals*, Appl. Phys. Lett **110**, 071109 (2017).

[141] M. R. Shcherbakov, P. P. Vabishchevich, A. S. Shorokhov, K. E. Chong, D.-Y. Choi, I. Staude, A. E. Miroshnichenko, D. N. Neshev, A. A. Fedyanin, and Y. S. Kivshar, *Ultrafast all-optical switching with magnetic resonances in nonlinear dielectric nanostructures*, Nano Lett. **15**, 6985 (2015).

[142] K. Wang, B. M. Szydłowska, G. Wang, X. Zhang, J. J. Wang, J. J. Magan, L. Zhang, J. N. Coleman, J. Wang, and W. J. Blau, *Ultrafast nonlinear excitation dynamics of black phosphorus nanosheets from visible to mid-infrared*, ACS Nano **10**, 6923 (2016).

[143] M. R. Shcherbakov, S. Liu, V. V. Zubyuk, A. Vaskin, P. P. Vabishchevich, G. Keeler, T. Pertsch, T. V. Dolgova, I. Staude, I. Brener, et al., *Ultrafast all-optical tuning of direct-gap semiconductor metasurfaces*, Nat. Commun. **8**, 17 (2017).

[144] D. Zhang, Y. Chen, S. Gong, W. Wu, W. Cai, M. Ren, X. Ren, S. Zhang, G. Guo, and J. Xu, *All-optical modulation of quantum states by nonlinear metasurface*, Light Sci. Appl **11**, 58 (2022).

[145] M. A. Masharin, T. Oskolkova, F. Isik, H. Volkan Demir, A. K. Samusev, and S. V. Makarov, *Giant ultrafast all-optical modulation based on exceptional points in exciton–polariton perovskite metasurfaces*, ACS Nano **18**, 3447 (2024).

[146] M. Maiuri, A. Schirato, G. Cerullo, and G. Della Valle, *Ultrafast all-optical metasurfaces: Challenges and new frontiers*, ACS Photonics **11**, 2888 (2024).

[147] T. Li, H. Xu, M. Panmai, T. Shao, G. Gao, F. Xu, G. Hu, S. Wang, Z. Wang, and S. Zhu, *Ultrafast metaphotonics*, Ultrafast Sci. **4**, 0074 (2024).

[148] A. E. Miroshnichenko, S. Flach, and Y. S. Kivshar, *Fano resonances in nanoscale structures*, Rev. Mod. Phys. **82**, 2257 (2010).

[149] E. Melik-Gaykazyan, K. Koshelev, J.-H. Choi, S. S. Kruk, A. Bogdanov, H.-G. Park, and Y. Kivshar, *From Fano to quasi-BIC resonances in individual dielectric nanoantennas*, Nano Lett. **21**, 1765 (2021).

[150] S. Fan, *Sharp asymmetric line shapes in side-coupled waveguide-cavity systems*, Appl. Phys. Lett **80**, 908 (2002).

[151] D. R. Abujetas, M. A. Mandujano, E. R. Méndez, and J. A. Sánchez-Gil, *High-contrast Fano resonances in single semiconductor nanorods*, ACS Photonics **4**, 1814 (2017).

[152] A. Krasnok, and A. Alú, *Low-symmetry nanophotonics*, ACS Photonics **9**, 2 (2022).

[153] S. Campione, S. Liu, L. I. Basilio, L. K. Warne, W. L. Langston, T. S. Luk, J. R. Wendt, J. L. Reno, G. A. Keeler, I. Brener, et al., *Broken symmetry dielectric resonators for high quality factor Fano metasurfaces*, ACS Photonics **3**, 2362 (2016).

[154] Y. Zhou, S. Guo, A. C. Overvig, and A. Alù, *Multiresonant nonlocal metasurfaces*, Nano Lett. **23**, 6768 (2023).

[155] A. Overvig, and A. Alù, *Wavefront-selective Fano resonant metasurfaces*, Adv. Photon. **3**, 026002 (2021).

[156] S.-D. Liu, E. S. P. Leong, G.-C. Li, Y. Hou, J. Deng, J. H. Teng, H. C. Ong, and D. Y. Lei, *Polarization-independent multiple Fano resonances in plasmonic nonamers for multimode-matching enhanced multiband second-harmonic generation*, ACS Nano **10**, 1442 (2016).

[157] S. Zhang, K. Bao, N. J. Halas, H. Xu, and P. Nordlander, *Substrate-induced Fano resonances of a plasmonic nanocube: a route to increased-sensitivity localized surface plasmon resonance sensors revealed*, Nano Lett. **11**, 1657 (2011).

[158] S. B. Saadatmand, V. Ahmadi, and S. M. Hamidi, *Quasi-BIC based all-dielectric metasurfaces for ultra-sensitive refractive index and temperature sensing*, Sci. Rep. **13**, 20625 (2023).

[159] M. Luo, Y. Zhou, X. Zhao, Z. Guo, Y. Li, Q. Wang, J. Liu, W. Luo, Y. Shi, A. Q. Liu, et al., *High-sensitivity optical sensors empowered by quasi-bound states in the continuum in a hybrid metal–dielectric metasurface*, ACS Nano **18**, 6477 (2024).

[160] G. Zito, G. Siciliano, A. Seifalinezhad, B. Miranda, V. Lanzio, A. Schwartzberg, G. Gigli, A. Turco, I. Rendina, V. Mocella, et al., *Molecularly imprinted polymer sensor empowered by bound states in the continuum for selective trace-detection of TGF-beta*, Adv. Sci. **11**, 2401843 (2024).

[161] M. F. Limonov, *Fano resonance for applications*, Adv. Opt. Photonics **13**, 703 (2021).

[162] S. Yuan, X. Qiu, C. Cui, L. Zhu, Y. Wang, Y. Li, J. Song, Q. Huang, and J. Xia, *Strong photoluminescence enhancement in all-dielectric Fano metasurface with high quality factor*, ACS Nano **11**, 10704 (2017).

[163] A. S. Kupriianov, Y. Xu, A. Sayanskiy, V. Dmitriev, Y. S. Kivshar, and V. R. Tuz, *Metasurface engineering through bound states in the continuum*, Phys. Rev. Appl. **12**, 014024 (2019).

[164] C. Zhou, L. Huang, R. Jin, L. Xu, G. Li, M. Rahmani, X. Chen, W. Lu, and A. E. Miroshnichenko, *Bound states in the continuum in asymmetric dielectric metasurfaces*, Laser Photonics Rev. **17**, 2200564 (2023).

[165] K. Koshelev, Y. Tang, K. Li, D.-Y. Choi, G. Li, and Y. Kivshar, *Nonlinear metasurfaces governed by bound states in the continuum*, ACS Photonics **6**, 1639 (2019).

[166] V. R. Tuz, V. V. Khardikov, A. S. Kupriianov, K. L. Domina, S. Xu, H. Wang, and H.-B. Sun, *High-quality trapped modes in all-dielectric metamaterials*, Opt. Express **26**, 2905 (2018).

[167] J. Algorri, F. DellOlio, Y. Ding, F. Labbé, V. Dmitriev, J. López-Higuera, J. Sánchez-Pena, L. Andreani, M. Galli, and D. Zografopoulos, *Experimental demonstration of a silicon-slot quasi-bound state in the continuum in near-infrared all-dielectric metasurfaces*, Opt. Laser Technol. **161**, 109199 (2023).

[168] B. Bunday, C. Montgomery, W. Montgomery, and A. Cepler, *Photoresist shrinkage effects in 16 nm node extreme ultraviolet (EUV) photoresist targets*, in *Proc. SPIE, Metrol. Inspect. Process Control Microlithogr. XXVII* (SPIE, 2013), vol. 8681, pp. 173–187.

[169] C. Zhou, T. Pu, J. Huang, M. Fan, and L. Huang, *Manipulating optical scattering of quasi-BIC in dielectric metasurface with off-center hole*, Nanomaterials **12**, 54 (2021).

[170] J. Algorri, V. Dmitriev, H. Hernández-Figueroa, L. Rodríguez-Cobo, F. DellOlio, A. Cusano, J. López-Higuera, and D. Zografopoulos, *Polarization-independent hollow nanocuboid metasurfaces with robust quasi-bound states in the continuum*, Opt. Mater. **147**, 114631 (2024).

[171] J. Kühne, J. Wang, T. Weber, L. Kühner, S. A. Maier, and A. Tittl, *Fabrication robustness in BIC metasurfaces*, Nanophotonics **10**, 4305 (2021).

[172] A. Krokhin, P. Halevi, and J. Arriaga, *Long-wavelength limit (homogenization) for two-dimensional photonic crystals*, Phys. Rev. B **65**, 115208 (2002).

[173] F. Capolino, *Theory and phenomena of metamaterials* (CRC press, 2017).

[174] S. Foteinopoulou, *Photonic crystals as metamaterials*, Physica B **407**, 4056 (2012).

[175] M. Hammer, and O. V. Ivanova, *Effective index approximations of photonic crystal slabs: a 2-to-1-D assessment*, Opt. Quantum Electron. **41**, 267 (2009).

[176] S. Rytov, *Electromagnetic properties of a finely stratified medium*, Sov. Phys. JETP **2**, 466 (1956).

[177] P. Yeh, A. Yariv, and C.-S. Hong, *Electromagnetic propagation in periodic stratified media. I. general theory*, J. Opt. Soc. Am. A **67**, 423 (1977).

[178] M. L. Tseng, Y. Jahani, A. Leitis, and H. Altug, *Dielectric metasurfaces enabling advanced optical biosensors*, ACS Photonics **8**, 47 (2020).

[179] H. Kim, H. Yun, S. Jeong, S. Lee, E. Cho, and J. Rho, *Optical metasurfaces for biomedical imaging and sensing*, ACS Nano **19**, 3085 (2025).

[180] A. J. Ollanik, I. O. Oguntoye, G. Z. Hartfield, and M. D. Escarra, *Highly sensitive, affordable, and adaptable refractive index sensing with silicon-based dielectric metasurfaces*, Adv. Mater. Technol. **4**, 1800567 (2019).

[181] W. Chen, M. Li, W. Zhang, and Y. Chen, *Dual-resonance sensing for environmental refractive index based on quasi-BIC states in all-dielectric metasurface*, Nanophotonics **12**, 1147 (2023).

[182] A. Di Francescantonio, A. Zilli, D. Rocco, V. Vinel, L. Coudrat, F. Conti, P. Biagioni, L. Duò, A. Lemaître, C. De Angelis, et al., *All-optical free-space routing of upconverted light by metasurfaces via nonlinear interferometry*, Nat. Nanotechnol. **19**, 298 (2024).

[183] C. Zou, J. Sautter, F. Setzpfandt, and I. Staude, *Resonant dielectric metasurfaces: active tuning and nonlinear effects*, J. Phys. D: Appl. Phys **52**, 373002 (2019).

[184] M. Cotrufo, D. de Ceglia, H. Jung, I. Brener, D. Neshev, C. De Angelis, and

A. Alù, *Nonlinear analog processing with anisotropic nonlinear films*, arXiv preprint arXiv:2409.16448 (2024).

[185] G. Zograf, K. Koshelev, A. Zalogina, V. Korolev, R. Hollinger, D.-Y. Choi, M. Zuerch, C. Spielmann, B. Luther-Davies, D. Kartashov, et al., *High-harmonic generation from resonant dielectric metasurfaces empowered by bound states in the continuum*, ACS Photonics **9**, 567 (2022).

[186] K. L. Koshelev, Z. F. Sadrieva, A. A. Shcherbakov, Y. S. Kivshar, and A. A. Bogdanov, *Bound states in the continuum in photonic structures*, Phys. Usp **93**, 528 (2023).

[187] K. I. Okhlopkov, A. Zilli, A. Tognazzi, D. Rocco, L. Fagiani, E. Mafakheri, M. Bollani, M. Finazzi, M. Celebrano, M. R. Shcherbakov, et al., *Tailoring third-harmonic diffraction efficiency by hybrid modes in high-Q metasurfaces*, Nano Lett. **21**, 10438 (2021).

[188] C. U. Hail, L. Michaeli, and H. A. Atwater, *Third harmonic generation enhancement and wavefront control using a local high-Q metasurface*, Nano Lett. **24**, 2257 (2024).

[189] L. Carletti, K. Koshelev, C. De Angelis, and Y. Kivshar, *Giant nonlinear response at the nanoscale driven by bound states in the continuum*, Phys. Rev. Lett. **121**, 033903 (2018).

[190] I. S. Sinev, K. Koshelev, Z. Liu, A. Rudenko, K. Ladutenko, A. Shcherbakov, Z. Sadrieva, M. Baranov, T. Itina, J. Liu, A. A. Bogdanov, and Y. Kivshar, *Observation of ultrafast self-action effects in quasi-BIC resonant metasurfaces*, Nano Lett. **21**, 8848 (2021).

[191] O. A. Abdelraouf, Z. Wang, H. Liu, Z. Dong, Q. Wang, M. Ye, X. R. Wang, Q. J. Wang, and H. Liu, *Recent advances in tunable metasurfaces: materials, design, and applications*, ACS Nano **16**, 13339 (2022).

[192] L. Carletti, M. Gandolfi, D. Rocco, A. Tognazzi, D. de Ceglia, M. A. Vincenti, and C. De Angelis, *Reconfigurable nonlinear response of dielectric and semiconductor metasurfaces*, Nanophotonics **10**, 4209 (2021).

[193] J. Deng, Y. Tang, S. Chen, K. Li, A. V. Zayats, and G. Li, *Giant enhancement of second-order nonlinearity of epsilon-near-zero medium by a plasmonic metasurface*, Nano Lett. **20**, 5421 (2020).

[194] W. Ye, F. Zeuner, X. Li, B. Reineke, S. He, C.-W. Qiu, J. Liu, Y. Wang, S. Zhang, and T. Zentgraf, *Spin and wavelength multiplexed nonlinear metasurface holography*, Nat. Commun. **7**, 11930 (2016).

[195] Z. Chai, X. Hu, F. Wang, X. Niu, J. Xie, and Q. Gong, *Ultrafast all-optical switching*, Adv. Opt. Mater. **5**, 1600665 (2017).

[196] S. M. Kamali, E. Arbabi, A. Arbabi, and A. Faraon, *A review of dielectric optical metasurfaces for wavefront control*, Nanophotonics **7**, 1041 (2018).

[197] M. Khorasaninejad, W. T. Chen, R. C. Devlin, J. Oh, A. Y. Zhu, and F. Capasso, *Metalenses at visible wavelengths: Diffraction-limited focusing and subwavelength resolution imaging*, Science **352**, 1190 (2016).

[198] D. N. Neshev, and A. E. Miroshnichenko, *Enabling smart vision with metasurfaces*, Nat. Photonics **17**, 26 (2023).

[199] J. P. B. Mueller, N. A. Rubin, R. C. Devlin, B. Groever, and F. Capasso,

Metasurface polarization optics: independent phase control of arbitrary orthogonal states of polarization, Phys. Rev. Lett. **118**, 113901 (2017).

[200] E. Arbabi, S. M. Kamali, A. Arbabi, and A. Faraon, *Full-Stokes imaging polarimetry using dielectric metasurfaces*, ACS Photonics **5**, 3132 (2018).

[201] A. Leitis, A. Tittl, M. Liu, B. H. Lee, M. B. Gu, Y. S. Kivshar, and H. Altug, *Angle-multiplexed all-dielectric metasurfaces for broadband molecular fingerprint retrieval*, Sci. Adv. **5**, eaaw2871 (2019).

[202] H. Kwon, D. Sounas, A. Cordaro, A. Polman, and A. Alù, *Nonlocal metasurfaces for optical signal processing*, Phys. Rev. Lett. **121**, 173004 (2018).

[203] H. Liu, C. Guo, G. Vampa, J. L. Zhang, T. Sarmiento, M. Xiao, P. H. Bucksbaum, J. Vučković, S. Fan, and D. A. Reis, *Enhanced high-harmonic generation from an all-dielectric metasurface*, Nat. Phys. **14**, 1006 (2018).

[204] C. McDonnell, J. Deng, S. Sideris, T. Ellenbogen, and G. Li, *Functional THz emitters based on Pancharatnam-Berry phase nonlinear metasurfaces*, Nat. Commun. **12**, 30 (2021).

[205] S. D. Roscam Abbing, R. Kolkowski, Z.-Y. Zhang, F. Campi, L. Lötgering, A. F. Koenderink, and P. M. Kraus, *Extreme-ultraviolet shaping and imaging by high-harmonic generation from nanostructured silica*, Phys. Rev. Lett. **128**, 223902 (2022).

[206] P. Gutruf, C. Zou, W. Withayachumnankul, M. Bhaskaran, S. Sriram, and C. Fumeaux, *Mechanically tunable dielectric resonator metasurfaces at visible frequencies*, ACS Nano **10**, 133 (2016).

[207] A. Komar, R. Paniagua-Domínguez, A. Miroshnichenko, Y. F. Yu, Y. S. Kivshar, A. I. Kuznetsov, and D. Neshev, *Dynamic beam switching by liquid crystal tunable dielectric metasurfaces*, ACS Photonics **5**, 1742 (2018).

[208] M. Rahmani, L. Xu, A. E. Miroshnichenko, A. Komar, R. Camacho-Morales, H. Chen, Y. Zárate, S. Kruk, G. Zhang, D. N. Neshev, and Y. S. Kivshar, *Reversible thermal tuning of all-dielectric metasurfaces*, Adv. Funct. Mater. **27**, 1700580 (2017).

[209] P. J. van Essen, Z. Nie, B. de Keijzer, and P. M. Kraus, *Toward complete all-optical intensity modulation of high-harmonic generation from solids*, ACS Photonics **11**, 1832 (2024).

[210] Q. Zhou, Q. Qiu, T. Wu, Y. Li, and Z. Huang, *Ultrafast all-optical switching modulation of terahertz polarization conversion metasurfaces based on silicon*, ACS Omega **8**, 48465 (2023).

[211] A. Di Francescantonio, A. Zilli, D. Rocco, L. Coudrat, F. Conti, P. Biagioni, L. Duò, A. Lemaître, C. De Angelis, G. Leo, M. Finazzi, and M. Celebrano, *All-optical free-space routing of upconverted light by metasurfaces via nonlinear interferometry*, Nat. Nanotechnol. pp. 1–8 (2023).

[212] H. Xie, L. Gui, Y. Liu, F. Lin, Z. Zhang, and K. Xu, *Giant two-photon absorption response from a silicon quasi-BIC metasurface*, Appl. Phys. Lett. **123**, 211704 (2023).

[213] S. W. Leonard, H. M. Van Driel, J. Schilling, and R. B. Wehrspohn, *Ultrafast band-edge tuning of a two-dimensional silicon photonic crystal via free-carrier injection*, Phys. Rev. B **66**, 161102(R) (2002).

[214] J. Meyer, A. Elezzabi, and M. Hughes, *Infrared absorption and momentum relaxation of free carriers in silicon generated by subpicosecond above band gap radiation*, IEEE J.

Quant. Electron. **31**, 729 (1995).

[215] H. M. van Driel, *Kinetics of high-density plasmas generated in Si by 1.06-and 0.53-μm picosecond laser pulses*, Phys. Rev. B **35**, 8166 (1987).

[216] K. Sokolowski-Tinten, and D. von der Linde, *Generation of dense electron-hole plasmas in silicon*, Phys. Rev. B **61**, 2643 (2000).

[217] S. K. Cushing, M. Zürch, P. M. Kraus, L. M. Carneiro, A. Lee, H.-T. Chang, C. J. Kaplan, and S. R. Leone, *Hot phonon and carrier relaxation in Si(100) determined by transient extreme ultraviolet spectroscopy*, Struct. Dyn. **5**, 054302 (2018).

[218] K. E. Myers, Q. Wang, and S. L. Dexheimer, *Ultrafast carrier dynamics in nanocrystalline silicon*, Phys. Rev. B **64**, 161309(R) (2001).

[219] C. Becker, S. Linden, G. von Freymann, M. Wegener, N. Tétreault, E. Vekris, V. Kitaev, and G. A. Ozin, *Two-color pump-probe experiments on silicon inverse opals*, Appl. Phys. Lett. **87**, 091111 (2005).

[220] G. Li, S. Zhang, and T. Zentgraf, *Nonlinear photonic metasurfaces*, Nat. Rev. Mater. **2**, 1 (2017).

[221] A. M. Yao, and M. J. Padgett, *Orbital angular momentum: origins, behavior and applications*, Adv. Opt. Photonics **3**, 161 (2011).

[222] K. Murzyn, L. Guery, Z. Nie, M. van der Geest, and P. M. Kraus, *Point-spread function reduction through high-harmonic generation deactivation. Conference on Lasers and Electro-Optics/Europe (CLEO/Europe 2023) and European Quantum Electronics Conference (EQEC 2023), p cf_2_3* (2023).

[223] Y. R. Shen, *Principles of Nonlinear Optics* (Wiley-Interscience, New York, NY, USA, 1984).

[224] A. Fedotova, M. Younesi, J. Sautter, A. Vaskin, F. J. Lochner, M. Steinert, R. Geiss, T. Pertsch, I. Staude, and F. Setzpfandt, *Second-harmonic generation in resonant nonlinear metasurfaces based on lithium niobate*, Nano Lett. **20**, 8608 (2020).

[225] L. Qu, L. Bai, C. Jin, Q. Liu, W. Wu, B. Gao, J. Li, W. Cai, M. Ren, and J. Xu, *Giant second harmonic generation from membrane metasurfaces*, Nano Lett. **22**, 9652 (2022).

[226] L. Xu, D. A. Smirnova, R. Camacho-Morales, R. A. Aoni, K. Z. Kamali, M. Cai, C. Ying, Z. Zheng, A. E. Miroshnichenko, D. N. Neshev, et al., *Enhanced four-wave mixing from multi-resonant silicon dimer-hole membrane metasurfaces*, New J. Phys. **24**, 035002 (2022).

[227] A. S. Shorokhov, E. V. Melik-Gaykazyan, D. A. Smirnova, B. Hopkins, K. E. Chong, D.-Y. Choi, M. R. Shcherbakov, A. E. Miroshnichenko, D. N. Neshev, A. A. Fedyanin, et al., *Multifold enhancement of third-harmonic generation in dielectric nanoparticles driven by magnetic Fano resonances*, Nano Lett. **16**, 4857 (2016).

[228] S. Won, S. Choi, T. Kim, B. Kim, S.-W. Kim, and Y.-J. Kim, *Dynamic ultraviolet harmonic beam pattern control by programmable spatial wavefront modulation of near-infrared fundamental beam*, Nanophotonics **12**, 3373 (2023).

[229] D. Zhao, Z. Lin, W. Zhu, H. J. Lezec, T. Xu, A. Agrawal, C. Zhang, and K. Huang, *Recent advances in ultraviolet nanophotonics: from plasmonics and metamaterials to metasurfaces*, Nanophotonics **10**, 2283 (2021).

[230] Y. Deng, X. Wang, Z. Gong, K. Dong, S. Lou, N. Pégard, K. B. Tom, F. Yang,

Z. You, L. Waller, et al., *All-silicon broadband ultraviolet metasurfaces*, Adv. Mater. **30**, 1802632 (2018).

[231] G. Li, L. Wu, K. F. Li, S. Chen, C. Schlickriede, Z. Xu, S. Huang, W. Li, Y. Liu, E. Y. Pun, et al., *Nonlinear metasurface for simultaneous control of spin and orbital angular momentum in second harmonic generation*, Nano Lett. **17**, 7974 (2017).

[232] H. Ahmed, H. Kim, Y. Zhang, Y. Intaravanne, J. Jang, J. Rho, S. Chen, and X. Chen, *Optical metasurfaces for generating and manipulating optical vortex beams*, Nanophotonics **11**, 941 (2022).

[233] Y. Xu, J. Sun, J. Frantz, M. I. Shalaev, W. Walasik, A. Pandey, J. D. Myers, R. Y. Bekele, A. Tsukernik, J. S. Sanghera, et al., *Reconfiguring structured light beams using nonlinear metasurfaces*, Opt. Express **26**, 30930 (2018).

[234] A. H. Dorrah, and F. Capasso, *Tunable structured light with flat optics*, Science **376**, eabi6860 (2022).

[235] T. Badloe, J. Lee, J. Seong, and J. Rho, *Tunable metasurfaces: the path to fully active nanophotonics*, Adv. Photon. Res. **2**, 2000205 (2021).

[236] M. Celebrano, D. Rocco, M. Gandolfi, A. Zilli, F. Rusconi, A. Tognazzi, A. Mazzanti, L. Ghirardini, E. A. Pogna, L. Carletti, et al., *Optical tuning of dielectric nanoantennas for thermo-optically reconfigurable nonlinear metasurfaces*, Opt. Lett. **46**, 2453 (2021).

[237] J. Yu, S. Park, I. Hwang, D. Kim, F. Demmerle, G. Boehm, M.-C. Amann, M. A. Belkin, and J. Lee, *Electrically tunable nonlinear polaritonic metasurface*, Nat. Photon. **16**, 72 (2022).

[238] J. Sautter, I. Staude, M. Decker, E. Rusak, D. N. Neshev, I. Brener, and Y. S. Kivshar, *Active tuning of all-dielectric metasurfaces*, ACS Nano **9**, 4308 (2015).

[239] C. Zhang, J. Jing, Y. Wu, Y. Fan, W. Yang, S. Wang, Q. Song, and S. Xiao, *Stretchable all-dielectric metasurfaces with polarization-insensitive and full-spectrum response*, ACS Nano **14**, 1418 (2019).

[240] H. van Driel, *Optical effective mass of high density carriers in silicon*, Appl. Phys. Lett. **44**, 617 (1984).

[241] A. Aigner, T. Possmayer, T. Weber, A. A. Antonov, L. de S. Menezes, S. A. Maier, and A. Tittl, *Optical control of resonances in temporally symmetry-broken metasurfaces* (2025), Nature pp. 1-7 (2025), DOI: 10.1038/s41586-025-09363-7.

[242] E. A. A. Pogna, M. Celebrano, A. Mazzanti, L. Ghirardini, L. Carletti, G. Marino, A. Schirato, D. Viola, P. Laporta, C. De Angelis, G. Leo, G. Cerullo, M. Finazzi, and G. Della Valle, *Ultrafast, all optically reconfigurable, nonlinear nanoantenna*, ACS Nano **15**, 11150 (2021).

[243] A. Mazzanti, E. A. A. Pogna, L. Ghirardini, M. Celebrano, A. Schirato, G. Marino, A. Lemaítre, M. Finazzi, C. De Angelis, G. Leo, G. Cerullo, and G. Della Valle, *All-optical modulation with dielectric nanoantennas: Multiresonant control and ultrafast spatial inhomogeneities*, Small Sci. **1**, 2000079 (2021).

[244] N. Tavakoli, R. Spalding, A. Lambertz, P. Koppejan, G. Gkantzounis, C. Wan, R. Rohrich, E. Kontoleta, A. F. Koenderink, R. Sapienza, et al., *Over 65% sunlight absorption in a 1 μm Si slab with hyperuniform texture*, ACS Photonics **9**, 1206 (2022).

List of Publications

Related to this thesis

1. **F. Bijloo**, A. J. den Boef, P.M. Kraus and A. F. Koenderink, *Structure-in-Void Quasi-Bound State in the Continuum Metasurface for Deeply Subwavelength Nanostructure Metrology*, ACS Nano **19**, 3208232092 (2025). (**Chapter 2**)
2. **F. Bijloo**, A. J. den Boef, P.M. Kraus and A. F. Koenderink, *The Influence of Driving Pulse Properties on Third-Harmonic Diffraction from Quasi-BIC Metasurfaces*, ACS Photonics, accepted for publication. (**Chapter 3**)
3. **F. Bijloo**, K. Murzyn, F. van Emmerik, A. J. den Boef, P.M. Kraus and A. F. Koenderink, *Near-Unity All-Optical Modulation of Third-Harmonic Generation with a Fano-Resonant Dielectric Metasurface*, Nano Lett. **24**, 12942–12942 (2024). (**Chapter 4**)
4. **F. Bijloo**, M. Ogienko, A. J. den Boef, P.M. Kraus and A. F. Koenderink, *All-Optical Nonlinear Real and Fourier Space Shaping with All-Dielectric Fano Resonant Metasurfaces*, submitted. (**Chapter 5**)

Other

5. J. Abad-Arredondo, Z. Geng, G. Keijsers, **F. Bijloo**, F. J. García-Vidal, A. I. Fernández-Domínguez, and S. R. K. Rodriguez, *Spontaneous Symmetry Breaking in Diffraction*, Phys. Rev. Lett. **133**, 133803 (2024).
6. L. Guery, **F. Bijloo** and P.M. Kraus, *Digital holography using harmonic generation from solids for reconstruction of subwavelength nanostructures*, submitted.

Patents

1. **F. Bijloo**, A. F. Koenderink, P. M. Kraus, A. J. den Boef, *Method for nonlinear optical measurement of parameter*, PCT Int. App. (WO), No. WO2024165217A1 (2024).

Author Contributions

Chapter 2 *F. Bijloo* designed and fabricated metasurface samples, performed measurements, simulations, analyzed and interpreted the data and writing of the manuscript. *A. Röell* provided finite-sized array simulations. *P. M. Kraus* contributed to discussions and commented on the manuscript. *A. J. den Boef* joined in discussions. *A. F. Koenderink* contributed to interpretation, writing, setting up the equations for the model and offered overall supervision.

Chapter 3 *F. Bijloo* designed and fabricated metasurface samples, performed measurements, simulations, did the data interpretation and analysis and writing of the manuscript. *P. M. Kraus* contributed to discussions and commented on the manuscript and *A. F. Koenderink* wrote the initial coupled oscillator model, contributed to interpretation, writing, and offered overall supervision.

Chapter 4 *F. Bijloo* designed and fabricated metasurface samples, performed linear and nonlinear characterization measurements and simulations, analyzed the data and wrote the manuscript. *F. van Emmerik* performed nonlinear transient measurements and provided illustrations of the setup. *K. Murzyn* supervised the transient measurements and commented on the manuscript. *A. J. den Boef* joined in discussions. *P. M. Kraus* offered supervision, commented on the manuscript and discussed and interpreted results. *A. F. Koenderink* contributed to writing the first draft, next to interpretation, discussions, and overall supervision.

Chapter 5 *F. Bijloo* designed and fabricated metasurface samples, performed measurements, simulations, data analysis, calculations and wrote the manuscript. *M. Ogienko* helped with spatial deactivation measurements, the experimental setup and commented on the manuscript. *P. M. Kraus* offered supervision, commented on the manuscript and discussion and interpretation of results. *A. F. Koenderink* contributed to interpretation, writing, and overall supervision.

The author acknowledges the use of text-based artificial intelligence tools, which were consulted during the writing of the thesis for suggesting editing improvements in grammar and vocabulary on the sentence level, and which were used in debugging Python algorithms during data analysis.

Acknowledgements

Gratitude reciprocates

My time at AMOLF has been a journey of learning. During these years, I picked up some insights into photonics, of which this book became a result. However, the most meaningful growth came as an introspective journey. I discovered that one of the most empowering realizations is understanding ones role, both professionally and personally. As a PhD student, I learned to see myself as playing that role, rather than being it. This subtle shift allowed me to separate my emotions, needs, and sense of self-worth from my 'output'. We humans thrive when we are allowed to play. Once you recognize your role, you can take all of it a little less seriously, and approach life with curiosity, creativity and gratitude. Work becomes play, and growth follows naturally.

After this piece of wisdom, I would like to express my deep gratitude to the people who guided me through this journey of learning. First and foremost, my promotor, **Femius**. When we met by coincidence on Terschelling, just a few days after discussing a potential PhD position, the stars aligned for me to apply. The four years that followed were fantastic. You continue to inspire me in many ways, and I deeply value both your scientific brilliance and your personal outlook on life. I have no doubt the group will remain resonant with you at the helm. To my co-promotor, **Peter**, you have been an incredible guide. Your curiosity, your balance between leadership and collegiality, and your engaged approach have been invaluable. You always treated problems as something we could solve together, and through that attitude you reminded me time and again that physics is mostly fun and fascinating, not difficult and frustrating.

The Resonant Nanophotonics group is quite a bunch. **Deba**, my office buddy, I will always cherish our philosophical morning conversations about history, capitalism, racism, and of course, physics. **Nelson**, my spiritual brother, we shared so much joy. Growing oyster mushrooms, yogurt or peanut butter lunches, ecstatic dancing, and even sharing the stage as rappers at NWO Physics. **Nick**, my metrology mate, we started at the same time and rode the AMOLF-ARCNL-ASML rollercoaster together. I deeply appreciate your directness, honesty, and the way you connect deep theory to practical experiments with ease. **Marko**, without you, the setup would have fallen apart, or there wouldn't have been experiments in the first place. **Masha**, I first supervised you as a Masters student, and later you joined the group as a PhD student. You are incredibly sharp and endlessly quick-witted, and it's so much fun to be around you. **August**, you smart fella. How you manage to know something about everything still baffles me. **Kim** and **Steven**, your personal warmth and professional contributions to the group have both been great additions in the last year. Thank you **Floor**, for letting me guide you through a Bachelor project that somehow ended up forming half of my thesis. Also, a heartfelt thanks to **Kevin** for your contributions to that project, and even more for your curious, relaxed and positive energy. And **Louis**, your practical, hands-on mentality and easygoing spirit made working together on your Master's project an absolute pleasure.

This project was part of the AMOLF-ARCNL-ASML collaboration. **Arie**, you were an incredible help in explaining what the key metrology questions truly are, and your naturally curious mind always led to the most insightful questions. The High-Harmonic Generation and EUV group helped me occasionally step back from focusing solely on photonic resonances and instead look at the broader picture of the materials, the physics, and the science itself. The collaborative atmosphere in your group is something special and well worth preserving. I especially loved our paper-writing retreats, which were both productive and so much fun. **Sylvianne**, **Stefan**, **Manos**, **Nataliia**, **Francesco**, **Pieter**, **Leo**, **Thorben**, **Tanya**, **Roy**, and **Zhonghui**, through you, I always felt that I could also call ARCNL my home.

During the first two years of my PhD, I spent a lot, a lot, of time in the cleanroom. This would not have been possible without **Bob**, **Igor**, **Dimitri**, and *Hans*. You truly are the backbone of so much of the work at AMOLF, and without your help, it would have taken me much longer to get anything running in the Nanolab.

The magic of AMOLF is rooted in our cross-pollination and coffee. **Eva**, thank you for our breaks, talks and our dances. **Robin**, We make a funny team. *Matthias* and *Andrea*, thank you for showing me another side of AMOLF during my Master's project. **Said**, thank you for introducing me to AMOLF all the way in the beginning. **Giel**, **Kevin**, **Zhou**, **Roos**, **Vashist**, **Nassim**, our interactions about photonics never failed. **Ewold**, thank you for always bringing a fresh perspective and steering my research in interesting new directions. **Jesse**, **Roel**, **Rene**, **Jente**, **Menno**, **Daniel**, **Timo**, **Xiaofei**, **Fons**, **Lavanya**, **Tuoyu**, and **Giorgos**, may the photonic force always be with you. **Vera**, **Marjan**, bringing the lightness in the canteen. **Max** who made the fantastic 3D images for the last two chapters. **Daan**, **Linde**, **Nika**, **Mees**, **Loriane**, **Yorick**, **Alex**, **Ethan**, **Willemijn**, **Magda**, **Saskia**, **Hollie**, **Lukas**, and too many others to name, thank you for all that makes AMOLF so great.

Daniëlle en **Richard**, jullie hebben altijd gezegd dat ik moet doen waar ik gelukkig van wordt, nooit te streng op mezelf zijn, en vooral mezelf zijn. Volgens mij is dat goed gelukt zo. **Jeany** en **Colin**, prachtig hoe we zo dicht bij elkaar zijn gekomen lieve zus, en fantastisch dat er iemand te wachten staat om door jullie op de wereld gebracht te worden. **Luisa**, você sempre sabe como me deixar tranquilo e como me animar. A gente forma um time supimpa. **Floris**, you are actually the one that got me to AMOLF in the first place. The B-lattice and enter the voyager might still be my scientific highlights. **Dean**, **Cor**, **Bas**, **Daan**, **Leon**, **Joram**, **Robin**, het leven is mooi met vrienden als jullie. **Hongsie**, **Dylan**, **Ivan**, **Irma**, **Maria**, **Paolo**, **Francesca**,

Antonio, **Bibi** keep dancing through life. **Nathan**, tamo junto.

Finally, I would like to end by repeating my motto: *Gratitude reciprocates*. Happiness is not about what you get, but about what you give. Decide to every day step into the world with a heart full of love to share. Direct your energy toward appreciating the beauty around you, and you will see that everything you seek has already been there.